Topological Superconductivity and Majorana Fermions

by

Henrik Schou Røising

Thesis submitted for the degree of
Master of Science

Department of Physics
Faculty of Mathematics and Natural Sciences
University of Oslo

May 2016

Abstract

This thesis is devoted to the topic of one- and two-dimensional models of topological superconductivity. We study the Kitaev chain subject to closed and open boundary conditions. In the closed chain, we derive the energy spectrum, the ground state, and the topological invariant viewed as a certain Berry phase. We study two-point correlation functions and find enlarged values close to the topological phase transitions. The open chain is studied with focus on describing the degenerate ground states for a simple parameter choice in the topological phase. Then, the open system Hamiltonian is diagonalized numerically, and we model the order parameter with a spatial dependency. Additional Majorana zero modes appear if the order parameter changes sign. We also consider the $p + ip$ model. The localization of a Majorana zero mode, bound to a vortex that is described by Ginzburg-Landau theory, is found numerically. We propose an argument that results in a non-Abelian exchange transformation for a system of several vortices. The $p + ip$ model is also studied on an annulus; we approximate the ground state as a combination of boundary states and calculate its energy. The results are compared to a numerical implementation, and the agreement is convincing as the boundary separation becomes large compared to other length scales.

Takk

Takk til studentene og de ansatte på teoriavdelingen for å ha skapt et hyggelig miljø med godt faglig klima. En ekstra takk til Olav Fredrik Syljuåsen for å ha gitt meg svært gode tips til veien videre.

Denne oppgaven ville ikke ha blitt fullført uten uvurderlig veiledning fra Jon Magne Leinaas og Mats Horsdal. Takk, Jon Magne Leinaas for å ha delt av din svært dype innsikt og intuisjon. Takk, Mats Horsdal for å velvillig bidra med din omfattende kunnskap om topologisk superledning og for å ha gitt meg veldig nyttige tips til fremgangsmåter.

Tusen takk, Marte Julie Sætra for solid vennskap og hjelp til tekniske utfordringer knyttet til LaTeX. Tusen takk til Anders Lauvland for gode faglige diskusjoner og, spesielt det siste året, for å ha blitt en veldig god venn. Takk også til Henrik Sverre Limseth for gode samtaler, *snedige* innspill og matematiske innsikter. Jeg vil takke Mari Røysheim og Eli Bæverfjord Rye for å ha vært nære venner i fem intense år på Blindern. Tilværelsen på Blindern ville ikke blitt den samme uten dere. Til slutt vil jeg takke Hanne Schou Røising, Leif Hugo Stubrud og Victoria Frederikke Schou Røising for å alltid vise interesse og stor omsorg.

Henrik Schou Røising, 15.05.16, Oslo.

Contents

Chapter 1

Introduction

Topological phases of matter has emerged as a rapidly growing field of research during the past decades. The discovery of the *Quantum Hall*, and later the *Fractional Quantum Hall effect*, in the 80s led to an intense focus on quantum phases of matter, both experimentally and theoretically. This type of matter is characterized, qualitatively speaking, by certain properties that are robust against local perturbations. New quantum numbers are introduced to characterize it, such as the ground state degeneracy or quantized geometrical phases of the ground state. Moreover, topological phases in superconducting systems may host *Majorana boundary states* with *non-Abelian* exchange statistics. The apperance of these states is related to the intrinsic properties of low-dimensional systems. In some systems of two dimensions, particles being neither bosons nor fermions, called *anyons*, are predicted to occur [1]. Non-Abelian anyons, for instance, are expected to emerge in some filling fractions of the Fractional Quantum Hall effect. They are considered particularly interesting since they have a long-term application in *topological quantum computation*. In contrast to quantum computation schemes based on spin states, topological qubits may be highly non-local, and the information they carry is intrinsically protected from decoherence.

Superconductivity is a well-studied phenomenon, built on firm experimental grounds. A successful microscopic theory, today known as BCS-theory, was developed already in the late 50s [2]. It is a mean field description where an attractive interaction between phonons and electrons leads to a condensate of *Cooper-pairs*. BCS-theory, along with the phenomenological Ginzburg-Landau theory, were able of explaining a broad range of phenomena in low-temperature superconductivity [3]. Later, a systematic refinement of the theory of superconductors and insulators has led to a classification where topological properties are taken into account. A complete classification table for topological superconductors and insulators is now available [4]. The classification can be used to predict the number of topological phases a given model realizes. This is summarized in the form of an integer known as the *topological invariant*. So, in what sense are topological superconductors suited for hosting non-Abelian anyons, and in what form are they predicted to emerge? A part of the answer lies in the electron spin pairing. Originally, Cooper-paired electrons were taken to be of opposite spins. However, if equal spin states are paired up and

only one spin projection is active (effectively meaning that the models are *spinless*), Majorana fermions are permitted to occur in the form of quasiparticles.

Majorana fermions in condensed matter systems are rather different than in high-energy physics. Instead of appearing as fundamental particles in this context, a Majorana operator is hermitian, $\gamma^\dagger = \gamma$, and an equally weighted superposition of fermionic creation and annihilation operators. They may be said to constitute half a fermionic degree of freedom. Consequently, pairing up two Majorana modes yields a fermionic operator that may fill or empty one qubit state. Majorana modes are expected to bind themselves to vortices in some two-dimensional superconducting fluids [5]. Furthermore, the unitary transformation that encodes an adiabatic exchange of two Majorana modes, γ_1 and γ_2, has been shown to have a non-Abelian nature, $U = e^{\frac{\pi}{4}\gamma_2\gamma_1}$ [6]. Majorana modes are also expected to be localized on the ends of superconducting nanowires with special spin-pairing or close to domain walls. In principle, it sounds simpler to manipulate modes in a one-dimensional system. However, exchange of particles in one dimension is intuitively impossible without collision. This problem has been proposed avoided by constructing networks of wires with T-shaped junctions and manipulation of the chemical potential [7]. Observation of Majorana modes in condensed matter systems in itself would be an experimental breakthrough. Although results from recent experiments, such as [8, 9], are subject to some scepticism, there are reasons to believe that the definite confirmation of Majorana fermions is tantalizing close.

1.1 Outline

In this thesis two toy models, of one and two spatial dimensions respectively, belonging to the same category class will be studied. We will explore a discrete, one-dimensional chain first proposed by Alexei Kitaev in 2001 [10]. A two-dimensional analogue, the $p + ip$ model, will also be studied. These toy models models capture the essential physics needed to understand the core of topological superconductivity. The goal of this work is to obtain a comprehensive understanding of the main content of the models. Specifically, we will fill in omitted details in the brief presentation by Jason Alicea in [11]. In this process, several more specialized questions that were not formulated *a priori* arise. Some of the concrete issues that will be faced and an outline of the content in this thesis is given below.

In Chapter 2 we summarize the key concepts needed to put the effective models appearing later in a wider context. This is done with emphasis on keeping the description brief but concise. Central parts of BCS-theory and Ginzburg-Landau theory are recapitulated. An introduction to topological superconductors, Majorana fermions and anyons is given.

Chapter 3 is devoted to the Kitaev chain with *closed* boundary conditions. The Hamiltonian is diagonalized and the ground state derived. Some effort is spent on building intuition about the properties of both this state and excitations of it.

Thereafter, we study how a certain Berry phase calculation separates the parameters in a trivial and a topological phase. This motivates the last part of the chapter where two-point correlation functions in the ground state are calculated. The basic question we ask is *if*, and potentially *how*, the transition between the quantum phases manifest itself in these correlation functions. In particular, do the correlation functions show signs of long range effects? Finally, we discuss the differences between periodic and anti-periodic boundary conditions.

The Kitaev chain with *open* boundaries is studied in Chapter 4. We demonstrate the possibility of Majorana zero modes localized on each end in the spirit of Kitaev's original argument [10]. We depart from Kitaev's discussion by establishing what the degenerate ground state subspace looks like for a simple choice of parameters. In this process, it turns out that it is a non-trivial task to pick the correct ground states from a set of three candidate states. Then, we study the open Kitaev chain by numerical diagonalization, partly to obtain a visualization the energy spectrum in the presence of zero modes. We study next a spatially varying order parameter. It is of interest to explore if a kinked order parameter can give rise to additional Majorana modes. This extends the study of domain walls in chemical potential, which seems to be frequently discussed in the literature [7, 11, 12].

In Chapter 5 we study the two-dimensional $p + ip$ model. First, a formal development with a derivation of the diagonalization equations is presented. This is applied when we solve the equations numerically for a non-homogeneous order parameter in search of a Majorana zero mode solution. The order parameter is taken to describe a symmetric vortex in accordance with a minimal Ginzburg-Landau description. This extends known solutions with an infinitesimally small vortex core [13], and it naturally calls for a numerical implementation. Finally, we suggest an argument that results in an exchange transformation in a system of many Majorana vortices. Our argument is seen to agree with Ivanov's result [6], which in turn implies non-Abelian statistics (we demonstrate this in section 2.7).

Chapter 6 is concerned with the $p + ip$ model on an annulus geometry. Specifically, we are interested in calculating the energy splitting between Majorana modes localized on each of the circular boundaries. We approach the problem by finding analytical approximations to zero modes of systems having only an inner and an outer boundary respectively. A linear combination of these states is used as a trial state describing the ground state of the two-edged system. An analytical computation, resulting in the energy splitting as function of the boundary separation, is suggested. The result is tested by comparing the energy and the edge states with solutions found by numerical diagonalization.

The content of the thesis is summarized in Chapter 7. Here, the work is supplemented with concluding remarks and a brief presentation of the experimental status of topological superconductivity with realizations of Majorana fermions.

1.2 Notation

The notation in this thesis is meant to be self-explained for a reader with background in physics that has basic knowledge of quantum mechanics. Still, some conventions are settled at this stage to avoid possible confusion. Occasionally, the Pauli matrices will appear. They are

$$\sigma_x = \begin{pmatrix} 0 & 1 \\ 1 & 0 \end{pmatrix}, \quad \sigma_y = \begin{pmatrix} 0 & -i \\ i & 0 \end{pmatrix} \quad \text{and} \quad \sigma_z = \begin{pmatrix} 1 & 0 \\ 0 & -1 \end{pmatrix}. \tag{1.1}$$

In Chapter 3 we use the symbols (φ, ϑ) to denote the polar angles in three dimensions. In Chapter 5 and 6 the polar angle in two dimensions is denoted by θ. In discrete formulations, $\delta_{x,x'}$ is the Kronecker delta symbol being 1 if $x = x'$ and 0 otherwise. Whereas in continuum formulations we use the symbol $\delta^{(2)}(\boldsymbol{r} - \boldsymbol{r}')$ to denote the two-dimensional Dirac delta function. The symbol $\Theta(\rho)$ is used to denote the Heaviside function, which is 1 if $\rho > 0$ and 0 if $\rho < 0$. Expressions with repeated indices, such as $f_i = \epsilon_{ijk} g_{jk}$, are understood to imply summation over j and k according to the usual summing convention, $f_i \equiv \sum_{j,k} \epsilon_{ijk} g_{jk}$. The symbol ϵ_{ijk} denotes the three-dimensional Levi-Civita symbol being $+1$ if (i, j, k) is an even permutation of $(1, 2, 3)$ and -1 if (i, j, k) is an odd permutation of $(1, 2, 3)$. It is 0 for all other combinations of indices. Depending on the convenience and the respective context, indices will mostly be separated by a comma. Unless being very clear from the context, new notation that appear will be explained.

Chapter 2

Background Material

2.1 Superconductivity – an Overview

Although this thesis is devoted to modern theoretical models from around the beginning of the 21st century, it is appropriate to put them in a wider historical context. The purpose of this chapter is to revisit and recapitulate some of the ideas that were developed over a long time span. This will provide the reader with an overview, and it will motivate the effective models appearing in the main chapters (3 - 6). The material in this section is based on [3].

The concept of superconductivity is more than a hundred years old but still highly active in terms of research. In 1911 H. K. Onnes discovered that certain materials exhibited zero electrical resistance below a (material dependent) critical temperature T_c. The discovery of *perfect conductivity* was accompanied in 1933 by W. Meissner and R. Ochsenfeld findings of *perfect diamagnetism*. They found that external magnetic field lines were expelled entirely and abruptly from some material samples when the field strength was less than a critical value, $H < H_c(T)$. Superconductors with this property are today referred to as being of type I. Shortly after this, F. and H. London proposed two electrodynamic equations that, among other predictions, suggested an exponential decay of the magnetic field into the sample. This was the start of a microscopic approach to explaining superconductivity. A characteristic length scale of the magnetic decay, λ, is called the *penetration depth* and is one of two important length scales in the theory of superconductivity.

In 1950 a phenomenological theory by V. Ginzburg and L. Landau appeared. Apart from successfully predicting several known phenomena, Landau-theory is today known as a more general mean field approach to deriving macroscopic properties. We will revisit this theory in more detail later, but simply mention here that another important length scale appears in this theory. The *Ginzburg-Landau coherence length*, a, characterizes a spatial length over which the superconducting electron density, n_s, does not change significantly. Furthermore, the ratio between the two length scales, $\kappa = \lambda/a$, turned out to reveal an important distinction, as first noticed by

A. A. Abrikosov in 1957 [14]. He showed that $\kappa = 1/\sqrt{2}$ separated two types of superconductivity. The previously known breakdown in flux penetration at H_c was now seen to occur when $\kappa < 1/\sqrt{2}$. Materials with $\kappa > 1/\sqrt{2}$, however, was found to have a continuous increase in magnetic flux penetration. This is known as type II superconductivity. Materials with this property are characterized by *two* critical field strengths, $H_{c_1}(T)$ and $H_{c_2}(T)$. Imagining that the external field H is increased from zero, the magnetic breakdown of a type II material starts at $H_{c_1}(T)$ and increases continuously to $H_{c_2}(T)$, where the breakdown is complete.

Abrikosov crucially discovered that for type II superconductors in the mixed state, $H_{c_1} < H < H_{c_2}$, the magnetic flux penetrates the material sample in a *regular grid of flux tubes*. Each tube carries one (superconducting) quantum flux unit,

$$\Phi_0 = \frac{hc}{2e} \approx 2.068 \cdot 10^{-15} \text{ Wb}. \tag{2.1}$$

He named this intermediate phase the *vortex lattice phase* and performed a numerical calculation showing that a square grid of flux tubes should be energetically favoured. It later turned out that a triangular grid has a slightly higher preference in most materials. These vortex grids were confirmed experimentally in 1967. Later, they have been depicted beautifully by use of tunnelling spectroscopy. During 1957, a complete and successful microscopic theory was proposed by J. Bardeen, L. Cooper and J. R. Schrieffer [2]. Their theory is today referred to as *BCS-theory*.[1]

2.2 BCS-Theory

In BCS-theory weakly attracting pairs of electrons form a condensate and make up the fundamental building blocks of superconductivity. These bound states were investigated and presented by Cooper in 1956. The reason for the attraction will be explained here superficially. Then, we will see how effective models arise using mean field theory. Moreover, we recapitulate the BCS ground state and an important self-consistent equation. This section is based on [3], but it contain elements from other sources as indicated.

2.2.1 Electron-Phonon Interaction

Cooper showed that pairs of electrons will form in the Fermi sea as long as there exist an arbitrarily weak attractive potential. Such a potential could originate from a *phonon-electron interaction*. Briefly explained, the electrons polarizes the medium they travel through by Coulomb attraction of positive grid ions. This forms a small perturbation in the ion grid that can attract a second electron. Effectively, it can be seen as the two electrons interacting attractively by a phonon mediator,

[1] In 1972 Bardeen, Cooper and Schrieffer were awarded the Nobel Prize for their contribution. Abrikosov and Ginzburg were awarded the Nobel Prize (as late as) in 2003.

analogous to QED and the electron-photon interaction. An effective Hamiltonian of the system takes the following form in second quantized language (without the Coulomb interaction) [15]:

$$\begin{aligned} H &= H_{\text{electron}} + H_{\text{phonon}} + \lambda V_{\text{F}} \\ &= \sum_{\boldsymbol{k},s} \epsilon_k c^\dagger_{\boldsymbol{k},s} c_{\boldsymbol{k},s} + \sum_{\boldsymbol{q},\sigma} \hbar\omega_q \left(a^\dagger_{\boldsymbol{q},\sigma} a_{\boldsymbol{q},\sigma} + \frac{1}{2} \right) + \lambda \sum_{\boldsymbol{k},s,\boldsymbol{q}} (V_q a_{\boldsymbol{q},\parallel} c^\dagger_{\boldsymbol{k}+\boldsymbol{q},s} c_{\boldsymbol{k},s} + \text{h.c.}). \end{aligned} \tag{2.2}$$

The free electron gas is described by H_{electron}, with sums running over all momenta $\boldsymbol{k}$ and spin projections $s \in \{\uparrow, \downarrow\}$. The kinetic energy is in the non-relativistic limit given by $\epsilon_k = \hbar^2 k^2/(2m_e)$. Moreover, the fermion operators obey the canonical anticommutation relations

$$\{c^\dagger_{\boldsymbol{k},s}, c_{\boldsymbol{k}',s'}\} = \delta_{\boldsymbol{k},\boldsymbol{k}'}\delta_{s,s'} \quad \text{and} \quad \{c_{\boldsymbol{k},s}, c_{\boldsymbol{k}',s'}\} = \{c^\dagger_{\boldsymbol{k},s}, c^\dagger_{\boldsymbol{k}',s'}\} = 0. \tag{2.3}$$

The term H_{phonon} describes the quantized phonon vibrations with $\boldsymbol{q}$ as the phonon mode, σ the phonon polarization[2] and $\omega_q = vq$ the phonon frequency. The phonon spectrum has the usual Debye cutoff at $\omega_D = v(6\pi^2\rho)^{1/3}$ in a three dimensional solid with ion density ρ [16]. As the phonons are bosons, they obey the commutation relations

$$[a_{\boldsymbol{q},\sigma}, a^\dagger_{\boldsymbol{q}',\sigma'}] = \delta_{\boldsymbol{q},\boldsymbol{q}'}\delta_{\sigma,\sigma'} \quad \text{and} \quad [a_{\boldsymbol{q},\sigma}, a_{\boldsymbol{q}',\sigma'}] = [a^\dagger_{\boldsymbol{q},\sigma}, a^\dagger_{\boldsymbol{q}',\sigma'}] = 0. \tag{2.4}$$

Finally, the interaction term, λV_F, is known as the *Fröhlich interaction Hamiltonian*. The parameter λ is a (small) coupling constant and V_q the scattering amplitude. The interaction term describes a fermion with momentum $\boldsymbol{k}$ absorbing a phonon of momentum $\boldsymbol{q}$. When treating the Hamiltonian (2.2) perturbatively in λ, one can obtain rules and draw interaction diagrams, like Feynman rules in QED. Deriving this thoroughly is outside the scope of this presentation. Instead, we simply state the result that V_F gives rise to a scattering amplitude of the form [15]

$$\langle \boldsymbol{k}_3, \boldsymbol{k}_4 | \, V_F \, | \boldsymbol{k}_1, \boldsymbol{k}_2 \rangle = |V_q|^2 \frac{\hbar\omega_q}{\left(\epsilon_{|\boldsymbol{k}_1+\boldsymbol{q}|} - \epsilon_{k_1}\right)^2 - \hbar^2\omega_q^2} \delta_{\boldsymbol{k}_1+\boldsymbol{k}_2,\boldsymbol{k}_3+\boldsymbol{k}_4} \delta_{\boldsymbol{k}_1-\boldsymbol{k}_3,\boldsymbol{q}} \delta_{s_1,s_3} \delta_{s_2,s_4}, \tag{2.5}$$

to the order $\mathcal{O}(\lambda^2)$ for scattering of initial fermion states 1 and 2 onto 3 and 4. The important thing to notice about this expression is that it reflects an *attractive* interaction whenever $|\epsilon_{|\boldsymbol{k}_1+\boldsymbol{q}|} - \epsilon_{k_1}| < \hbar\omega_q$. In comparison, an electron-electron scattering would be strictly positive and inversely proportional to q^2, when neglecting the electron screening effect. Dominance of the attractive potential over the repulsive Coulomb interaction was originally proposed as the criterion for superconductivity [2].

[2]There are three possible polarization directions in three dimension. However, the normal modes do not generate charge density variations and should be excluded.

2.2.2 The Mean Field Hamiltonian

We look at a phenomenological Hamiltonian taking the electron-phonon interaction into account. Consider

$$H = \sum_{\boldsymbol{k},s} \epsilon_k c^\dagger_{\boldsymbol{k},s} c_{\boldsymbol{k},s} + \sum_{\boldsymbol{k},\boldsymbol{l}} V_{\boldsymbol{k},\boldsymbol{l}} c^\dagger_{\boldsymbol{k},\uparrow} c^\dagger_{-\boldsymbol{k},\downarrow} c_{-\boldsymbol{l},\downarrow} c_{\boldsymbol{l},\uparrow}, \tag{2.6}$$

with $V_{\boldsymbol{k},\boldsymbol{l}}$ a Fourier transformed scattering potential including both the (screened) Coulomb interaction and the electron-phonon interaction in (2.5). The Hamiltonian pairs up states of opposite momenta and spin. In the *mean field treatment* we introduce fluctuations around the averages,

$$\delta(cc) \equiv c_{-\boldsymbol{l},\downarrow} c_{\boldsymbol{l},\uparrow} - \langle c_{-\boldsymbol{l},\downarrow} c_{\boldsymbol{l},\uparrow} \rangle \quad \text{and} \quad \delta(c^\dagger c^\dagger) \equiv c^\dagger_{\boldsymbol{k},\uparrow} c^\dagger_{-\boldsymbol{k},\downarrow} - \langle c^\dagger_{\boldsymbol{k},\uparrow} c^\dagger_{-\boldsymbol{k},\downarrow} \rangle, \tag{2.7}$$

and assume that terms of order $\mathcal{O}(\delta^2)$ are vanishingly small. Inserting this into equation (2.6) while introducing the *order parameter*,

$$\Delta(\boldsymbol{k}) \equiv \sum_{\boldsymbol{l}} V_{\boldsymbol{k},\boldsymbol{l}} \langle c_{-\boldsymbol{l},\downarrow} c_{\boldsymbol{l},\uparrow} \rangle, \tag{2.8}$$

yields the mean field result

$$H_{\mathrm{MF}} = \sum_{\boldsymbol{k},s} \epsilon_k c^\dagger_{\boldsymbol{k},s} c_{\boldsymbol{k},s} + \sum_{\boldsymbol{k}} \left(\Delta(\boldsymbol{k}) c^\dagger_{\boldsymbol{k},\uparrow} c^\dagger_{-\boldsymbol{k},\downarrow} + \Delta^*(\boldsymbol{k}) c_{-\boldsymbol{k},\downarrow} c_{\boldsymbol{k},\uparrow} \right) - \sum_{\boldsymbol{k}} \Delta(\boldsymbol{k}) \langle c^\dagger_{\boldsymbol{k},\uparrow} c^\dagger_{-\boldsymbol{k},\downarrow} \rangle. \tag{2.9}$$

The last term is constant and of little interest. We see by construction that $\Delta(\boldsymbol{k})$ is a parameter that implies correlations of the type $\langle c_{-\boldsymbol{l},\downarrow} c_{\boldsymbol{l},\uparrow} \rangle$. Such correlations would be absent in a normal metal; the order parameter reflects Cooper pairing.

Above, Cooper pairs were formed with opposite spin. This was how it was originally treated in BCS-theory. However, it has later been generalized to other spin configurations. We briefly pursue a more modern treatment and separate out spin indices m and n in the order parameter,

$$H_{\mathrm{MF}} = \sum_{\boldsymbol{k},s} \epsilon_k c^\dagger_{\boldsymbol{k},s} c_{\boldsymbol{k},s} + \sum_{\boldsymbol{k}} \left(\Delta_{m,n}(\boldsymbol{k}) c^\dagger_{\boldsymbol{k}} c^\dagger_{-\boldsymbol{k}} + \mathrm{h.c.} \right). \tag{2.10}$$

Here, the order parameter is conventionally allowed to have both a spin-singlet component, which we denote by $\Delta_s(\boldsymbol{k})$, and components in any of the three spin-triplet configurations, denoted by $\boldsymbol{d}(\boldsymbol{k})$. For completeness, recall the spin-singlet state, $(|\uparrow\downarrow\rangle - |\downarrow\uparrow\rangle)/\sqrt{2}$, and the spin-triplet states, $\{|\uparrow\uparrow\rangle, |\downarrow\downarrow\rangle, (|\uparrow\downarrow\rangle + |\downarrow\uparrow\rangle)/\sqrt{2}\}$. We follow the convention in [4] and express the generalized order parameter as

$$\begin{aligned}\Delta_{m,n}(\boldsymbol{k}) &= \Big[\left(\Delta_s(\boldsymbol{k})\mathbb{1} + \boldsymbol{d}(\boldsymbol{k})\cdot\boldsymbol{\sigma}\right) i\sigma_y \Big]_{m,n} \\ &= \begin{pmatrix} -d_x + id_y & d_z + \Delta_s \\ d_z - \Delta_s & d_x + id_y \end{pmatrix}_{m,n}.\end{aligned} \tag{2.11}$$

Above, we made use of the Pauli matrices and the vector containing them, $\boldsymbol{\sigma} = \begin{pmatrix}\sigma_x, & \sigma_y, & \sigma_z\end{pmatrix}^T$. The spin-singlet function is *symmetric* under spatial inversion, $\Delta_s(-\boldsymbol{k}) = \Delta_s(\boldsymbol{k})$, while the spin-triplet function is *antisymmetric*, $\boldsymbol{d}(-\boldsymbol{k}) = -\boldsymbol{d}(\boldsymbol{k})$, making the generalized order parameter satisfy the Pauli exclusion principle,[3]

$$\Delta_{m,n}(\boldsymbol{k}) = -\Delta_{n,m}(-\boldsymbol{k}). \tag{2.12}$$

Conventional superconductors have spin singlet pairing ($\boldsymbol{d} = \boldsymbol{0}$) and Cooper pairs of even angular momentum. The pairing is typically denoted after increasing angular momentum, such as s-wave, d-wave, etc. Note that this nomenclature is similar to that of atomic states in the periodic table [17]. Superconductors with spin triplet pairing ($\Delta_s = 0$) have Cooper pairs with odd angular momenta. The lowest angular momentum configuration of this type is called p-wave, and it is experimentally exotic. For instance, letting $d_x = d_y = 0$ and $d_z = k_x \pm ik_y$ would give a spinfull, chiral $p \pm ip$ superconductor. A continuum and *spinless* version of this model is studied in Chapter 5 and 6.

2.2.3 The Ground State and the Gap Equation

The Hamiltonian (2.10) can be diagonalized with a *Bogoliubov transformation*. This approach is applied in some detail in Chapter 3. Instead of focusing on this method here, we review how BCS originally searched for the ground state. We return to the Hamiltonain in equation (2.6). A general ansatz for a N-particle ground state with Cooper pairing could be [2]

$$|\psi_G\rangle = \sum_{\{\boldsymbol{k}_i\}} g(\boldsymbol{k}_1, \ldots, \boldsymbol{k}_{N/2}) c^\dagger_{\boldsymbol{k}_1,\uparrow} c^\dagger_{-\boldsymbol{k}_1,\downarrow} \cdots c^\dagger_{\boldsymbol{k}_{N/2},\uparrow} c^\dagger_{-\boldsymbol{k}_{N/2},\downarrow} |0\rangle\,, \tag{2.13}$$

with the sums running over all momenta $\boldsymbol{k}_i$ and $|0\rangle$ denoting the vacuum state, which is destroyed by any $c_{\boldsymbol{k},s}$ operator. It is clearly a difficult combinatoric task to determine the weighting coefficients g. However, BCS treated N statistically, which basically corresponds to applying the *grand canonical ensemble* [16]. A simplified ansatz (using multiplicative separation) for the ground state was taken to be

$$|\psi_G\rangle = \prod_{\boldsymbol{k}} (u_{\boldsymbol{k}} + v_{\boldsymbol{k}} c^\dagger_{\boldsymbol{k},\uparrow} c^\dagger_{-\boldsymbol{k},\downarrow}) |0\rangle\,, \tag{2.14}$$

[3]The order parameter $\Delta_{m,n}(\boldsymbol{k})$ should obey the Pauli principle because it involves a correlation between two fermionic operators.

with $|u_{\boldsymbol{k}}|^2+|v_{\boldsymbol{k}}|^2 = 1$. Determining the weights $u_{\boldsymbol{k}}$ and $v_{\boldsymbol{k}}$ was set up as a variational problem,

$$\delta \langle\psi_G| H - \mu \sum_{\boldsymbol{k},s} c^\dagger_{\boldsymbol{k},s} c_{\boldsymbol{k},s} |\psi_G\rangle = 0. \tag{2.15}$$

Including the term $-\mu\langle N\rangle$ moves the zero point in kinetic energy to the Fermi surface, $\sum_k \epsilon_k = \mu\langle N\rangle$. One may now parametrize the coefficients by an angle, $u_{\boldsymbol{k}} = \cos\theta_{\boldsymbol{k}}$ and $v_{\boldsymbol{k}} = \sin\theta_{\boldsymbol{k}}$, to take care of the normalization, and then minimize with respect to $\theta_{\boldsymbol{k}}$. Going through these steps in detail becomes lengthy, so we restrict ourselves to stating the result. The final self-consistent equation is known as the *gap equation* (here for $T = 0$),

$$\Delta_{\boldsymbol{k}} = -\frac{1}{2}\sum_{\boldsymbol{l}} \frac{\Delta_{\boldsymbol{l}}}{\sqrt{(\epsilon_k - \mu)^2 + \Delta^2_{\boldsymbol{l}}}} V_{\boldsymbol{k},\boldsymbol{l}}. \tag{2.16}$$

This determines the order parameter rigorously in principle, although it often has to be treated numerically in practice. Analytical approximations of the order parameter can be obtained by applying certain simplifications. For instance by assuming that $V_{\boldsymbol{k},\boldsymbol{l}} = -V$ is constant. The most important application of the gap equation is, however, to approximate the critical temperature (at finite temperatures the equation is slightly modified). We will not pursue such approximations here, but rather emphasise the existence and importance of this equation in conventional BCS-theory. The gap equation will not be used in this thesis. Instead, we will apply the phenomenological Ginzburg-Landau theory to approximate the order parameter of a vortex.

2.3 Ginzburg-Landau Theory

In this section we establish some basic concepts related to Ginzburg-Landau theory and vortices. It will be put to use in Chapter 5. Still, the presented material is based on [3], unless otherwise specified.

In 1950, seven years before the microscopic theory of superconductivity was at hand, V. Ginzburg and L. Landau proposed a macroscopic theory was able of predicting several aspects of a second order phase transition. Their theory also proved to be successful on systems with a non-homogeneous order parameter. The basic idea is to assume that the free energy can be expanded in powers of an order parameter ϕ, in vicinity of the critical temperature T_c. This parameter, ϕ, is assumed to be zero in the normal phase, $T > T_c$. Close to the critical temperature the parameter should be small, and the free energy can be expanded as a power sum,

$$F = F_n + \lambda\phi + \alpha\phi^2 + \gamma\phi^3 + \frac{\beta}{2}\phi^4, \tag{2.17}$$

with F_n being the free energy in the normal phase, and the parameters λ, α, γ and β being functions of $(T - T_c)$. Requiring that $\phi = 0$ should be a minimum of F in the normal phase implies that $\lambda = 0$. Ginzburg and Landau associated the order parameter with a *pseudo wavefunction*, $\phi = \psi(\boldsymbol{r})$, describing the superconducting electron density $n_s = |\psi(\boldsymbol{r})|^2$. This underpins that we now discard the term with ϕ^3 (F must be real and ψ is generally complex). A vector potential and a phenomenological kinetic term is included, and we express the free energy density as

$$f(\boldsymbol{r}) = f_n + \alpha|\psi(\boldsymbol{r})|^2 + \frac{\beta}{2}|\psi(\boldsymbol{r})|^4 + \frac{1}{2m^*}\left|\left(-i\hbar\nabla - \frac{e^*}{c}\boldsymbol{A}\right)\psi(\boldsymbol{r})\right|^2, \tag{2.18}$$

with m^* and e^* the effective mass and charge respectively. Intuitively, although not settled at the time of formulation, $m^* = 2m_e$ and $e^* = -2e$ are the mass and charge of a condensate Cooper pair. In 1959 L. Gor'kov established a relation between the pseudo wavefunction $\psi(\boldsymbol{r})$ and the order parameter in BCS-theory, $\Delta(\boldsymbol{r})$ [18]. Near the critical temperature, the two quantities were shown to be directly proportional, and Ginzburg-Landau theory was seen as a limiting case of BCS-theory.[4]

2.3.1 Vortices

A quantum vortex is characterized by a non-homogeneous region in the superconducting fluid, accompanied by the presence of angular momentum. In the vortex core the superconducting electron density, n_s, and consequentially the order parameter, drops to zero. For a rotationally symmetric vortex $|\psi(\boldsymbol{r})|^2$ depends on r only. Thus, the basic ansatz of such a vortex reads

$$\psi(\boldsymbol{r}) = h(r)e^{iS(\boldsymbol{r})}, \tag{2.19}$$

with $h(r)$ some real function. If $\psi(\boldsymbol{r})$ is assumed to be an eigenfunction of the angular momentum operator, $L_z = i\hbar\partial/\partial\theta$, then $S(\boldsymbol{r}) = n\theta$ for some arbitrary n and θ being the polar angle. Moreover, requiring $\psi(r, \theta)$ to be *single valued*, $\psi(r, \theta + 2\pi) = \psi(r, \theta)$, implies the restriction $n \in \mathbb{Z}$. This integer is called the *vorticity*.

Next, we consider constraints on the expansion in equation (2.18) due to superconducting effects. For simplicity, we neglect the kinetic part of the free energy in this consideration. If the power expansion is enforced to have a finite minimum, we must assume that $\beta > 0$. This means that if $\alpha > 0$, then f has only the trivial minimum at $|\psi|^2 = 0$. This is the *normal phase*. On the other hand, $\alpha < 0$ is called the *superconducting phase* with minimum occurring at

$$|\psi_\infty|^2 = -\frac{\alpha}{\beta}, \tag{2.20}$$

[4]To be precise, Gor'kov derived the relation $\psi(\boldsymbol{r}) = \Delta(\boldsymbol{r})\sqrt{7\zeta(3)n}/(4\pi T_c)$, with ζ being the Riemann zeta function, n the number density of electrons in the normal metal, and T_c the critical temperature [18].

and the subscript indicating that this is the equilibrium value far from vortices. A phase transition would formally occur if we let $\alpha \propto (T - T_c)$ and β be constant. It implies the normal phase for $T > T_c$. From now on, we consider a field free system, $\boldsymbol{A} = \mathbf{0}$, but with the kinetic term in (2.18) present. The dynamical equations may then be determined as the variational problem $\delta F/\delta\psi^* = 0$,

$$\begin{aligned} \frac{\delta}{\delta\psi^*} \int \mathrm{d}V \; f(\psi, \psi^*, \nabla\psi, \nabla\psi^*) = 0, \\ \frac{\hbar^2}{2m^*}\nabla^2\psi - \alpha\psi - \beta|\psi|^2\psi = 0. \end{aligned} \tag{2.21}$$

This is a non-linear, homogeneous differential equation. It is usually referred to as one of the *Ginzburg-Landau equations* (here: without the vector potential). Finally, we consider it on dimensionless form. Assume that $T < T_c$ and redefine $\alpha \to -\alpha > 0$ such that both expansion coefficients are positive. We scale the wavefunction with its equilibrium value, $\psi_\infty = \sqrt{\alpha/\beta}$, and introduce a length scale,

$$\hat{\psi} \equiv \frac{\psi}{\psi_\infty} \quad \text{and} \quad \boldsymbol{\rho} \equiv \frac{\boldsymbol{r}}{a} \quad \text{with} \quad a \equiv \frac{\hbar}{\sqrt{2m^*\alpha}} \propto (T_c - T)^{-1/2}. \tag{2.22}$$

Altogether, this brings the equation to the form

$$\nabla^2\hat{\psi} + (1 - |\hat{\psi}|^2)\hat{\psi} = 0, \tag{2.23}$$

where the derivatives are with respect to components of $\boldsymbol{\rho}$. The length scale a is called the *Ginzburg-Landau coherence length*. It determines the length scale over which the order parameter reaches its equilibrium value if perturbed in some region. Solving (2.23) with boundary conditions $|\hat{\psi}(\rho = 0)| = 0$, $|\hat{\psi}(\rho = \infty)| = 1$, with the ansatz in (2.19), would correspond to the presence of a vortex at $\rho = 0$.

2.4 Symmetries and Classification of Topological Superconductors

Recently, models for topological superconductors and insulators have been subject to a comprehensive classification in terms of present or absent symmetries. A complete "periodic table" of the *ten symmetry classes* that exist for non-interacting systems of fermions is now available [4]. The central result of the classification is information of the number of topological phase transitions a given model supports, which is summarized in the *topological invariant*. Typically, topological superconductivity can not be controlled in terms of a single, easily controllable parameter tuned to make exotic properties appear. A topological phase transition does usually manifest itself in some discrete change in the ground state that is not obtainable by any continuous transformation. Invariance of quantities when the Hamiltonian is subject to adiabatic deformations is loosely speaking what is meant by the word

"topological".

The three discrete symmetries that uniquely places a model in the classification system will be described briefly. They are: the *time-reversal symmetry* (TRS) $\mathcal{T}$, the *particle-hole symmetry* (PHS) $\mathcal{P}$, and the *sublattice symmetry* (SLS) $\mathcal{C}$. In particular, they will be presented with focus on their appearance in superconducting systems. Central elements from the presentation below is adapted from [4]. Assume that a system is described by the Hamiltonian H. Then, we say that U is a symmetry of H if U is an unitary (antiunitary) transformation, $U^\dagger = U^{-1}$ ($U^\dagger = -U^{-1}$), such that H commutes (anticommutes) with U.

Time-Reversal Symmetry This symmetry comes in two flavours. When describing a spinful system of spin-1/2 particles, the time-reversal operator is given by an antiunitary operator that squares to $-\mathbb{1}$,

$$\mathcal{T} = e^{-i\pi S_y}\kappa = i\sigma_y\kappa \quad \text{with} \quad \mathcal{T}^2 = -\mathbb{1}. \tag{2.24}$$

Above, σ_y is the second Pauli matrix acting on spin-degrees of freedom and κ the complex conjugation operator. However, for a spinless system one usually speaks of a reduced time-reversal operator with a scalar structure,

$$\mathcal{T} = \kappa \quad \text{with} \quad \mathcal{T}^2 = +1, \tag{2.25}$$

sometimes called the pseudo time-reversal symmetry operator. There are three options. The standard nomenclature is to say that TRS is -1 for Hamiltonians commuting with the spinful $\mathcal{T}$ operator, and that TRS is $+1$ for Hamiltonians commuting with the scalar $\mathcal{T}$ operator. Absence of the symmetry is denoted by saying that TRS is 0. A Hamiltonian commuting with the spinful time-reversal operator, $[H, \mathcal{T}] = 0$, has an important property; every energy eigenvalue, E_n, is at least doubly degenerate. This is known as *Kramer's degeneracy*. It can be proven by observing that if $|n\rangle$ is an eigenstate of H, then $\mathcal{T}|n\rangle$ is also an eigenstate of H with the same energy. And for a spinful system, these states are distinct since the spin of the state is flipped when the operator is applied.

Particle-Hole Symmetry The particle-hole symmetry exchanges the roles of creation and annihilation operators. There are generally three options for this symmetry as well. If it is present, the representative operator may square to either $\mathcal{P}^2 = \pm\mathbb{1}$. One says that PHS is ± 1 respectively. It could also be absent, in which case one says that PHS is 0. However, we make this presentation more specialized and exemplify how it appears for (spinless) superconducting Hamiltonians, referred to as BdG (*Bogoliubov-de-Gennes*) Hamiltonians, with PHS equal to $+1$. This is because we will study such models in this thesis, and it will suffice for the purpose of this chapter. The result of a mean field treatment of an electron-phonon interaction was seen in section 2.2. Motivated by this, consider the following general and

spinless lattice model in position space with all types of quadratic fermion couplings present,

$$H = \sum_{i,j} h_{i,j} c_i^\dagger c_j + \frac{1}{2} \sum_{i,j} \left(\Delta_{i,j}^* c_i c_j + \Delta_{i,j} c_i^\dagger c_j^\dagger \right). \tag{2.26}$$

This may be more compactly expressed by introducing

$$\boldsymbol{C} \equiv \begin{pmatrix} c_1, & c_2, & \ldots, & c_N, & c_1^\dagger, & c_2^\dagger, & \ldots, & c_N^\dagger \end{pmatrix}^T \quad \text{and} \quad \tilde{H} \equiv \begin{pmatrix} \Xi & \Delta \\ -\Delta^* & -\Xi^T \end{pmatrix}. \tag{2.27}$$

Above, Ξ and Δ are matrices with components $h_{i,j}$ and $\Delta_{i,j}$ respectively. Exploiting this notation allows us to express the Hamiltonian as

$$H = \frac{1}{2} \boldsymbol{C}^\dagger \tilde{H} \boldsymbol{C} + \frac{1}{2} \mathrm{Tr}\, \Xi. \tag{2.28}$$

The particle-hole operator of such systems is identified by an operator that exchanges the creation and annihilation parts of $\boldsymbol{C}$,

$$\mathcal{P} = \mathbb{1}_N \otimes \sigma_x \kappa = \begin{pmatrix} 0 & \mathbb{1}_N \\ \mathbb{1}_N & 0 \end{pmatrix} \kappa, \tag{2.29}$$

with $\mathbb{1}_N$ being the $N \times N$ identity matrix and σ_x the first Pauli matrix. The squared operator is here $\mathcal{P}^2 = +\mathbb{1}$ (PHS is +1). Furthermore, $\{\tilde{H}, \mathcal{P}\} = 0$. The symmetry does also manifest itself in k-space, but this will be seen explicitly for the Kitaev chain in Chapter 3. Any BdG Hamiltonian with the particle-hole symmetry present has a spectrum constraint; for every positive energy eigenvalue E_k, there is an eigenvalue with opposite sign, $-E_k$. Note, however, that each such pair of values correspond to only one physical particle excitation. This reminds immediately of the *Dirac sea*, where holes are the negative energy counterparts of ordinary matter. In superconducting systems, on the other hand, the holes represent an artificial doubling of the spectrum and do *not* correspond to physically distinct excitations. We will be reminded of this interpretation occasionally. Still, we will sometimes visualize both the positive and negative energy values for completeness.

Sublattice Symmetry The third symmetry is the *sublattice symmetry* (SLS), or sometimes called the chiral symmetry. It may be defined as the product of the other two symmetry operators,

$$\mathcal{C} = \mathcal{T}\mathcal{P}. \tag{2.30}$$

It is either present (SLS equal to 1) or absent (SLS equal to 0) and can always be chosen to square to $+\mathbb{1}$ [4]. More physically, it occurs for systems that can be divided into a block structure of two subsystems such that the Hamiltonian only

has non-zero matrix elements between the two subsystems.

The presence or absence of the three discrete symmetries discussed here, $\{\mathcal{T}, \mathcal{P}, \mathcal{C}\}$, is used to form the classification table of topological superconductors and insulators. As seen from our discussion above, we have thus nine combinations of $\mathcal{T}$ and $\mathcal{P}$; each can be 0 or ± 1. The sublattice symmetry is uniquely given in terms of the first two, except when both TRS and PHS are 0. In that case, SLS can either be 0 or 1. This means that there are ten symmetry classes in total. Out of these, four goes in the superconducting BdG category. The four BdG classes have the alienated names D, C, DIII and CI.[5]

In this nomenclature, the models that will be investigated later belong to the D class. This means that they have PHS equal to $+1$ and the two other symmetries absent. The key result of the classification is that a D class model with dimension $d = 1$ is expected to have a $\mathbb{Z}_2$ topological invariant, while $d = 2$ models have a $\mathbb{Z}$ topological invariant. For the one-dimensional Kitaev chain we will derive how the quantization of this number arise. In the notion of section 2.2, both models we will study have p-wave pairing. Why is this type of pairing important? We will see that the main feature of such pairing is that Majorana fermions may emerge as an edge phenomenon in the topological phase.

2.5 Majorana Fermions

In 1937 Ettore Majorana showed that fermions being identical to their own antiparticles were in accordance with Dirac's description from 1928 [19]. The Dirac equation for a relativistic spin-1/2 fermion field, ψ, of mass m reads

$$(i\gamma^\mu \partial_\mu - m)\psi = 0. \tag{2.31}$$

Dirac found a complex basis for the γ matrices satisfying the Dirac algebra, $\{\gamma^\mu, \gamma^\nu\} = 2\eta^{\mu\nu}\mathbb{1}_4$, with $\eta_{\mu\nu}$ being the Minkowski metric. This intrinsically demands complex field solutions. Majorana modified this view by finding a purely imaginary basis for the γ matrices,

$$\gamma_0 = \sigma_y \otimes \sigma_x, \quad \gamma_1 = i\sigma_x \otimes \mathbb{1}, \quad \gamma_2 = i\sigma_z \otimes \mathbb{1}, \quad \text{and} \quad \gamma_3 = i\sigma_y \otimes \sigma_y, \tag{2.32}$$

such that the field solutions were allowed to be real [20]. For an operator with a scalar structure, meaning that spin degrees of freedom are locked out, this is encoded in that the Majorana mode is created by an *hermitian operator*. This is not possible for a particle with electric charge. A Majorana fermion would therefore need to be electrically neutral. In condensed matter physics, Majorana fermions takes place in the form of *quasiparticle excitations* [11]. Generally, a quasiparticle is a collective

[5] The names of these classes are related to an old mathematical group classification due to Élie Cartan.

excitation with some properties similar to fundamental particles. In this context, a quasiparticle is a linear combination of creation and annihilation operators. A combination with equal weighting of particle and hole would qualify for electrical neutralness – a necessity for Majorana fermions.

However, spin introduces an obstacle in superconducting systems. In an ordinary s-wave superconductor for instance, the Cooper pairs are formed of electrons with opposite spins. This makes quasiparticles have the schematic form $a = uc_{\uparrow}^{\dagger} + vc_{\downarrow}$, with u and v being (complex) weights. We see that spin effectively hinders the possibility of $a = a^{\dagger}$. On the other hand, in a "spinless" superconductor, i.e. a system of fermions with only one active spin component, this problem is avoided. It could occur in a p-wave superconductor if the only active spin sector is $|\uparrow\uparrow\rangle$ or $|\downarrow\downarrow\rangle$. This is easy to phrase on theoretical grounds, but there are proposals on how to effectively induce spinless p-wave superconductivity in semiconducting in proximity of an ordinary s-wave superconductor [11]. We will not pursue these ideas. Instead, we explore superficially the most exciting application of Majorana fermions in condensed matter systems: their non-Abelian statistics. In order to do that and to understand why it must be realized in two (or perhaps even one [7]) spatial dimensions, it is necessary to discuss *anyons*.

2.6 Anyons

In the late 70s Jon Magne Leinaas and Jan Myrheim argued that identical particles in one and two dimensions can obey exchange statistics in a continuum of possibilities intermediate to that of fermions and bosons [1]. Frank Wilczek explored flux-tube models where the same type of particles emerged, and he introduced the term *anyons* [21]. In this section we recapitulate superficially the core of the original argument by Leinaas and Myrheim due to its fundamental implications.

One is used to think of quantum statistics as a symmetry constraint on many-particle wavefunctions during the exchange of two particles. Fermionic wavefunctions are antisymmetric while bosonic wavefunctions are symmetric. The starting point in [1] is to describe the configuration space of identical particles properly. By bringing the indistinguishability of identical particles into the formalism of the configuration space, the (artificial) need of imposing symmetry constraints disappears. Let X denote the configuration space of a single particle. It can for instance be $X = \mathbb{R}^3$ for a free particle in three dimensions. The configuration space of N identical particles is *not* simply the Cartesian product X^N, because permutations of particles do not represent distinct configurations. Assume therefore that the space remaining after excluding permutations of coordinates is denoted by $\mathcal{E}_d^N$ in d dimensions. Let also X be the Euclidean space $\mathbb{R}^d$. Then, $\mathcal{E}_d^N$ separates into a space containing the center-of-mass coordinate, $\mathbb{R}_{\mathrm{CM}}^d$, and a *relative space*, $r(d, N)$,

$$\mathcal{E}_d^N = \mathbb{R}_{\mathrm{CM}}^d \times r(d, N). \tag{2.33}$$

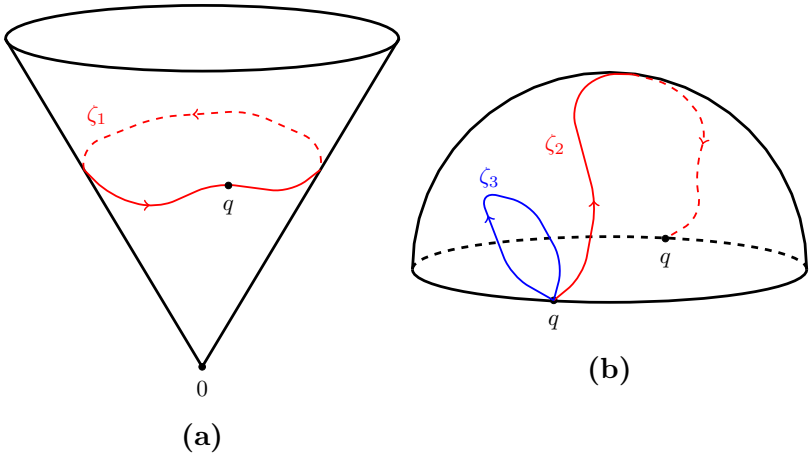

Figure 2.1: The relative spaces in two and three dimensions. **(a)** A closed curve ζ_1 representing a possible particle exchange in the relative space $r(2,2)$. The space may be constructed by cutting $\mathbb{R}^2$ along a line from the origin and folding it around this line *twice*, resulting in a cone. By this construction, $\pm\boldsymbol{x}$ are represented by the same point on the cone. The loop ζ_1 may not be deformed into a point without passing through the singular point. Furthermore, loops with a different number of windings around 0 can not be continuously deformed into each other. **(b)** The curves ζ_2 and ζ_3 are closed curves in the projective space $\mathbb{R}\mathrm{P}^2$. This space is represented here as the two-sphere S^2 with diametrically opposite points identified. The loop ζ_3 may be contracted to a point, but ζ_2 may not. However, the curve ζ_2 traversed twice, $\zeta_2 \circ \zeta_2$, can be contracted to a point. Hence, $\zeta_2 \circ \zeta_2$ can be continuously deformed into ζ_3.

The relative space $r(d,N)$ must be of dimension $d(N-1)$. Much of the remaining discussion concerns identifying and describing this relative space in the case of two particles, $N=2$. The relative space has a singular point where the positions of the two particles coincide. By removing the singular point, the relative space may further be separated into the real positive line and a $(d-1)$-dimensional *projective space* $\mathbb{R}\mathrm{P}^{d-1}$,[6]

$$r(d,2) \setminus \{0\} = (0,\infty) \times \mathbb{R}\mathrm{P}^{d-1}. \tag{2.34}$$

The first part of this product identifies the distance between the two particles, $|\boldsymbol{x}| = |\boldsymbol{x}_1 - \boldsymbol{x}_2|$, and the projective space specifies the direction of the line connecting them, $\pm\boldsymbol{x}/|\boldsymbol{x}|$. For instance, with $N = d = 2$, there are four degrees of freedom (d.o.f.) to uniquely specify the configuration space. In this case, $\mathbb{R}^2_{\mathrm{CM}}$ takes care of two d.o.f. and one is accounted for in the inter-particle distance. The final d.o.f. is taken care of by a point in $\mathbb{R}\mathrm{P}^1$, intuitively the angle between a coordinate axis and $\boldsymbol{x}$. Insights of physical significance follow from exploring the topological properties of the relative space, in particular how $d=2$ and $d \geq 3$ are fundamentally different in this aspect ($d=1$ is peculiar since interchange of particles must involve them passing through each other). An illustration of the fundamental difference is depicted in Figure 2.1.

[6]Technically, each point in $\mathbb{R}\mathrm{P}^{d-1}$ corresponds to a line though the origin of $\mathbb{R}^d$.

Consider first $d = 2$ and the relative space $r(2, 2)$. This space is the plane $\mathbb{R}^2$ with diametrically opposite points, $\boldsymbol{x}$ and $-\boldsymbol{x}$, identified. One may represent this by cutting the plane along a straight line from the origin and folding it around this line twice to form a cone with the origin 0 as the cone tip. By this construction, the points $\pm\boldsymbol{x}$ becomes identical on the cone. A possible exchange of two particles, illustrated by the curve ζ_1 in Figure 2.1(a), is encoded by a loop that circulates the singular point. This loop may not be shrunk to a point without passing through the singular point. Furthermore, loops with a different number of windings around the origin may not be continuously deformed into each other; they formally belong to different *homotopy classes*. The fact that there are an infinity of topologically distinct closed paths reflects a rich type of exchange statistics in $d = 2$. Exchanges in an N-anyon system is described by a group structure known as the *braid group*, B_N.

The deformation of closed paths is rather different in $d = 3$. The projective space $\mathbb{R}\mathrm{P}^2$ may be constructed from the two-sphere S^2 by identification of diametrically opposite points $\boldsymbol{x}$ and $-\boldsymbol{x}$. This is encoded in removal of, for instance, the southern hemisphere of S^2, which is what we have depicted in Figure 2.1(b). A closed curve in the projective space, representing a particle exchange, may or may not be contracted to a point. The curve ζ_2 in Figure 2.1(b) is closed but can not be contracted to a point when the endpoints are kept fixed. However, traversing it twice, $\zeta_2 \circ \zeta_2$ (a double exchange), results in a loop that may be continuously shrunk to a point. The two types of trajectories represent a single exchange (ζ_2) and no exchange (ζ_3), and they constitute all topologically distinct possibilities.

This fundamental difference in the topology of closed paths in two- and three-dimensional configuration spaces of identical particles becomes of physical significance in the quantum description. A linear operator encoding parallel displacement of wavefunctions in the Hilbert space generically takes the form

$$P = \exp(i\xi). \tag{2.35}$$

In three dimensions, the possibility of contracting any curve traversed twice, as depicted in 2.1(b), results in the condition that $P^2 = 1$. Thus, $\xi = 0$ and $\xi = \pi$, corresponding to bosons and fermions respectively, are the only options in three dimensions. In other words, the two-particle symmetry condition $\psi(\boldsymbol{x}_1, \boldsymbol{x}_2) = \pm\psi(\boldsymbol{x}_2, \boldsymbol{x}_1)$ is only implied for $d = 3$. In two dimensions, there is no particular restriction on the phase ξ. Any additional winding around the singular point in Figure 2.1(a) makes the two-particle wavefunction obtain a genuinely complex phase factor. The phase is, then, some characteristic quantity of the two-particle system, usually called the *statistical phase*. Exchanging anyons therefore yields $\psi(\boldsymbol{x}_1, \boldsymbol{x}_2) = e^{i\xi}\psi(\boldsymbol{x}_2, \boldsymbol{x}_1)$. Moreover, if ξ has a scalar structure the anyons are *Abelian* since the exchange operators commute. More exotic is the possibility of a matrix structure in the phase, $\psi_a(\boldsymbol{x}_1, \boldsymbol{x}_2) = e^{i\xi_\alpha T^\alpha_{ab}}\psi_b(\boldsymbol{x}_2, \boldsymbol{x}_1)$, such that new states might be involved after the particle interchange. This is the case for *non-Abelian* anyons.

2.6.1 Braids

In a system of N anyons with initial and final positions $\{\boldsymbol{r}_i\}_{i=1}^{N}$ at times t_i and t_f respectively, there is a one-to-one correspondence with elements in the braid group [12]. A N-braid is formally a set of N strings (or strands) confined within two horizontal lines with fixed endpoints. Each string intersects any plane between the two lines exactly once [22]. Physically, we may think of braids as world lines or particle trajectories visualized with time in the vertical direction and position projections in the horizontal direction; see Figure 2.2. The braid group B_N consists of $N-1$ discrete exchange generators $\{\sigma_i\}_{i=1}^{N-1}$. The operator σ_i is a counter-clockwise exchange of strings i and $i+1$. Consequently, σ_i^{-1} is a clockwise exchange of the same pair of strings. The defining properties of the generators are

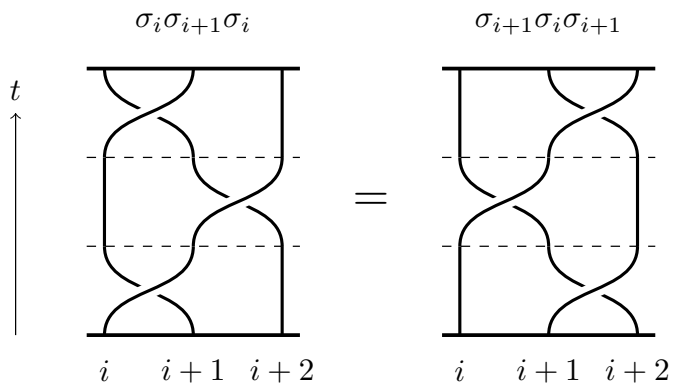

Figure 2.2: Diagrammatic illustration of the braid group identity $\sigma_i\sigma_{i+1}\sigma_i = \sigma_{i+1}\sigma_i\sigma_{i+1}$. The braids may be interpreted as particle world lines with time in the vertical direction and position projections in the horizontal direction.

$$\begin{aligned} \sigma_i\sigma_j &= \sigma_j\sigma_i \qquad \text{for } |i-j| \geq 2, \\ \sigma_i\sigma_{i+1}\sigma_i &= \sigma_{i+1}\sigma_i\sigma_{i+1} \quad \text{for } i \leq N-1. \end{aligned} \tag{2.36}$$

The (binary) group operator is just the consecutive application of exchange operations. In Figure 2.2 we have diagramatically depicted one of the Braid group identities from (2.36). The simplest (trivial) case is $N = 2$ with σ_1 as the only generator. The group B_2 is Abelian and isomorphic with the infinite cyclic group $(\mathbb{Z}, +)$. Applying σ_1 successively results in increased windings, and the identity element is never produced; the braid group is infinite. The picture becomes more complicated in the case of B_n for $n \geq 2$. In the next section we will explore a non-Abelian representation of B_4 that describes the exchange of Majorana modes bound to vortices.

2.7 Quantum Computation with Majoranas

The theoretical foundation of quantum computation appeared around 1980 with the basic idea of exploiting the superposition principle of quantum states. The interest of this subject grew quickly after it was discovered that certain types of problems

could be solved much faster on a quantum computer [12, 23]. For instance, simulating many-body quantum systems on a quantum computer can be done exponentially faster than on a classical computer. Algorithms as Grover's search algorithm, Shor's prime factorization algorithm and the Quantum Fourier transform algorithm should in principle show a significant decrease in computation time. Realizing a quantum computer is consequentially of great interest also outside academia; these algorithms have a vast range of applications.

The *qubit*, $|q\rangle$, is a quantum analogue of the classical bit. It is generally a superposition of the classical bit "states" 0 and 1, $|q\rangle = \alpha|0\rangle + \beta|1\rangle$. Quantum computation with qubits is based on three steps: initialization, unitary evolution and measurement [12]. And in order for the computation to be *universal*, meaning that any unitary operator can be represented, only a small set of elementary gates must be available. Among the greatest challenges to overcome in constructing a functioning quantum computer is handling *errors*, especially those caused by interactions with the environment. A quantum superposition is a delicate object that will collapse, ruining the computation, if influenced by any external interaction or measurement. Thus, overcoming *decoherence* caused by the environment becomes truly important in any realistic scheme.

The exotic properties of non-Abelian anyons may be used to form *topological qubits*. Topological qubits encode information in the braiding of particles. This makes them far superior when it comes to decoherence protection, at least in principle. Topological qubits can be highly non-local in the sense that they may be constructed from Majorana modes with arbitrary spatial separation. Moreover, this would make them robust against local perturbations, in contrast to computation schemes with spin based qubits. Below, we provide a simple example of how the braiding of four Majorana modes localized in vortices may result in a state space rotation. The example is inspired by [11].

2.7.1 Demonstration of Non-Abelian Braiding

Imagine a system of $2N$ well-separated vortices in a two-dimensional p-wave superconductor. Each vortex is assumed to bind a single Majorana zero mode. Note that we in Chapter 5 will establish a detailed understanding of how this takes place, especially how the Majorana modes are localized. In total, the set $\{\gamma_n\}_{n=1}^{2N}$ contains the distinct operators at our disposal. The Majorana operators satisfy the defining properties

$$\gamma_n = \gamma_n^\dagger \quad \text{and} \quad [H, \gamma_n] = 0. \tag{2.37}$$

They are assumed to satisfy fundamental anticommutation relations similar to fermions, adopting a common normalization convention [11],

$$\{\gamma_n, \gamma_m\} = 2\delta_{n,m}. \tag{2.38}$$

Note how this last property makes it difficult to speak of the occupancy of a Majorana state. Trying to construct a number operator leads to the trivial result $n_{\mathrm{MF}} = \gamma_n^\dagger \gamma_n = 1$ (since $\gamma_n^2 = 1$). In other words, a Majorana mode is in this sense always filled, and counting the occupancies is meaningless. Still, we may pair up two Majorana operators to form an ordinary fermionic state. This pairing is merely a choice of basis, and it clarifies why we need $2N$ Majorana modes to form N fermionic operators. We define

$$c_j \equiv \frac{1}{2}(\gamma_{2j-1} + i\gamma_{2j}). \tag{2.39}$$

The reader may look at Figure 5.4 at this point to get a cartoon picture of the situation. These operators can readily be checked to satisfy the canonical relations $\{c_i^\dagger, c_j\} = \delta_{i,j}$ and $\{c_i, c_j\} = \{c_i^\dagger, c_j^\dagger\} = 0$. Occupation operators, $n_j = c_j^\dagger c_j$, can conveniently be formed, and they are used to denote the ground state manifold in terms of the occupancy state $|n_1, n_2, \ldots, n_N\rangle$. For the matter of this demonstration we simply state the result of adiabatically exchanging the vortices containing γ_j and γ_{j+1} in a clockwise manner. This discrete transformation is the key result of Ivanov's derivation [6],

$$\sigma_i : \begin{cases} \gamma_i \mapsto \gamma_{i+1} \\ \gamma_{i+1} \mapsto -\gamma_i \\ \gamma_j \mapsto \gamma_j \qquad \text{for } j \notin \{i, i+1\} \end{cases}. \tag{2.40}$$

In section 5.6 we will suggest an argument that results in the same transformation rule. Consider the minimal (and non-trivial) example with two fermionic degrees of freedom, $N = 2$. Assume that the initial ground state of the system is $|n_1, n_2\rangle \equiv |n_1\rangle \otimes |n_2\rangle$, with n_1 is the occupation number of the fermionic state formed by γ_1 and γ_2 according to (2.39). Similarly, n_2 consists of γ_3 and γ_4. Hence, $|n_1, n_2\rangle$ is an eigenstate of $n_1 = c_1^\dagger c_1$ and $n_2 = c_2^\dagger c_2$ by assumption. In order to study the action of σ_i on $|n_1, n_2\rangle$, we need a unitary representation of the transformation rule in (2.40), meaning an operator U_i satisfying

$$\sigma_i(\gamma_j) = U_i \gamma_j U_i^\dagger. \tag{2.41}$$

Up to an undetermined phase factor, the unitary operator satisfying this is given by

$$U_i = \exp\left(\frac{\pi}{4}\gamma_{i+1}\gamma_i\right) = \frac{1}{\sqrt{2}}(\mathbb{1} + \gamma_{i+1}\gamma_i). \tag{2.42}$$

One may readily check that it satisfies the Braid group properties in (2.36). The operators $\{U_i\}_{i=1}^3$ constitute a representation of the Braid group, in this case B_4. The operator U_2 affects γ_2 and γ_3 such that the state $|n_1, n_2\rangle$ is possibly left in a linear combination of the four states spanning the ground state manifold,

$$\mathcal{M} = \{|0,0\rangle, |1,0\rangle, |0,1\rangle, |1,1\rangle\}. \tag{2.43}$$

We define the fully filled state as $|1,1\rangle \equiv c_1^\dagger c_2^\dagger |0,0\rangle$ (the order is of importance in what follows). Our system consists of two fermionic operators, $c_1 = \frac{1}{2}(\gamma_1 + i\gamma_2)$ and $c_2 = \frac{1}{2}(\gamma_3 + i\gamma_4)$, with the inverse relations

$$\gamma_1 = c_1 + c_1^\dagger, \quad \gamma_2 = -i(c_1 - c_1^\dagger), \quad \gamma_3 = c_2 + c_2^\dagger, \quad \gamma_4 = -i(c_2 - c_2^\dagger). \tag{2.44}$$

Thus, acting with single Majorana operators on $|n_1, n_2\rangle$ can be summarized as

$$\begin{aligned}
\gamma_1 |n_1, n_2\rangle &= |1 - n_1, n_2\rangle , \\
\gamma_2 |n_1, n_2\rangle &= i(-1)^{n_1} |1 - n_1, n_2\rangle , \\
\gamma_3 |n_1, n_2\rangle &= (-1)^{n_1} |n_1, 1 - n_2\rangle , \\
\gamma_4 |n_1, n_2\rangle &= i(-1)^{n_1+n_2} |n_1, 1 - n_2\rangle .
\end{aligned} \tag{2.45}$$

Hence, we have the tools needed to see how U_1, U_2 and U_3 act on the occupancy states,

$$\begin{aligned}
U_1 |n_1, n_2\rangle &= \frac{1}{\sqrt{2}}\Big(1 + i(-1)^{1-n_1}\Big) |n_1, n_2\rangle , \\
U_2 |n_1, n_2\rangle &= \frac{1}{\sqrt{2}}\Big(|n_1, n_2\rangle - i |1 - n_1, 1 - n_2\rangle \Big), \\
U_3 |n_1, n_2\rangle &= \frac{1}{\sqrt{2}}\Big(1 + i(-1)^{2n_1-n_2+1}\Big) |n_1, n_2\rangle .
\end{aligned} \tag{2.46}$$

The two-qubit state $|n_1, n_2\rangle$ is an eigenstate of U_1 and U_3 as anticipated. However, the operator U_2 is seen to rotate the state into a linear combination of two states. In other words, *the representation is non-Abelian, and the order of which one successively applies U operators do matter.* Alternatively, we may represent the operators as matrices, with the consequence that U_2 is non-diagonal. We do this with the basis states in the same order as in (2.43):

$$U_1 = \frac{1}{\sqrt{2}}\begin{pmatrix} 1-i & 0 & 0 & 0 \\ 0 & 1+i & 0 & 0 \\ 0 & 0 & 1-i & 0 \\ 0 & 0 & 0 & 1+i \end{pmatrix}, \quad U_2 = \frac{1}{\sqrt{2}}\begin{pmatrix} 1 & 0 & 0 & -i \\ 0 & 1 & -i & 0 \\ 0 & -i & 1 & 0 \\ -i & 0 & 0 & 1 \end{pmatrix}, \quad U_3 = \frac{1}{\sqrt{2}}\begin{pmatrix} 1-i & 0 & 0 & 0 \\ 0 & 1-i & 0 & 0 \\ 0 & 0 & 1+i & 0 \\ 0 & 0 & 0 & 1+i \end{pmatrix}. \tag{2.47}$$

Unfortunately, the two-qubit braiding operators U_1, U_2 and U_3 alone do not allow for universal quantum computation; they do not span all unitary transformations [12]. However, there are schemes, even though we will not pursue them, on how to approximate any quantum computation to arbitrary accuracy with only the braid operations. Proposals have also been put forward on how to extend the set of braiding operations with the gates needed to obtain universal computation.

Chapter 3

The Closed Kitaev Chain

We open the content of this thesis with a detailed study of a toy model of historical impact. The motivation is to fill in details, and to gain a more complete understanding than obtained with the presentation by Jason Alicea in [11]. By considering closed boundary conditions, we will be able to analytically derive the energy spectrum and characterize the ground state. We explore how a certain Berry phase distinguishes the two topological phases of the model. With this classification in mind, it is of fundamental interest to study if fermionic correlation functions show signs of the topological phase transition. This is done numerically.

In 2001 Alexei Kitaev proposed a toy model for spinless fermions on a one-dimensional superconducting chain [10]. The model captures concisely the physics of topological phenomena, and it has proven to be central in the field of topological superconductivity. The Kitaev Hamiltonian for a closed system is

$$H = -\mu \sum_{x=1}^{N} c_x^\dagger c_x - \frac{1}{2} \sum_{x=1}^{N} \Big(t c_x^\dagger c_{x+1} + \Delta e^{i\phi} c_x c_{x+1} + \text{h.c.} \Big). \tag{3.1}$$

Above, c_x denotes the annihilation operator of a spinless fermion at site x. We define $c_{N+1} \equiv c_1$ so that the N-site chain obeys periodic boundary conditions. The chemical potential is denoted by μ, t is the real and positive neighbouring site hopping strength, Δ is the superconducting energy gap (the order parameter) and ϕ a superconducting phase. The fermion operators obey canonical anticommutation relations,

$$\{c_x, c_{x'}^\dagger\} = \delta_{x,x'} \quad \text{and} \quad \{c_x, c_{x'}\} = \{c_x^\dagger, c_{x'}^\dagger\} = 0. \tag{3.2}$$

The discrete Kitaev chain has a notable similarity with the Ising model. Despite the affinity with onsite terms and nearest neighbour couplings along the chain, the Ising model is semi-classical – classical in the sense of involving commuting variables and quantum mechanical in the sense of describing quantized spins – while the Kitaev chain plays the role of being a truly quantum analogue.

3.1 Bogoliubov-de-Gennes Hamiltonian

Discrete Fourier transforms c_k of the operators c_x are introduced. The context should reveal clearly when we refer to momentum space operators (subscript k or l) and when we refer to real space operators (subscript x or y),

$$c_k = \frac{1}{\sqrt{N}} \sum_{x=1}^{N} e^{ikx\frac{2\pi}{N}} c_x \quad \text{and} \quad c_x = \frac{1}{\sqrt{N}} \sum_{k=1}^{N} e^{-ikx\frac{2\pi}{N}} c_k. \tag{3.3}$$

The Kronecker delta function $\delta_{k,k'}$ of period N in this discrete formulation may be expressed in terms of a sum of complex exponentials,

$$\delta_{k,k'} = \frac{1}{N} \sum_{x=1}^{N} e^{-i(k-k')x\frac{2\pi}{N}}, \tag{3.4}$$

and will appear in the deduction below. This formula may be proven by using the summation of a geometric series. The Fourier transformed operators are defined for k-values $1 \leq k \leq N$, but we can by periodicity extend the allowed range. In particular, when for example $-k$ appears in the following deduction, it is understood to be equivalent to $N-k$. The transformed operators obey similar anticommutation relations as in equation (3.2). This follows from (3.2), (3.3) and (3.4),

$$\{c_k^\dagger, c_{k'}\} = \frac{1}{N} \sum_{x=1}^{N} e^{-ikx\frac{2\pi}{N}} \sum_{x'=1}^{N} e^{ik'x'\frac{2\pi}{N}} \{c_x^\dagger, c_{x'}\} = \delta_{k,k'}. \tag{3.5}$$

The relations $\{c_k^\dagger, c_{k'}^\dagger\} = \{c_k, c_{k'}\} = 0$ follow analogously.

3.1.1 Momentum Representation

The different terms in the Hamiltonian are brought to Fourier space. First, the onsite terms:

$$\begin{aligned} H_1 &\equiv -\mu \sum_{x=1}^{N} c_x^\dagger c_x \\ &= -\frac{\mu}{N} \sum_{k,k'=1}^{N} \sum_{x=1}^{N} e^{i(k-k')x\frac{2\pi}{N}} c_k^\dagger c_{k'} \\ &= -\mu \sum_{k=1}^{N} c_k^\dagger c_k \\ &= -\frac{\mu}{2} \sum_{k=1}^{N} (c_k^\dagger c_k - c_{-k} c_{-k}^\dagger) - \frac{1}{2}\mu N. \end{aligned} \tag{3.6}$$

The last term is constant, and we redefine the ground level energy by neglecting it. Next, the kinetic terms are transformed:

$$\begin{aligned} H_2 &\equiv -\frac{t}{2}\sum_{x=1}^{N}(c_x^\dagger c_{x+1} + \text{h.c.}) \\ &= -\frac{1}{2}\frac{t}{N}\sum_{k,k'=1}^{N}\sum_{x=1}^{N}(e^{i[-kx+k'(x+1)]\frac{2\pi}{N}}c_k^\dagger c_{k'} + \text{h.c.}) \\ &= -\frac{t}{2}\sum_{k=1}^{N}(e^{ik\frac{2\pi}{N}}c_k^\dagger c_k + \text{h.c.}) \\ &= -t\sum_{k=1}^{N}\frac{1}{2}(e^{ik\frac{2\pi}{N}} + e^{-ik\frac{2\pi}{N}})c_k^\dagger c_k \\ &= -\frac{t}{2}\sum_{k=1}^{N}\cos\left(\frac{2\pi k}{N}\right)(c_k^\dagger c_k - c_{-k}c_{-k}^\dagger) - \frac{t}{2}\sum_{k=1}^{N}\cos\left(\frac{2\pi k}{N}\right). \end{aligned} \tag{3.7}$$

Again, the last term is constant and may be neglected. Finally, we transform the superconducting Cooper terms:

$$\begin{aligned} H_3 &\equiv -\frac{1}{2}\Delta\sum_{x=1}^{N}(e^{i\phi}c_x c_{x+1} + \text{h.c.}) \\ &= -\frac{1}{2}\frac{\Delta}{N}\sum_{k,k'=1}^{N}\sum_{x=1}^{N}(e^{i\phi}e^{i[kx+k'(x+1)]\frac{2\pi}{N}}c_k c_{k'} + \text{h.c.}) \\ &= -\frac{\Delta}{2}\sum_{k=1}^{N}(e^{i\phi}e^{-ik\frac{2\pi}{N}}c_k c_{-k} + \text{h.c.}) \\ &= -\frac{\Delta}{2}\sum_{k=1}^{N}\left(\frac{e^{i\phi}}{2}\left(e^{-ik\frac{2\pi}{N}} - e^{ik\frac{2\pi}{N}}\right)c_k c_{-k} + \text{h.c.}\right) \\ &= \frac{\Delta}{2}\sum_{k=1}^{N}\left(ie^{i\phi}\sin\left(\frac{2\pi k}{N}\right)c_k c_{-k} + \text{h.c.}\right). \end{aligned} \tag{3.8}$$

To simplify notation we denote $k' = \frac{2\pi k}{N} \in \left[\frac{2\pi}{N}, 2\pi\right]$ and relabel $k' \to k$. This means that when $-k$ appears in the following, it is understood to be equivalent to $2\pi - k$. The operator $c_k^\dagger$ creates a fermion excitation of momentum k. We introduce $\mathcal{B}$ as the *Brillouin zone*; the discrete set of momentum numbers,

$$\mathcal{B} = \left\{\frac{2\pi}{N}n \mid n \in \{1, 2, \ldots, N\}\right\}. \tag{3.9}$$

In the continuum limit, $N \to \infty$, $\mathcal{B}$ approaches the interval $(0, 2\pi]$. We stress that there are two particular values of k that must be treated with care. Trying to form pairs of k and $-k$ from $\mathcal{B}$, the two values $k = 0$ and $k = \pi$ are the only ones that do not have a pairing partner. This is related to the formation of Cooper pairs in

the ground state. The values $k = 0$ and $k = \pi$ will be of importance later, and they appear in $\mathcal{B}$ as follows:

$$\begin{aligned} &k = 0 \in \mathcal{B} \text{ and } k = \pi \in \mathcal{B} \text{ if } N \text{ is even,} \\ &k = 0 \in \mathcal{B} \text{ and } k = \pi \notin \mathcal{B} \text{ if } N \text{ is odd.} \end{aligned} \tag{3.10}$$

Two functions are introduced to compactify the notation,

$$\epsilon_k \equiv -t\cos k - \mu \quad \text{and} \quad \Delta_k \equiv -i\Delta e^{i\phi}\sin k. \tag{3.11}$$

The terms may be collected to express the transformed Hamiltonian as

$$\begin{aligned} H &= H_1 + H_2 + H_3 \\ &= \frac{1}{2}\sum_{k\in\mathcal{B}} \left(\epsilon_k(c_k^\dagger c_k - c_{-k}c_{-k}^\dagger) + \Delta_k c_{-k}c_k + \Delta_k^* c_k^\dagger c_{-k}^\dagger\right) \\ &= \frac{1}{2}\sum_{k\in\mathcal{B}} \begin{pmatrix} c_k^\dagger, & c_{-k} \end{pmatrix} \begin{pmatrix} \epsilon_k & \Delta_k^* \\ \Delta_k & -\epsilon_k \end{pmatrix} \begin{pmatrix} c_k \\ c_{-k}^\dagger \end{pmatrix} \\ &= \frac{1}{2}\sum_{k\in\mathcal{B}} \boldsymbol{C}_k^\dagger \mathcal{H}_k \boldsymbol{C}_k, \end{aligned} \tag{3.12}$$

with

$$\boldsymbol{C}_k \equiv \begin{pmatrix} c_k \\ c_{-k}^\dagger \end{pmatrix} \quad \text{and} \quad \mathcal{H}_k \equiv \begin{pmatrix} \epsilon_k & \Delta_k^* \\ \Delta_k & -\epsilon_k \end{pmatrix}. \tag{3.13}$$

The matrix $\mathcal{H}_k$ acts as a two-level Hamiltonian that relates particles and holes of opposite momenta. It is referred to as the BdG Hamiltonian. The particle-hole symmetry that was mentioned in section 2.4 is visible in $\mathcal{H}_k$. This symmetry can be phrased in terms of a single-spinor operator τ, in contrast to $\mathcal{P}$ from section 2.4, which acted on a vector containing all fermion operators,

$$\tau \equiv \begin{pmatrix} 0 & -1 \\ 1 & 0 \end{pmatrix} \kappa = -i\sigma_y \kappa, \tag{3.14}$$

with κ as the complex conjugation operator. Letting τ act on a spinor has the effect of exchanging particles and holes.[1] By construction, τ anticommutes with $\mathcal{H}_k$,

$$\{\mathcal{H}_k, \tau\} = 0. \tag{3.15}$$

[1] It could be noted that there is an apparent similarity between τ and the time-reversal operator $\mathcal{T}$ discussed in section 2.4. The Kitaev chain consists of spinless fermions and the scalar time-reversal operator is simply $\mathcal{T} = \kappa$. This is, however, generally not a symmetry of the Kitaev chain. If, on the other hand, both t and $\Delta e^{i\phi}$ are strictly real (i.e. $\phi = n\pi$ for some integer n), then $[H, \mathcal{T}] = 0$ and the model obeys an additional symmetry, TRS equal to $+1$. This is subtle, but it means that the model moves from symmetry class D to BDI in the classification table [4]. We will return to this when studying the Kitaev chain with open boundaries.

This implies that the spectrum of $\mathcal{H}_k$ is symmetric, i.e. that the energy eigenvalues come in pairs of opposite signs. More explicitly, the eigenvalues of $\mathcal{H}_k$ are

$$\pm E_k = \pm\sqrt{\epsilon_k^2 + |\Delta_k|^2} = \pm\sqrt{(t\cos k + \mu)^2 + \Delta^2 \sin^2 k}. \tag{3.16}$$

The function E_k reveals that *the spectrum is gapped for all μ except at the two values $\mu = \pm t$*. A plot of the spectrum is shown in Figure 3.1. Assume now that $\begin{pmatrix} u_k^*, & v_k^* \end{pmatrix}^T$ is the eigenvector belonging to the positive eigenvalue $+E_k$ (the coefficients are chosen this way for convenience). In other words,

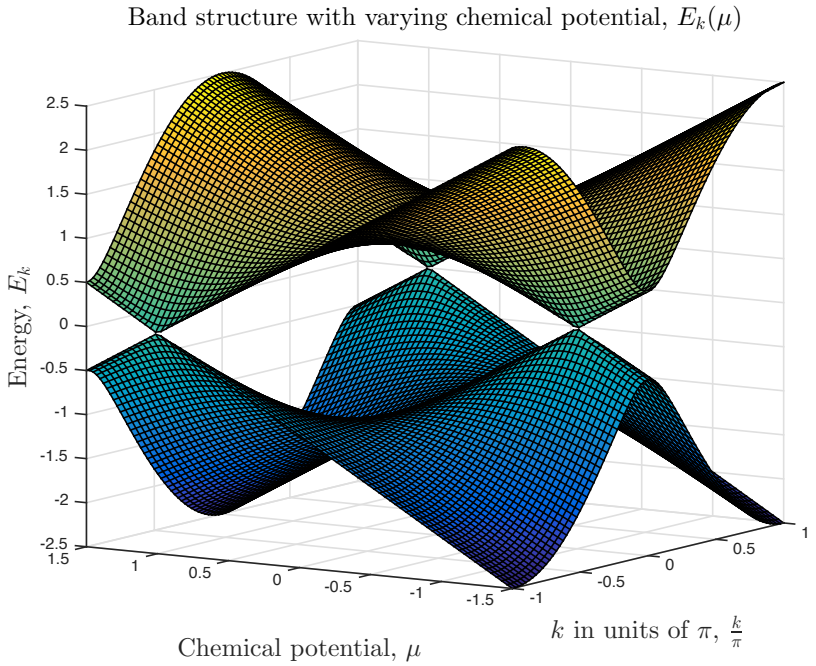

Figure 3.1: Energy spectrum as function of momentum $k \in (-\pi, \pi]$ and chemical potential μ in the range $\mu \in [-1.5t, 1.5t]$. Parameters $\Delta = t = 1.0$ were fixed. The gap closes at $k = \pi$ for $\mu = t$ and at $k = 0$ for $\mu = -t$.

$$\begin{aligned} \begin{pmatrix} \epsilon_k & \Delta_k^* \\ \Delta_k & -\epsilon_k \end{pmatrix} \begin{pmatrix} u_k^* \\ v_k^* \end{pmatrix} = E_k \begin{pmatrix} u_k^* \\ v_k^* \end{pmatrix} \Rightarrow \\ v_k^* = \frac{E_k - \epsilon_k}{\Delta_k^*} u_k^*. \end{aligned} \tag{3.17}$$

Normalization of the eigenvector is imposed,

$$\begin{aligned} |u_k|^2 + |v_k|^2 = 1 \Rightarrow \\ |u_k|^2 = \left(1 + \frac{(E_k - \epsilon_k)^2}{|\Delta_k|^2}\right)^{-1} = \frac{E_k + \epsilon_k}{2E_k}. \end{aligned} \tag{3.18}$$

The squared coefficients, $|u_k|^2$ and $|v_k|^2$, can alternatively be expressed as

$$|u_k|^2 = \frac{1}{2}\left(1 + \frac{\epsilon_k}{E_k}\right) \quad \text{and} \quad |v_k|^2 = \frac{1}{2}\left(1 - \frac{\epsilon_k}{E_k}\right). \tag{3.19}$$

Sometimes, they are referred to as *coherence factors* [24]. Some key observations are summarized beneath.

$$\begin{aligned}
&|u_k| \to 0 \text{ and } |v_k| \to 1 \text{ as } \mu \gg t, \\
&|u_k| \to 1 \text{ and } |v_k| \to 0 \text{ as } \mu \ll -t, \\
&|u_0| = \begin{cases} 0 & \text{if } \mu > -t \\ 1 & \text{if } \mu < -t \end{cases} \text{ and } |v_0| = \begin{cases} 1 & \text{if } \mu > -t \\ 0 & \text{if } \mu < -t \end{cases}, \\
&|u_\pi| = \begin{cases} 0 & \text{if } \mu > t \\ 1 & \text{if } \mu < t \end{cases} \text{ and } |v_\pi| = \begin{cases} 1 & \text{if } \mu > t \\ 0 & \text{if } \mu < t \end{cases}.
\end{aligned} \tag{3.20}$$

We are generally free to choose u_k and v_k up to k-dependent (complex) phase factors, $e^{i\alpha_k}$. Following the convention by Read and Green [24], one of u_k or v_k can be taken to be real and positive. Let therefore $u_k \in \mathbb{R}^+$ be given by the positive square root of equation (3.18) with $u_{-k} = u_k$. The other coefficient is allowed to be complex, $v_k \in \mathbb{C}$, and is odd in k, $v_{-k} = -v_k$. Both properties of v_k are given by equation (3.17), ensured by Δ_k^* in the denominator; recall that Δ_k is both complex and odd in k. Since the operator τ anticommutes with $\mathcal{H}_k$ we have that

$$\mathcal{H}_k \tau \begin{pmatrix} u_k^* \\ v_k^* \end{pmatrix} = -\tau \mathcal{H}_k \begin{pmatrix} u_k^* \\ v_k^* \end{pmatrix} = -E_k \tau \begin{pmatrix} u_k^* \\ v_k^* \end{pmatrix}. \tag{3.21}$$

Hence, the second eigenvector of $\mathcal{H}_k$ is $\tau \begin{pmatrix} u_k^*, & v_k^* \end{pmatrix}^T = \begin{pmatrix} -v_k, & u_k \end{pmatrix}^T$.

3.1.2 Quasiparticles and the Spectral Decomposition

The tools needed to diagonalize $\mathcal{H}_k$ are readily available. According to the matrix diagonalization theorem, define U such that

$$\mathcal{H}_k = UDU^\dagger \quad \text{with} \quad D = \begin{pmatrix} E_k & 0 \\ 0 & -E_k \end{pmatrix}, \tag{3.22}$$

and

$$U = \begin{pmatrix} u_k^* & -v_k \\ v_k^* & u_k \end{pmatrix} = \frac{1}{\sqrt{2E_k}} \begin{pmatrix} \sqrt{E_k + \epsilon_k} & -\frac{\Delta_k^*}{|\Delta_k|}\sqrt{E_k - \epsilon_k} \\ \frac{\Delta_k}{|\Delta_k|}\sqrt{E_k - \epsilon_k} & \sqrt{E_k + \epsilon_k} \end{pmatrix}. \tag{3.23}$$

A new operator basis is introduced; let *quasiparticle annihilation operators* be denoted by a_k. They are defined according to

$$\begin{pmatrix} a_k \\ a_{-k}^\dagger \end{pmatrix} \equiv \begin{pmatrix} u_k & v_k \\ -v_k^* & u_k^* \end{pmatrix} \begin{pmatrix} c_k \\ c_{-k}^\dagger \end{pmatrix}. \tag{3.24}$$

These operators, a_k, are thus linear combinations of creation and annihilation operators with opposite momenta. A quasiparticle excitation, created by $a_k^\dagger$, will carry a fraction of the normal fermion charge. At this point we note from the explicit expressions of u_k and v_k certain characteristics of such an excitation. In the limit $\mu \ll -t$ the operator a_k reduces to $a_k \to c_k$. Similarly, $a_k \to c_k^\dagger$ as $\mu \gg t$. Furthermore, observe that the quasiparticle operators obey the same anticommutation relations as normal fermions, found by using (3.5) and (3.18),

$$\begin{aligned} \{a_k, a_{k'}^\dagger\} &= \{u_k c_k + v_k c_{-k}^\dagger, u_{k'}^* c_{k'}^\dagger + v_{k'}^* c_{-k'}\} \\ &= \left(|u_k|^2 + |v_k|^2\right) \delta_{k,k'} \\ &= \delta_{k,k'}. \end{aligned} \tag{3.25}$$

The relations $\{a_k, a_{k'}\} = \{a_k^\dagger, a_{k'}^\dagger\} = 0$ follow as well. This means that the quasiparticles obey Fermi-Dirac statistics. In other words, $(a_k)^2 = (a_k^\dagger)^2 = 0$. Finally, the spectral decomposition of the Hamiltonian is

$$\begin{aligned} H &= \frac{1}{2} \sum_{k \in \mathcal{B}} \boldsymbol{C}_k^\dagger \mathcal{H}_k \boldsymbol{C}_k \\ &= \frac{1}{2} \sum_{k \in \mathcal{B}} \boldsymbol{C}_k^\dagger U \mathcal{D} U^\dagger \boldsymbol{C}_k \\ &= \frac{1}{2} \sum_{k \in \mathcal{B}} \begin{pmatrix} a_k^\dagger, & a_{-k} \end{pmatrix} \begin{pmatrix} E_k & 0 \\ 0 & -E_k \end{pmatrix} \begin{pmatrix} a_k \\ a_{-k}^\dagger \end{pmatrix} \\ &= \frac{1}{2} \sum_{k \in \mathcal{B}} E_k (a_k^\dagger a_k - a_{-k} a_{-k}^\dagger) \\ &= \sum_{k \in \mathcal{B}} E_k a_k^\dagger a_k - \frac{1}{2} \sum_{k \in \mathcal{B}} E_k. \end{aligned} \tag{3.26}$$

Again, a constant energy term arises. It can be neglected by a redefinition of the ground level energy. The Hamiltonian is diagonal in the new operators, indicating that quasiparticles are non-interacting. Moreover, they act as the fundamental excitations of the system. During the derivation we encountered two energy eigenvalues, $\pm E_k$, for each value of k. The above expression reveals, however, that quasiparticles are exclusively positive energy excitations. Hence, we will only care about the upper band in Figure 3.1 from this point. If one instead were to define $b_k = a_k^\dagger$ as the quasiparticle operators – this is essentially equivalent to interchanging particles and holes – the result would have had opposite sign. The Hilbert space governed by the many-body Hamiltonian (3.26) is 2^N-dimensional since each quasiparticle site can be either filled or empty.

3.2 The Ground State

Let a single-particle vacuum state of Fourier mode k be denoted by $|0,k\rangle$. This state is by definition annihilated by the c_k operator. Similarly, with $|0,x\rangle$ we refer to an empty fermion state with real space position x. The Fourier space N-body vacuum state, denoted simply by $|0\rangle$, is formally a tensor product state of single-particle vacuum states,

$$|0\rangle \equiv \bigotimes_{k\in\mathcal{B}} |0,k\rangle \,. \tag{3.27}$$

The ground state of the Hamiltonian (3.26) is denoted by $|\Omega\rangle$. Since $E_k \geq 0$ with equality only possible for $k = 0$ or $k = \pi$, the ground state can be constructed to have zero energy if it is annihilated by all the a_k operators. Of course, the constant energy term in the Hamiltonian (3.26) is neglected. The defining criterion of $|\Omega\rangle$ is thus that

$$a_k |\Omega\rangle = 0 \; \forall k \in \mathcal{B}. \tag{3.28}$$

In other words, the ground state contains no quasiparticles. This construction is achieved by expressing $|\Omega\rangle$ as the product

$$|\Omega\rangle = M \prod_{k\in\mathcal{B}} a_k |0\rangle \,, \tag{3.29}$$

with M as a normalization constant. It ensures $\forall l \in \mathcal{B}$ that

$$a_l |\Omega\rangle = M a_l \prod_{k\in\mathcal{B}} a_k |0\rangle = M' \prod_{k\in\mathcal{B},k\neq l} a_k (a_l)^2 |0\rangle = 0. \tag{3.30}$$

The constant M' is possibly different from M by a sign from the anticommutation relations. It is instructive to express $|\Omega\rangle$ as a product of paired states with opposite momenta. This is done by letting the product run over half of the values in $\mathcal{B}$. Observe that

$$\begin{aligned} a_k a_{-k} |0\rangle &= (u_k c_k + v_k c_{-k}^\dagger)(u_k c_{-k} - v_k c_k^\dagger) |0\rangle \\ &= -v_k (u_k + v_k c_{-k}^\dagger c_k^\dagger) |0\rangle \,. \end{aligned} \tag{3.31}$$

A subset of $\mathcal{B}$ is defined for notational convenience,

$$\mathcal{B}^+ \equiv \{ l \in \mathcal{B} \mid l < \pi \} \subset \mathcal{B}. \tag{3.32}$$

The Cooper paired part of $|\Omega\rangle$ can therefore be expressed according to (3.31) as

$$\prod_{k\in\mathcal{B}^+} a_k a_{-k}\,|0\rangle \propto \prod_{k\in\mathcal{B}^+} (1+g_k c_{-k}^\dagger c_k^\dagger)\,|0\rangle = \prod_{k\in\mathcal{B}^+} e^{g_k c_{-k}^\dagger c_k^\dagger}\,|0\rangle\,, \tag{3.33}$$

with

$$g_k \equiv \frac{v_k}{u_k} = \frac{\Delta_k^*}{E_k+\epsilon_k}. \tag{3.34}$$

Terms of power greater than one, when expanding the exponential operator in (3.33), vanishes due to Fermi-Dirac statistics, $(c_k)^2 = (c_k^\dagger)^2 = 0$. As pointed out earlier, it is important to include the single operators that can not be paired up as above, $k = 0$ and $k = \pi$, separately. Consequently, we are forced to make a distinction between N being even or odd. In addition, the parameter regime will have a critical impact on the two single operators a_0 and a_π, determined by the properties of $|u_0|$ and $|u_\pi|$ as summarized in (3.20). Up to the possible phase factor in v_k, we have that

$$a_0 = \begin{cases} c_0 & \text{if } \mu < -t \\ c_0^\dagger & \text{if } \mu > -t \end{cases} \quad \text{and} \quad a_\pi = \begin{cases} c_\pi & \text{if } \mu < t \\ c_\pi^\dagger & \text{if } \mu > t \end{cases}. \tag{3.35}$$

Consider an even number of sites N, so that both modes $k = 0$ and $k = \pi$ are present. Using (3.33), and making sure that both $a_0\,|\Omega\rangle = a_\pi\,|\Omega\rangle = 0$, yields the final result result,

$$\boxed{|\Omega\rangle = A \prod_{k\in\mathcal{B}^+} e^{g_k c_{-k}^\dagger c_k^\dagger} \left(\begin{cases} 1 & \text{if } \mu < -t \\ c_0^\dagger & \text{if } |\mu| < t \\ c_0^\dagger c_\pi^\dagger & \text{if } \mu > t \end{cases} \right) |0\rangle}\,. \tag{3.36}$$

Above, A is a normalization constant. Note that $|\Omega\rangle$ is constructed by pairs of fermions with opposite momenta in accordance with the BCS result [3]. However, the two unpaired operators alter the number of fermions in the ground state depending on the parameter regime. It could also be mentioned that this result gives a more precise description than the somewhat loosely stated ground state in equation (8) in [11]. The number of fermions being even or odd will be denoted by *fermion parity*. It may be encoded by the operator

$$P \equiv (-1)^{\sum_{k\in\mathcal{B}} n_k} = e^{i\pi \sum_{k\in\mathcal{B}} n_k} = \prod_{k\in\mathcal{B}} (1-2n_k)\,. \tag{3.37}$$

We return more thoroughly to the impact of this operator in section 5.6. The eigenvalue, $+1$ (-1), corresponds to an even (odd) number of fermions. It is now explicitly seen that

$$\langle P\rangle_\Omega = \langle\Omega|P|\Omega\rangle = \begin{cases} -1 & \text{if } |\mu| < t \\ +1 & \text{if } |\mu| > t \end{cases}. \tag{3.38}$$

Note that the $k = \pi$ Fourier mode is not present when N is odd. We will extend these observations in section 3.5 and leave this merely as an observation at this stage.

3.2.1 Fermion Occupancies in the Ground State

It is of general interest to understand some basic aspects of the ground state. For instance, how the fermions are distributed in this state. Since the Kitaev chain with periodic boundary conditions is translational invariant, we expect the occupation number on some site to be independent of the site position – a flat fermion distribution. Keeping in mind that the ground state is annihilated by all the a_k operators, we find first the occupation of a given Fourier mode,

$$\begin{aligned}\langle n_k \rangle_\Omega &= \langle \Omega | \, c_k^\dagger c_k \, | \Omega \rangle \\ &= \langle \Omega | \, (u_k a_k^\dagger - v_k^* a_{-k})(u_k^* a_k - v_k a_{-k}^\dagger) \, | \Omega \rangle \\ &= |v_k|^2 \\ &= \frac{1}{2}\left(1 + \frac{t\cos k + \mu}{\sqrt{(t\cos k + \mu)^2 + \Delta^2 \sin^2 k}}\right).\end{aligned} \tag{3.39}$$

This expression is in agreement with the occupation of the modes $k = 0$ and $k = \pi$ as discussed in (3.20). Namely, $\langle n_{k=0} \rangle_\Omega = 1$ if $\mu > -t$ (and zero otherwise) and $\langle n_{k=\pi} \rangle_\Omega = 1$ if $\mu > t$ (and zero otherwise), which is also reflected in (3.36). The total fermion expectation number of the ground state is simply

$$\begin{aligned}\langle n_{\text{tot}} \rangle_\Omega &= \sum_{k \in \mathcal{B}} \langle n_k \rangle_\Omega \\ &= \frac{1}{2}\left(N + \sum_{k \in \mathcal{B}} \frac{t\cos k + \mu}{\sqrt{(t\cos k + \mu)^2 + \Delta^2 \sin^2 k}}\right).\end{aligned} \tag{3.40}$$

In the thermodynamic limit, the sum can to a good approximation be replaced by an integral. The increment in k was previously defined to be $\delta k = 2\pi/N$ as seen from equation (3.9). Hence,

$$\begin{aligned}\sum_{k \in \mathcal{B}} \frac{t\cos k + \mu}{\sqrt{(t\cos k + \mu)^2 + \Delta^2 \sin^2 k}} &= \frac{1}{\delta k} \sum_{k \in \mathcal{B}} \delta k \frac{t\cos k + \mu}{\sqrt{(t\cos k + \mu)^2 + \Delta^2 \sin^2 k}} \\ &\approx \frac{N}{2\pi} \int_0^{2\pi} \mathrm{d}k \frac{t\cos k + \mu}{\sqrt{(t\cos k + \mu)^2 + \Delta^2 \sin^2 k}},\end{aligned} \tag{3.41}$$

and in the special case of $\mu = 0$ this integral can be computed exactly since

$$\int_0^{2\pi} \mathrm{d}k \frac{t\cos k}{\sqrt{t^2\cos^2 k + \Delta^2 \sin^2 k}} = 0. \tag{3.42}$$

Thus, half of the available sites are filled for $\mu = 0$. The value $\langle n_k \rangle_\Omega$ may also be discussed in the limiting cases $\mu \ll -t$ and $\mu \gg t$. From (3.20) we see that $\langle n_k \rangle_\Omega$ tends to 1, and thereby $\langle n_{\text{tot}} \rangle_\Omega \to N$, as $\mu \gg t$. When $\mu \ll -t$ we see that $\langle n_k \rangle_\Omega$ tends to 0 and that $\langle n_{\text{tot}} \rangle_\Omega \to 0$. The occupation number of a single site in real space can be calculated by using the definition in equation (3.3),

$$\begin{aligned}
\langle n_x \rangle_\Omega &= \langle \Omega | \, c_x^\dagger c_x \, | \Omega \rangle \\
&= \langle \Omega | \left[\frac{1}{N} \sum_{k,k' \in \mathcal{B}} e^{-ix(k-k')} c_{k'}^\dagger c_k \right] | \Omega \rangle \\
&= \langle \Omega | \left[\frac{1}{N} \sum_{k,k' \in \mathcal{B} | k \neq k'} e^{-ix(k-k')} c_{k'}^\dagger c_k + \frac{1}{N} \sum_{k \in \mathcal{B}} c_k^\dagger c_k \right] | \Omega \rangle \\
&= \frac{1}{N} \sum_{k \in \mathcal{B}} \langle \Omega | \, c_k^\dagger c_k \, | \Omega \rangle \\
&= \frac{1}{N} \sum_{k \in \mathcal{B}} |v_k|^2 .
\end{aligned} \tag{3.43}$$

The sum with the $k \neq k'$ vanishes identically, as seen when expressing the c_k operators in terms of a_k operators. Hence, we are left with a flat distribution of occupation numbers in real space as anticipated. A simple relation between $\langle n_x \rangle_\Omega$ evaluated at $\pm\mu$ may be established. This is found by combining the relations (3.39), (3.41) and (3.43), still in the large N limit:

$$\begin{aligned}
&\langle n_x(\mu) \rangle_\Omega + \langle n_x(-\mu) \rangle_\Omega \\
&= \frac{1}{N} \sum_{k \in \mathcal{B}} \Big(|v_k(\mu)|^2 + |v_k(-\mu)|^2 \Big) \\
&= \frac{1}{N} \sum_{k \in \mathcal{B}} \left(1 + \frac{t \cos k + \mu}{2\sqrt{(t \cos k + \mu)^2 + \Delta^2 \sin^2 k}} + \frac{t \cos k - \mu}{2\sqrt{(t \cos k - \mu)^2 + \Delta^2 \sin^2 k}} \right) \\
&\approx 1 + \frac{1}{4\pi} \int_0^{2\pi} \mathrm{d}k \left(\frac{t \cos k + \mu}{\sqrt{(t \cos k + \mu)^2 + \Delta^2 \sin^2 k}} + \frac{t \cos k - \mu}{\sqrt{(t \cos k - \mu)^2 + \Delta^2 \sin^2 k}} \right) \\
&= 1 + \frac{1}{4\pi} \left(\int_0^{2\pi} \mathrm{d}k \, \frac{t \cos k + \mu}{\sqrt{(t \cos k + \mu)^2 + \Delta^2 \sin^2 k}} \right. \\
&\qquad \left. + \int_{-\pi}^{\pi} \mathrm{d}u \, \frac{-t \cos u - \mu}{\sqrt{(t \cos u + \mu)^2 + \Delta^2 \sin^2 u}} \right) \\
&= 1 + \frac{1}{4\pi} \left(\int_0^{2\pi} \mathrm{d}k \, f(k) - \int_{-\pi}^{\pi} \mathrm{d}u \, f(u) \right).
\end{aligned} \tag{3.44}$$

When splitting up the integrals above, a change of variables was made in the second integral, $u = k - \pi$. The function $f(k)$ refers to the integrand that appears in both final integrals. There is a simple theorem stating that if $f(x)$ is an integrable

periodic function of period a, then $\int_0^a \mathrm{d}x\, f(x) = \int_b^{a+b} \mathrm{d}x\, f(x)\ \forall\, b \in \mathbb{R}$. Since $f(k)$ is a periodic function, this theorem ensures that the two integrals above cancel. Therefore,

$$\langle n_x(\mu)\rangle_\Omega + \langle n_x(-\mu)\rangle_\Omega = 1, \tag{3.45}$$

meaning that the fermion occupation number of a general site on the chain is antisymmetric about $1/2$ when considered as a function of μ. Before closing these remarks we comment on a connection to statistical mechanics. Recall that $\langle n_k\rangle_\Omega = |v_k|^2$. Using the anticommutation relations (3.5) also reveals that $\langle n_k^2\rangle_\Omega = \langle n_k\rangle_\Omega$. This means that the variance of the Fourier mode occupation is

$$\sigma_{n_k}^2 = \langle n_k^2\rangle_\Omega - \langle n_k\rangle_\Omega^2 = \langle n_k\rangle_\Omega \left(1 - \langle n_k\rangle_\Omega\right). \tag{3.46}$$

It can be recognized as the variance of the *Bernoulli distribution*.[2] Moreover, it is identical to the particle number variance obtained with the Fermi-Dirac distribution in the *grand canonical ensemble* [16].[3] It is thus natural to interpret (3.46) as reflecting the underlying Fermi-Dirac statistics. Since the Kitaev chain is a mean field model, it would be meaningful to see that the average particle number fluctuations tend to zero in the thermodynamic limit. We found an expression for $\langle n_{\mathrm{tot}}\rangle_\Omega$ in equation (3.40). To discuss the variance of n_{tot}, an expression for $\langle n_{\mathrm{tot}}^2\rangle_\Omega$ is needed. This is a tedious calculation, and it does not add any insights to the computation from the previous paragraphs. We therefore state our result:

$$\langle n_{\mathrm{tot}}^2\rangle_\Omega = \sum_{k,l\in\mathcal{B}} \langle c_k^\dagger c_k c_l^\dagger c_l\rangle_\Omega = 2\sum_{k\in\mathcal{B}} |v_k u_k|^2 + \left(\sum_{k\in\mathcal{B}} |v_k|^2\right)^2. \tag{3.47}$$

In turn, the variance becomes

$$\sigma_{n_{\mathrm{tot}}}^2 = \langle n_{\mathrm{tot}}^2\rangle_\Omega - \langle n_{\mathrm{tot}}\rangle_\Omega^2 = 2\sum_{k\in\mathcal{B}} |v_k u_k|^2. \tag{3.48}$$

Both coherence factors $|u_k|^2$ and $|v_k|^2$ are typically of order unity (particularly never greater than 1). For instance, averaging $|v_k|^2$ over k was earlier seen to result in $1/2$ when $\mu = 0$. As a rough estimate, the variance therefore scales with N as $\sigma_{n_{\mathrm{tot}}}^2 \sim N$ since (3.48) instructs us to sum up N terms of order unity. Equivalently, $\sigma_{n_{\mathrm{tot}}} \sim \sqrt{N}$. According to equation (3.40) the expected number of fermions on the chain analogously scales with N as $\langle n_{\mathrm{tot}}\rangle_\Omega \sim N$. Therefore, the relative fluctuations of the total occupation number must scale with N as

$$\frac{\sigma_{n_{\mathrm{tot}}}}{\langle n_{\mathrm{tot}}\rangle_\Omega} \sim \frac{1}{\sqrt{N}}. \tag{3.49}$$

[2]The Bernoulli distribution is the Binomial distribution, $P_m(\langle n_k\rangle_\Omega) = \langle n_k\rangle_\Omega^m + (1-\langle n_k\rangle_\Omega)^{1-m}$, with one trial.

[3]The fermionic grand canonical single-particle partition function is $\mathcal{Z} = 1 + e^{-(\epsilon-\mu)/(kT)}$ for an excitation of energy ϵ at temperature T.

This corresponds to the particle number fluctuations in the grand canonical ensemble [16]. And in fact, finding the BCS ground state was historically treated as a variational problem in this ensemble [2, 3].

3.2.2 Quasiparticle Excitations

The focus is turned to excitations of the ground state. Since the diagonal Hamiltonian (3.26) suggests that the fundamental excitations of the system are quasiparticles, we are interested in finding the quasiparticle occupation number distribution in real space. We define

$$|\varphi_x\rangle = \phi_x^\dagger |\Omega\rangle \quad \text{with} \quad \phi_x \equiv \frac{1}{\sqrt{N}} \sum_{k\in\mathcal{B}} e^{-ikx} a_k. \tag{3.50}$$

The state $|\varphi_x\rangle$ is interpreted as a quasiparticle with localization around position x. An occupation operator is introduced,

$$\rho(x) \equiv c_x^\dagger c_x, \tag{3.51}$$

such that for instance $\langle n_x\rangle_\Omega = \langle\Omega|\,\rho(x)\,|\Omega\rangle$. In this nomenclature the charge expectation value is $\langle Q\rangle_\Omega = \sum_{x=1}^N \langle\Omega|\,q\,\rho(x)\,|\Omega\rangle = Nq\langle n_x\rangle_\Omega$ if all fermions have charge q. We are interested in calculating $\langle\varphi_{x_0}|\,\rho(x)\,|\varphi_{x_0}\rangle$ – the fermion occupation of site x with a qasiparticle state located at x_0. Since the ground state gives rise to flat distribution of occupation numbers, this new function is expected to introduce a perturbation in this background distribution. The perturbation is expected to depend only on the relative distance $x - x_0$,

$$\langle\varphi_{x_0}|\,\rho(x)\,|\varphi_{x_0}\rangle \equiv \langle n_x\rangle_\Omega + S(x - x_0). \tag{3.52}$$

First, observe that

$$\begin{aligned}\langle\varphi_{x_0}|\,\rho(x)\,|\varphi_{x_0}\rangle &= \langle\Omega|\,\phi_{x_0}\rho(x)\phi_{x_0}^\dagger\,|\Omega\rangle \\ &= \frac{1}{N}\sum_{k,l\in\mathcal{B}} e^{-ix_0(k-l)}\,\langle\Omega|\,a_k c_x^\dagger c_x a_l^\dagger\,|\Omega\rangle\,.\end{aligned} \tag{3.53}$$

The quasiparticle operators should be anticommuted to the opposite sides in the expression $\langle\Omega|\,a_k c_x^\dagger c_x a_l^\dagger\,|\Omega\rangle$ to annihilate the ground state. Since the quasiparticle operators are linear combinations of the c_k operators, the non-vanishing anticommutation relations between c_k and c_x are needed in this procedure. Using (3.2) and (3.5) we find the only non-vanishing relation,

$$\{c_x^\dagger, c_k\} = \frac{e^{ikx}}{\sqrt{N}}. \tag{3.54}$$

This yields, by using that $a_k = u_k c_k + v_k c_{-k}^\dagger$, the anticommutation relations we need,

$$\{c_x^\dagger, a_k\} = \frac{e^{ikx}}{\sqrt{N}} u_k \quad \text{and} \quad \{c_x, a_k\} = \frac{e^{ikx}}{\sqrt{N}} v_k. \tag{3.55}$$

Using the above relations repeatedly gives

$$\begin{aligned}
\langle\Omega|\, a_k c_x^\dagger c_x a_l^\dagger \,|\Omega\rangle &= \langle\Omega|\left(\frac{e^{ikx}}{\sqrt{N}} u_k - c_x^\dagger a_k\right)\left(\frac{e^{-ilx}}{\sqrt{N}} u_l^* - a_l^\dagger c_x\right)|\Omega\rangle \\
&= \frac{u_k u_l^*}{N} e^{ix(k-l)} + \langle\Omega|\, c_x^\dagger a_k a_l^\dagger c_x \,|\Omega\rangle \\
&= \frac{u_k u_l^*}{N} e^{ix(k-l)} + \delta_{k,l}\,\langle\Omega|\,\rho(x)\,|\Omega\rangle - \langle\Omega|\, c_x^\dagger a_l^\dagger a_k c_x \,|\Omega\rangle \\
&= \frac{u_k u_l^*}{N} e^{ix(k-l)} + \delta_{k,l}\langle n_x\rangle_\Omega \\
&\qquad\qquad - \langle\Omega|\left(\frac{e^{-ilx}}{\sqrt{N}} v_l^* - a_l^\dagger c_x^\dagger\right)\left(\frac{e^{ikx}}{\sqrt{N}} v_k - c_x a_k\right)|\Omega\rangle \\
&= \frac{u_k u_l^*}{N} e^{ix(k-l)} + \delta_{k,l}\langle n_x\rangle_\Omega - \frac{v_k v_l^*}{N} e^{ix(k-l)}.
\end{aligned} \tag{3.56}$$

This may be inserted back into (3.53) to obtain

$$\begin{aligned}
\langle\varphi_{x_0}|\,\rho(x)\,|\varphi_{x_0}\rangle &= \frac{1}{N}\sum_{k,l\in\mathcal{B}} e^{-ix_0(k-l)}\,\langle\Omega|\, a_k c_x^\dagger c_x a_l^\dagger \,|\Omega\rangle \\
&= \frac{1}{N}\sum_{k,l\in\mathcal{B}} e^{-ix_0(k-l)}\left[\frac{e^{ix(k-l)}}{N}(u_k u_l^* - v_k v_l^*) + \delta_{k,l}\langle n_x\rangle_\Omega\right] \\
&= \langle n_x\rangle_\Omega + \frac{1}{N^2}\sum_{k,l\in\mathcal{B}} e^{i(x-x_0)(k-l)}(u_k u_l^* - v_k v_l^*).
\end{aligned} \tag{3.57}$$

Assume now that v_k has no complex phase factor depending on k. The coefficient u_k is already assumed to be real. Thus, we realize that

$$w_{k,l} \equiv u_k u_l^* - v_k v_l^* \tag{3.58}$$

is symmetric in k and l, $w_{k,l} = w_{l,k}$, and real, $w_{k,l} \in \mathbb{R}$. Therefore, the sum in (3.57) can be expressed as Fourier-like sum of an even function,

$$\begin{aligned}
\langle\varphi_{x_0}|\,\rho(x)\,|\varphi_{x_0}\rangle = \langle n_x\rangle_\Omega &+ \frac{2}{N^2}\sum_{k,l\in\mathcal{B}|l<k} w_{k,l}\cos\Big((x-x_0)(k-l)\Big) \\
&+ \frac{1}{N}\Big(1 - 2\langle n_x\rangle_\Omega\Big).
\end{aligned} \tag{3.59}$$

This is on the same form as the ansatz in (3.52). Note that the last term in (3.59) stems from the sum over the diagonal elements, $w_{k,k}$, and it is suppressed in the large

N limit. The expression for the perturbation, $S(x - x_0)$, is not very transparent other than having a dependency on $x - x_0$. It can not be easily evaluated since the coefficients $w_{k,l}$ depend intricately on the parameters μ, t and Δ. A numerical study of the function $S(x - x_0)$ can be seen in Figure 3.2 where the function is plotted for a range of chemical potentials. The distribution reveals a well-defined localization of the quasiparticle excitation with a slight overlap to the neighbouring sites of x_0.

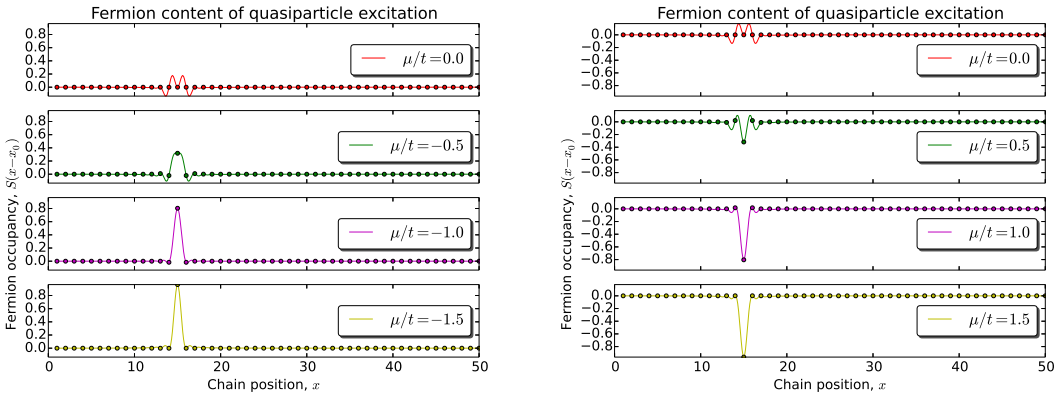

(a) **(b)**

Figure 3.2: Fermion occupancy in quasiparticle excitation, $S(x - x_0)$, with $x_0 = 15$ for $N = 50$ sites. The parameters were fixed to $\Delta = 0.5$ and $t = 1.0$. **(a)** $\mu \leq 0$ and **(b)** $\mu \geq 0$. Note that the two top panels with red graphs are identical. Coloured disks indicate the integer positions along the chain. The excitation $S(x - x_0)$ is sharply peaked around x_0. The peak is positive for $\mu \ll -t$ as the quasiparticle excitation is mainly particle. Similarly, the peak is negative peak for $\mu \gg t$ as the quasiparticle excitation is mainly hole.

Finally, we shift the focus to fermion excitations of the ground state,

$$|\psi_x\rangle = c_x^\dagger |\Omega\rangle = \frac{1}{\sqrt{N}} \sum_{k\in\mathcal{B}} e^{ikx} u_k a_k^\dagger |\Omega\rangle \,, \tag{3.60}$$

when expressed in terms of quasiparticle operators. Calculating $\langle\psi_{x_0}| \rho(x) |\psi_{x_0}\rangle$ is very similar to the derivation of $\langle\varphi_{x_0}| \rho(x) |\varphi_{x_0}\rangle$. We therefore skip the intermediate steps and state our result,

$$\begin{aligned}\langle\psi_{x_0}| \rho(x) |\psi_{x_0}\rangle = \langle n_x\rangle_\Omega (1 - \langle n_x\rangle_\Omega) + \frac{2}{N^2} \sum_{k,l\in\mathcal{B}|l<k} h_{k,l} \cos\Big((x - x_0)(k - l)\Big) \\ + \frac{1}{N}\left(1 - \langle n_x\rangle_\Omega - \left(\sigma_{n_{\text{tot}}}/\sqrt{N}\right)^2\right),\end{aligned} \tag{3.61}$$

with

$$h_{k,l} \equiv u_k^* u_l (u_k u_l^* - v_k v_l^*). \tag{3.62}$$

Again, the final constant term comes from summing over the diagonal elements $h_{k,k}$. The function (3.61) is qualitatively similar to (3.59) for $\mu < 0$. However, as $\mu \gg t$ the whole distribution in (3.61) tends to 0. This is not strange; it simply means that one hopelessly tries to excite the ground state with a fermion when all sites are already occupied (recall that $\langle n_x \rangle_\Omega \to 1$ as $\mu \gg t$).

3.3 Topological Invariant and the Berry Phase

We approach the task of establishing the topological invariant by computing a certain *geometrical phase* (the reader is referred to Appendix A for details and a formal derivation). The topological phase transition has a physical consequence in an open system. There, the invariant will turn out to indicate whether the system supports boundary Majorana fermions or not [10]. Our point of departure is to decompose the BdG Hamiltonian, $\mathcal{H}_k$, in a Pauli matrix basis. This is inspired by the prescription outlined by Jason Alicea [11]. It has a geometrical appeal and makes a natural connection to the geometrical phase. We will deviate from Alicea's minimalistic explanation and perform a calculation with associations of the original derivation by Michael Berry [25]. The Hamiltonian as expressed in the momentum representation,

$$H = \frac{1}{2} \sum_{k \in \mathcal{B}} \boldsymbol{C}_k^\dagger \mathcal{H}_k \boldsymbol{C}_k, \tag{3.63}$$

is a sum over paired states in the Brillouin zone. The matrix $\mathcal{H}_k$ connects particles and holes of momenta k and $-k$. Focusing on a single pair, Berry phase effects are expected to occur if k is allowed to adiabatically sweep $\mathcal{B}$ [26]. We will consider such a sweep and apply the formalism derived in Appendix A and B. With $\boldsymbol{\sigma} = \begin{pmatrix} \sigma_x, & \sigma_y, & \sigma_z \end{pmatrix}^T$ denoting the Pauli matrix vector, we decompose

$$\mathcal{H}_k = \boldsymbol{h}(k) \cdot \boldsymbol{\sigma} = \begin{pmatrix} h_z & h_x - ih_y \\ h_x + ih_y & -h_z \end{pmatrix}. \tag{3.64}$$

Comparing with the matrix components from equation (3.13) the vector $\boldsymbol{h}(k)$ can be directly read out,

$$\boldsymbol{h}(k) = \begin{pmatrix} \Delta \sin\phi \sin k \\ -\Delta \cos\phi \sin k \\ -t \cos k - \mu \end{pmatrix}, \tag{3.65}$$

with ϕ the superconducting phase as before. We think of ϕ, Δ and μ as fixed parameters, and k as varying in the interval $\mathcal{B} = (0, 2\pi]$ for convenience in this section. Crucially, the vector $\boldsymbol{h}(k)$ in equation (3.65) is restricted to lie in the plane spanned by the three points $(0,0,0)$, $(\sin\phi, -\cos\phi, 0)$ and $(0,0,1)$. Moreover, its components explicitly suggest that the curve in this plane is an ellipse. It is phrased parametrically in k with center in $(0,0,-\mu)$, one axis in the xy-plane of length Δ and the other axis along the z-axis of length t. For simplicity, we fix $\phi = 0$ such that $\boldsymbol{h}(k)$

lies in the yz-plane. This is depicted in Figure 3.3. Note, for later reference, that the direction of circulation is reversed if $\Delta < 0$. We will return to this observation when considering the open Kitaev chain with a spatially varying order parameter. The decomposition in equation (3.64) is just a rotated Pauli matrix. We may generally parametrize it by its polar angles, (φ, ϑ),

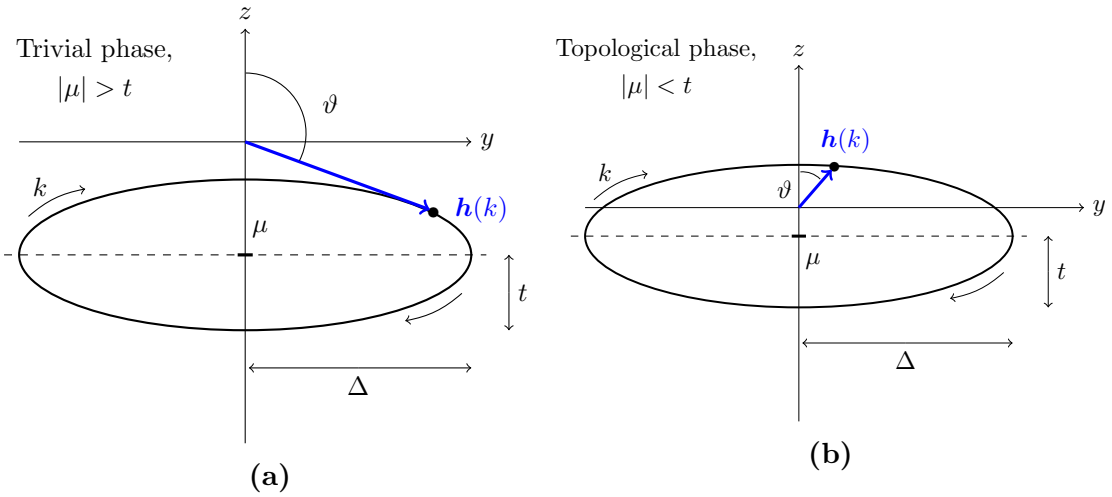

Figure 3.3: A geometrical interpretation of the topological invariant. Here, it is assumed that $\phi = 0$ and $\Delta > 0$. The contour traced out by $\boldsymbol{h}(k)$ is denoted by Γ. **(a)** If $|\mu| > t$ the origin is not inside in the contour traced out by $\boldsymbol{h}(k)$. **(b)** The vector $\boldsymbol{h}(k)$ circulates the origin if and only if $|\mu| < t$.

$$\mathcal{H}_k = \boldsymbol{h}(k) \cdot \boldsymbol{\sigma} = \sigma_{\boldsymbol{h}}(\varphi, \vartheta). \tag{3.66}$$

The eigenvectors take the usual form for a rotated Pauli matrix (see for instance [23]),

$$|\boldsymbol{h}, +\rangle = \begin{pmatrix} \cos\frac{\vartheta}{2} \\ e^{i\varphi}\sin\frac{\vartheta}{2} \end{pmatrix} \quad \text{and} \quad |\boldsymbol{h}, -\rangle = \begin{pmatrix} -e^{i\varphi}\sin\frac{\vartheta}{2} \\ \cos\frac{\vartheta}{2} \end{pmatrix}, \tag{3.67}$$

corresponding to the eigenvalues $\pm|\boldsymbol{h}|$ respectively.

3.3.1 Calculating the Geometrical Phase

As follows from the Adiabatic Theorem (the reader is directed to Appendix B for a formulation of the theorem), the geometric phases, $\alpha_\pm$, accumulated by the two states $|\boldsymbol{h}, \pm\rangle$ are given by the contour integral (summation over i implied)

$$\alpha_\pm = \oint_\Gamma \mathrm{d}h^i \, a_{i,\pm}(\boldsymbol{h}), \tag{3.68}$$

with Γ referring to the closed elliptical contour shown in Figure 3.3 and $\boldsymbol{a}_\pm(\boldsymbol{h})$ the vector field derived in Appendix A. It has the components

$$a_{i,\pm}(\boldsymbol{h}) = -i \langle \boldsymbol{h}, \pm | \frac{\partial}{\partial h^i} | \boldsymbol{h}, \pm \rangle \,. \tag{3.69}$$

The differential change in the ith component of $\boldsymbol{h}$, $\mathrm{d}h^i$, is caused by k running through the Brillouin zone. Using *Stokes' Theorem* enables us to rewrite the integral in a way that will reveal important features,

$$\alpha_\pm = \oint_\Gamma \mathrm{d}\boldsymbol{h} \cdot \boldsymbol{a}_\pm(\boldsymbol{h}) = \int_{\mathcal{S}} \mathrm{d}\boldsymbol{S} \cdot \Big(\nabla_{\boldsymbol{h}} \times \boldsymbol{a}_\pm(\boldsymbol{h}) \Big), \tag{3.70}$$

with $\mathcal{S}$ referring to the area of a surface with Γ as boundary, $\times$ is the antisymmetric vector product and

$$\nabla_{\boldsymbol{h}} \equiv \left(\tfrac{\partial}{\partial h^1}, \quad \tfrac{\partial}{\partial h^2}, \quad \tfrac{\partial}{\partial h^3} \right)^T \equiv \left(\partial_1, \quad \partial_2, \quad \partial_3 \right)^T . \tag{3.71}$$

The vector field appearing in the surface integral,

$$\boldsymbol{f}_\pm(\boldsymbol{h}) = \nabla_{\boldsymbol{h}} \times \boldsymbol{a}_\pm(\boldsymbol{h}), \tag{3.72}$$

is closely related to the antisymmetric tensor field f_{ij} that is derived in Appendix A.2. Making use of the Levi-Cevita symbol ϵ_{ijk}, the components of $\boldsymbol{f}_\pm(\boldsymbol{h})$ are related to $f_{jk,\pm}$ by

$$\begin{aligned} f_{i,\pm}(\boldsymbol{h}) &= \epsilon_{ijk} \partial_j a_{k,\pm} \\ &= \frac{1}{2} \epsilon_{ijk} \left(\partial_j a_{k,\pm} - \partial_k a_{j,\pm} \right) \\ &= \frac{1}{2} \epsilon_{ijk} f_{jk,\pm}(\boldsymbol{h}). \end{aligned} \tag{3.73}$$

Hence, the expression derived in Appendix A for calculating the components f_{ij} translates to a prescription for finding $f_{i,\pm}$,

$$f_{i,n}(\boldsymbol{h}) = -\frac{i}{2} \epsilon_{ijl} \sum_{n' \neq n} \left[\frac{\langle n | \partial_j \mathcal{H}_k | n' \rangle \langle n' | \partial_l \mathcal{H}_k | n \rangle}{(E_n - E_{n'})^2} - (j \leftrightarrow l) \right], \tag{3.74}$$

with $|n\rangle \in \{ |\boldsymbol{h}, +\rangle, |\boldsymbol{h}, -\rangle \}$ and $(j \leftrightarrow l)$ referring to the previous expression with indices j and l interchanged. Equivalently,

$$\boldsymbol{f}_\pm(\boldsymbol{h}) = -i \frac{\langle \boldsymbol{h}, \pm | \boldsymbol{\sigma} | \boldsymbol{h}, \mp \rangle \times \langle \boldsymbol{h}, \mp | \boldsymbol{\sigma} | \boldsymbol{h}, \pm \rangle}{(E_\pm - E_\mp)^2}, \tag{3.75}$$

since $\nabla_{\boldsymbol{h}} \mathcal{H}_k = \boldsymbol{\sigma}$ as seen from equation (3.66). We apply the same trick as originally performed by Michael Berry [26]; we temporarily rotate the axes such that $\vartheta = 0$, i.e. $\boldsymbol{h} = |\boldsymbol{h}| \boldsymbol{e}_z$. This means that

$$|\boldsymbol{h},+\rangle = \begin{pmatrix}1\\0\end{pmatrix} \equiv |+\rangle \quad \text{and} \quad |\boldsymbol{h},-\rangle = \begin{pmatrix}0\\1\end{pmatrix} \equiv |-\rangle\,. \tag{3.76}$$

Using Pauli matrices gives the quantities needed to evaluate (3.75),

$$\begin{aligned} &\langle +|\,\sigma_x\,|-\rangle = 1, \quad \langle +|\,\sigma_y\,|-\rangle = -i, \quad \langle +|\,\sigma_z\,|-\rangle = 0 \quad \Rightarrow \\ &\qquad \langle +|\,\boldsymbol{\sigma}\,|-\rangle \times \langle -|\,\boldsymbol{\sigma}\,|+\rangle = 2i\boldsymbol{e}_z. \end{aligned} \tag{3.77}$$

We arrive at a result that is general for a two-level system,

$$\begin{aligned} \boldsymbol{f}_\pm(\boldsymbol{h}) &= -i\frac{\langle \pm|\boldsymbol{\sigma}|\mp\rangle \times \langle \mp|\boldsymbol{\sigma}|\pm\rangle}{(E_\pm - E_\mp)^2} \\ &= -i\frac{\pm 2i\boldsymbol{e}_z}{4|\boldsymbol{h}|^2} \\ &= \pm\frac{\boldsymbol{h}}{2|\boldsymbol{h}|^3}. \end{aligned} \tag{3.78}$$

The field $\boldsymbol{f}_\pm$ is thus similar to a monopole source of charge $1/2$ at the origin, $\boldsymbol{h} = \boldsymbol{0}$, which is exactly where the energy levels become degenerate. The phase from equation (3.70) may be interpreted as the flux from this monopole field through a surface $\mathcal{S}$ that has Γ as boundary. This is simply equal to half the solid angle, denoted by Ω_Γ, that the surface $\mathcal{S}$ covers. With our elliptical contour, it boils down to whether the origin is inside the ellipse or not (see again Figure 3.3). If the origin is inside the contour the solid angle is equivalent to that of half a sphere, namely $\Omega_\Gamma = 2\pi$. If the origin is outside Γ the solid angle is trivial, $\Omega_\Gamma = 0$. To summarize,

$$\alpha_\pm = \int_{\mathcal{S}} \mathrm{d}\boldsymbol{S}\cdot\boldsymbol{f}_\pm(\boldsymbol{h}) = \pm\frac{\Omega_\Gamma}{2} = \begin{cases} \pm\pi & \text{if } |\mu| < t \\ 0 & \text{if } |\mu| > t \end{cases}. \tag{3.79}$$

Hence, the phase factors, $\nu = e^{-i\alpha_\pm}$, are restricted to being a $\mathbb{Z}_2$ integer. The possibilities are

- $|\mu| < t$: The origin lies inside the contour Γ, and the ground state of $\mathcal{H}_k$ will obtain a geometrical phase factor equal to $\nu = e^{-i\alpha_-} = -1$ during an adiabatic sweep of k.
- $|\mu| > t$: The origin is outside the contour Γ, and the ground state does not obtain any non-trivial phase factor during the adiabatic evolution, $\nu = 1$.

Thus, the quantization of ν is a consequence of k sweeping the entire Brillouin zone adiabatically and focusing on the Berry phase obtained by a single Cooper pair. The two values of ν reflect the two topologically distinct paths of $\boldsymbol{h}(k)$ (see again Figure 3.3). It is perhaps more convenient to depict the difference in terms of the unit vector $\boldsymbol{h}(k)/|\boldsymbol{h}(k)|$ as Alicea does [11]. In the case of $|\mu| < t$, this unit vector must trace out a unit circle as k sweeps $(0, 2\pi]$. Whereas for $|\mu| > t$, the normalized

vector trace out only a part of the circle arc. As seen from Figure 3.3, this arc contains the south pole if $\mu > t$ and the north pole if $\mu < -t$.

The two types of trajectories, characterized by ν, classify the topological phases of the model. Although not evident at the moment, the phase $|\mu| < t$ is denoted by the *topological phase*. It will turn out to be the parameter regime that supports edge Majorana modes in the open system. In contrast, $|\mu| > t$ is called the *trivial phase*. Furthermore, it is no coincidence that the transitions, $|\mu| = t$, occur exactly at the gap closing points (see Figure 3.1) where the ground state in (3.36) undergoes discrete changes in its fermionic content.

3.4 Two-Point Correlation Functions

The tools needed to calculate various correlation functions have been established throughout the past sections. Given two observables, A and B, we define the two-point correlation function as

$$C(A, B) \equiv \langle AB \rangle - \langle A \rangle \langle B \rangle. \tag{3.80}$$

Mathematically, this quantity is the *covariance* of A and B. The following deduction is separated in two types of fermionic correlations, which we denote by C_1 and C_2 respectively. We emphasise that this study is not based on any reference, but some of the findings will turn out to be related to the discussion in [24]. The section is concluded with a discussion of the results.

3.4.1 First Type of Correlation

We study the correlation describing annihilation of a fermion at site y when excited at x. Both $\langle c_x^\dagger \rangle_\Omega = \langle c_y \rangle_\Omega = 0$, which is seen by expressing the c_x operators in terms of quasiparticle operators as before. Hence, we find that

$$\begin{aligned} C_1(x, y) &\equiv \langle c_x^\dagger c_y \rangle_\Omega - \langle c_x^\dagger \rangle_\Omega \langle c_y \rangle_\Omega \\ &= \frac{1}{N} \langle \Omega | \sum_{k \in \mathcal{B}} e^{ikx} (u_k a_k^\dagger - v_k^* a_{-k}) \sum_{l \in \mathcal{B}} e^{-ily} (u_l^* a_l - v_l a_{-l}^\dagger) | \Omega \rangle \\ &= \frac{1}{N} \sum_{k \in \mathcal{B}} e^{ik(x-y)} |v_k|^2 \\ &= \frac{1}{2N} \sum_{k \in \mathcal{B}} \left(1 - \frac{\epsilon_k}{E_k} \right) \cos\Big(k(x-y) \Big). \end{aligned} \tag{3.81}$$

This function is real valued, $C_1(x, y) : \mathbb{N}^2 \to \mathbb{R}$, and it will be investigated numerically. Intuitively, we expect the function to have a peak, centred at $x = y$, with the value of the background distribution exactly at that point according to equation

(3.43). The function $C_1(x, y = 15)$ is shown in Figure 3.4 for a representative range of μ values and $N = 50$ chain sites. More interesting, however, is the long range behaviour; is a fermion annihilation at one site affected by an excitation on a site far away for arbitrary N?

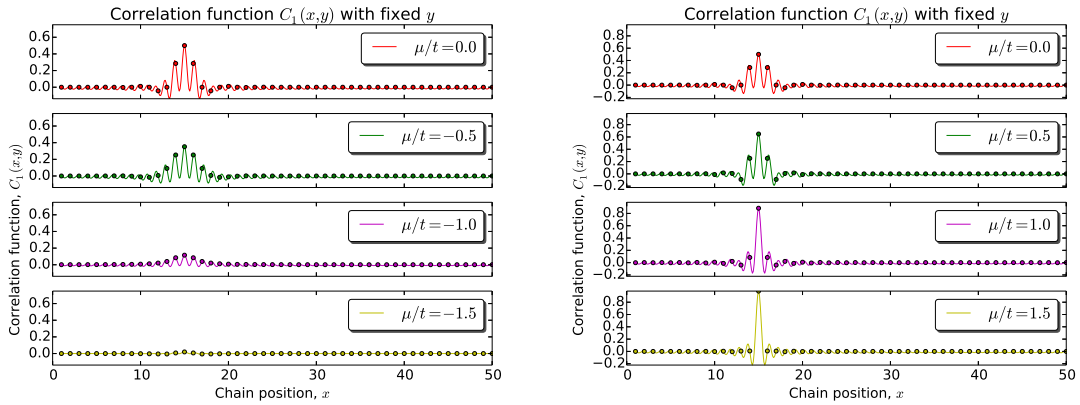

(a) **(b)**

Figure 3.4: Correlation function $C_1(x, y)$ for fixed $y = 15$, $t = 1.0$, $\Delta = 0.5$ with $N = 50$ sites. The coloured disks indicate the integer positions along the chain. **(a)** $\mu \leq 0$ and **(b)** $\mu \geq 0$. Note that the two top panels with red graphs are identical and kept for visual reference when comparing panels within the same figure.

In order to address this question one may trace the values of $C_1(x, y)$ for large spatial separation, $|x - y| = N/2 - 1$ (for even N), as a function of μ. The reason for choosing $|x-y| = N/2-1$ is that the correlations generally seemed to be suppressed exactly at $|x-y| = N/2$ (for even N). Stepping one site away was thus beneficial for the purpose of visualizing non-vanishing correlations with large spatial separation. We have shown this in Figure 3.5 for several system sizes. One can see how the long range values are discontinuous at the critical points, $\mu = \pm t$. Numerically, it was seen that rapid oscillations occurred for $|\mu| < t$ when $\Delta \ll t$. Indications of this behaviour can be seen for $N = 20$ in Figure 3.5.

Observe next that $C_1(x, y)$ can be related to the inverse Fourier transform of a certain expectation value. Glancing back at the deduction in equation (3.39), we find the connection

$$\frac{1}{N} \sum_{k \in \mathcal{B}} e^{-ikx} \langle c_k^\dagger c_k \rangle_\Omega = C_1(0, x), \tag{3.82}$$

which is a spatial translation of $C_1(x, y)$. Hence, $C_1(x, y)$ is basically the inverse Fourier transform of the fermion Fourier mode occupation number $\langle c_k^\dagger c_k \rangle_\Omega$.

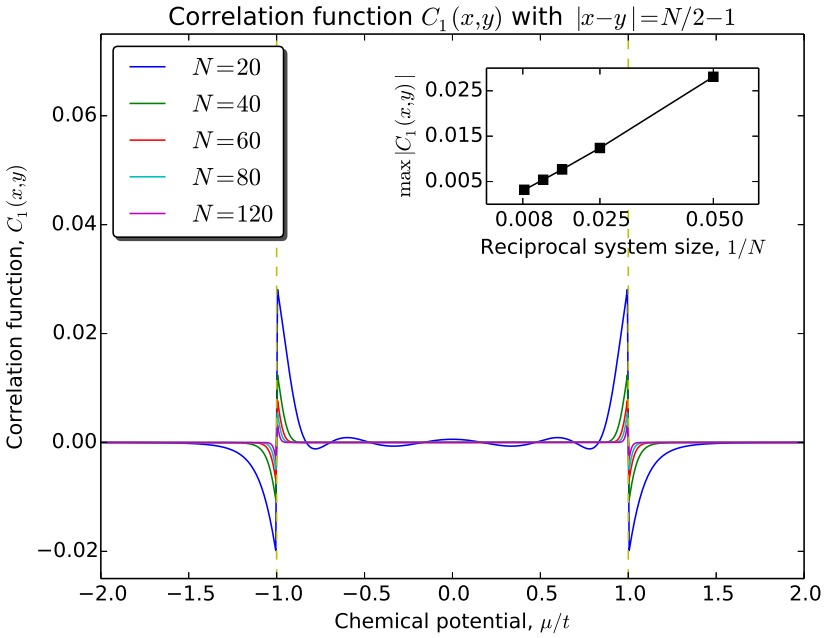

Figure 3.5: Correlation function $C_1(x, y)$ with $|x - y| = N/2 - 1$ as function of μ for several system sizes. The remaining parameters were fixed, $\Delta = 0.5$ and $t = 1.0$. The phase transitions at $\mu = \pm t$ are indicated with a yellow dashed line. The inset plot shows the maximum value of $|C_1(x, y)|$ as function of reciprocal system size.

3.4.2 Second Type of Correlation

The Kitaev Hamiltonian is a mean field model with Cooper pairing; terms of the type $\langle c_x^\dagger c_y^\dagger \rangle_\Omega$ are generally expected to be non-zero. Recall that such terms would not be present in a normal metal. With the assumption of $\phi = 0$ we define and calculate a second type of correlation function,

$$\begin{aligned} C_2(x,y) &\equiv \langle c_x^\dagger c_y^\dagger \rangle_\Omega - \langle c_x^\dagger \rangle_\Omega \langle c_y^\dagger \rangle_\Omega \\ &= \frac{1}{N} \langle \Omega | \sum_{k \in \mathcal{B}} e^{ikx} (u_k a_k^\dagger - v_k^* a_{-k}) \sum_{l \in \mathcal{B}} e^{ily} (u_l a_l^\dagger - v_l^* a_{-l}) \, | \Omega \rangle \\ &= -\frac{1}{N} \sum_{k \in \mathcal{B}} e^{ik(x-y)} v_k^* u_k \\ &= -\frac{\Delta}{N} \sum_{k \in \mathcal{B}} \frac{\sin k}{2E_k} \sin\Big(k(x-y)\Big). \end{aligned} \tag{3.83}$$

Just like $C_1(x, y)$, the function $C_2(x, y)$ is real valued (when $\phi = 0$). Furthermore, it is not unexpectedly proportional to the superconducting gap Δ. In Figure 3.6 the function $C_2(x, y = 15)$ is shown for a sample of μ values and $N = 50$ chain sites. Analogous to our study of C_1 Figure 3.7 visualizes the function $C_2(x, y)$ with large spatial separation, $|x - y| = N/2 - 1$, as function of μ. It does not reveal any discontinuity, but it exhibits qualitatively some of the same features as $C_1(x, y)$.

This function may also be related to the inverse Fourier transform of an expectation value. We find that

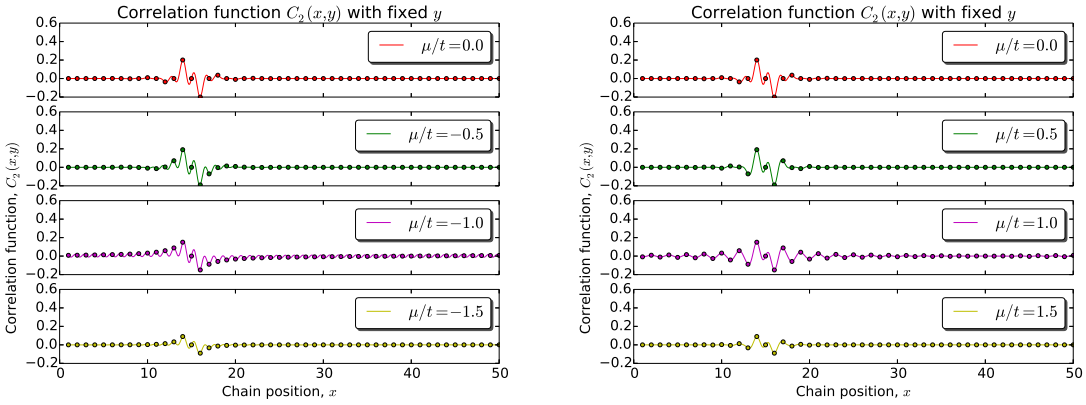

Figure 3.6: Correlation function $C_2(x, y)$ for fixed $y = 15$, $t = 1.0$, $\Delta = 0.5$ with $N = 50$ sites. The coloured disks indicate the integer positions along the chain. **(a)** $\mu \leq 0$ and **(b)** $\mu \geq 0$. Note that the two top panels with red graphs are identical and kept for visual reference when comparing panels within the same figure.

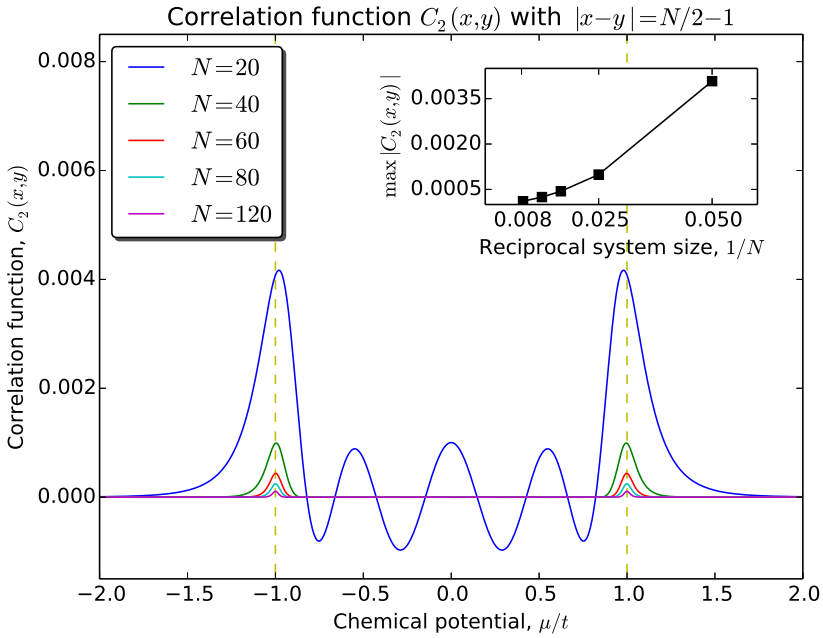

Figure 3.7: Correlation function $C_2(x, y)$ with $|x - y| = N/2 - 1$ as function of μ for several system sizes. The remaining parameters were fixed, $\Delta = 0.5$ and $t = 1.0$. The phase transitions at $\mu = \pm t$ are marked with a yellow dashed line. The inset plot shows the maximum value of $|C_2(x, y)|$ as function of reciprocal system size.

$$\begin{aligned}\frac{1}{N}\sum_{k\in\mathcal{B}} e^{-ikx}\langle c_k^\dagger c_{-k}^\dagger\rangle_\Omega &= \frac{1}{N}\sum_{k\in\mathcal{B}} e^{-ikx}\left\langle\Omega\right|(u_k a_k^\dagger - v_k^* a_{-k})(u_k a_{-k}^\dagger + v_k^* a_k)\left|\Omega\right\rangle \\ &= -\frac{1}{N}\sum_{k\in\mathcal{B}} e^{-ikx} v_k^* u_k \\ &= C_2(0,x).\end{aligned} \tag{3.84}$$

As pointed out by Read and Green [24] – although their discussion concerns a two-dimensional system – this latter function may be interpreted vaguely as the *Cooper pair size*, motivated by the fact that Cooper pairs are bound states of fermions with momenta k and $-k$.

3.4.3 Discussion and Remarks

Usually, one applies the term *long range correlations* if the correlation function depends algebraically on $|x-y|$, in contrast to an exponential dependency. The function $C_1(x,y)$ is generally not in any of these categories as Figure 3.4 and equation (3.81) indicate. However, one might suggest to do a more rigorous analysis in an attempt to determine if there is a qualitative difference between the correlations in the topological and the trivial phase. One approach to classifying the difference could be to parametrize the correlations by some trial function, having both an exponential and an algebraic decay, and statistically determine which part is dominant [16]. This quickly becomes a tedious investigation without revealing any revolutionary insights. Judging from Figure 3.4, the function $C_1(x,y)$ is only seen to have values that are not highly suppressed whenever $|x-y| \ll N/2$.

The inset plot in Figure 3.5 reveals that the maximum correlation values of C_1 with large spatial separation scale approximately inversely with system size, $\sim 1/N$. Recall that we consider a discrete chain with only nearest neighbour couplings. Thus, it is not unexpected that an increment in the number of sites leads to such a decay in the correlations. The correlations with great spatial separation will, by naive extrapolation, disappear in the thermodynamic limit, $N \to \infty$. The fact that the correlations are enlarged at $\mu = \pm t$ can be understood qualitatively from the closing of the energy gap at these points. When the gap is close to zero, a close-to-zero-energy excitation of the ground state could perturb almost undisturbed throughout the system.

One might question the discontinuity seen at $\mu = \pm t$ seen in Figure 3.5. Why does it occur? In the previous section we discussed that the unit vector $\boldsymbol{h}(k)/|\boldsymbol{h}(k)|$ traced out a circle when $|\mu| < t$. Whereas for $|\mu| > t$, the vector spanned only a part of the circle arc. The transition between these trajectories stem from discontinuities of u_k and v_k, meaning the eigenvectors of $\mathcal{H}_k$. The key properties in (3.20) do indeed confirm this, in particular for $k = 0$ and $k = \pi$. It is therefore not unexpected that a function depending heavily on $|v_k|^2$, as C_1 indeed does, reflects this discontinuity.

Moreover, this observation seems to be in accordance with a part of the discussion of Read and Green [24]. They argue how the topological phase transition is rooted in the topology of k-space and that this, in turn, should be reflected in the mean field functions u_k, v_k, E_k and Δ_k. We therefore vaguely interpret the observed discontinuity in the correlation function as reflecting the distinction between the trivial and the topological phase of the model.

Figures 3.6 and 3.7 show some of the characteristics just discussed. The scaling in the inset of Figure 3.7, approximately a $\sim 1/N$ relation,[4] suggests once more that the correlations with large spatial separation become suppressed in the thermodynamic limit. Some resonance or enlargement of the correlations occur close to $\mu = \pm t$. At this point we adopt the interpretation of Read and Green that $C_2(0, x)$ may be thought of as the Cooper pair size [24]. In this sense, we may state, by looking at Figure 3.7, that the Cooper pairs are more loosely bound close to the phase transitions where the energy gap is small.

Finally, one could *a priori* ask if it is of interest to investigate quasiparticle correlations, such as $\langle \varphi_x^\dagger \varphi_y \rangle_\Omega$, $\langle \varphi_x^\dagger \varphi_y^\dagger \rangle_\Omega$, $\langle \varphi_x \varphi_y \rangle_\Omega$ and $\langle \varphi_x \varphi_y^\dagger \rangle_\Omega$. By inspecting the definition of these operators in equation (3.50), and by applying the defining property of the ground state (3.28), however, it is clear that only one of these functions is non-zero, namely $\langle \varphi_x \varphi_y^\dagger \rangle_\Omega$. It is trivially seen to be $\langle \varphi_x \varphi_y^\dagger \rangle_\Omega = \delta_{x,y}$. This is no surprise since the fundamental excitations of the system are non-interacting particles.

3.5 Comparing Periodic and Anti-Periodic Boundary Conditions

We close this chapter with an observational note on anti-periodic boundary conditions for completeness and later reference. Recall the discrete Fourier transform that was introduced in the beginning of this chapter,

$$c_x = \frac{1}{\sqrt{N}} \sum_{k=1}^{N} e^{-ikx\frac{2\pi}{N}} c_k. \tag{3.85}$$

Requiring *periodic* boundary conditions can then be expressed by demanding that

$$c_{x=1} = c_{x=N+1} \Rightarrow e^{ikN} = 1, \tag{3.86}$$

which results in $k = 2\pi m/N$ for $m \in \{1, 2, \ldots, N\}$ as already seen. A superconducting flux quantum threading the closed Kitaev chain could be encoded by altering

[4] One may notice that the $N = 20$ line in Figure 3.7 deviates slightly from the linear scaling tendency in the inset plot. The exact reason for this is unclear. Generally, however, this deviation tended to be even larger as the system size was reduced further. Thus, some small system effect plausibly disturbs the linear tendency.

the boundary conditions to *anti-periodic* [24]. We may also think of this merely as a mathematical modification of the boundary conditions. It means that we instead require

$$c_{x=1} = -c_{x=N+1} \Rightarrow e^{ikN} = -1. \tag{3.87}$$

The values of k satisfying this belongs to the set

$$\bar{\mathcal{B}} \equiv \Big\{ \frac{\pi}{N}(2n+1) \mid n \in \{1, 2, \ldots, N\} \Big\}. \tag{3.88}$$

It should be compared to (3.9), and it is seen that

$$\begin{aligned} &k = 0 \notin \bar{\mathcal{B}} \text{ and } k = \pi \notin \bar{\mathcal{B}} \text{ of } N \text{ is even,} \\ &k = 0 \notin \bar{\mathcal{B}} \text{ and } k = \pi \in \bar{\mathcal{B}} \text{ of } N \text{ is odd.} \end{aligned} \tag{3.89}$$

The differences between occupied modes for periodic and anti-periodic boundary conditions are illustrated in Figure 3.8 in the topological phase, $|\mu| < t$. Note that the fermion parity of the ground state when $|\mu| < t$, for both even and odd N, is -1 with periodic boundary conditions and $+1$ for anti-periodic boundary conditions. A more complete collection of observations, based on the modes present or absent in $\mathcal{B}$ and $\bar{\mathcal{B}}$, are summarized in Table 3.1. The resulting ground states are seen to be in accordance with the two-dimensional analogue of the Kitaev chain that Read and Green thoroughly analyse [24]. One difference from their discussion, though, is the dispersion reflected in ϵ_k. The quadratic dispersion that is used in their discussion gives rise to a different characterization of the topological phases, determined only by the sign of μ.

Table 3.1: Comparison of ground state fermion parity for periodic and anti-periodic boundary conditions in the closed Kitaev chain.

Boundary conditions and number of sites, N	Ground state parity, $\mu < -t$	Ground state parity, $\lvert\mu\rvert < t$	Ground state parity, $\mu > t$
Periodic, even N	$+1$	-1	$+1$
Periodic, odd N	$+1$	-1	-1
Anti-periodic, even N	$+1$	$+1$	$+1$
Anti-periodic, odd N	$+1$	$+1$	-1

Another observation seems to be apparent in both our results and those of Read and Green. Comparing the ground state parity for periodic and anti-periodic boundary conditions (for even and odd N separately) reveals that they are opposite in the topological phase and equal in the trivial phase.

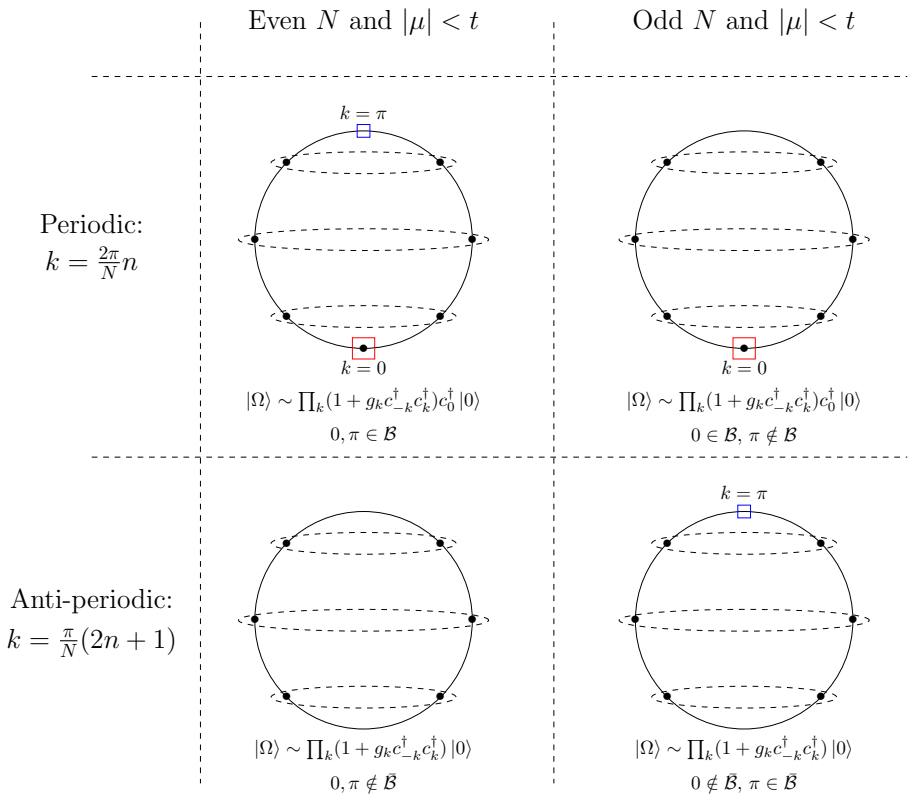

Figure 3.8: Illustration of (partly) occupied Fourier modes in the ground state for even/odd N and for periodic/anti-periodic boundary conditions in the topological phase, $|\mu| < t$. Paired states (Cooper pairs) are marked with dashed ellipses, and unpaired states are highlighted with red boxes. The blue boxes indicate present but unoccupied modes. The products are understood to run over $\mathcal{B}^+$ and a corresponding set $\bar{\mathcal{B}}^+$ for periodic and anti-periodic boundary conditions respectively.

3.5.1 Closing Remarks

In this chapter we have progressively built a detailed understanding of the closed Kitaev chain. Discrete Fourier transforms allowed us to analytically diagonalize the Hamiltonian and to find its energy spectrum. We derived a ground state with Cooper-paired states and two unoccupied modes that depended on the parameter regime. This detailed view adds information to the schematic description of the ground state in [11]. Effort was spent in describing the fermion distribution in the ground state and excitations of it. The fermion occupancy was seen to be antisymmetric when consider as a function of μ, and it did not depend on the chain site (translational invariance). Then, a Berry phase calculation was found to distinguish the two parameter regimes $|\mu| < t$ and $|\mu| > t$, reflecting two types of curves traced out by $\boldsymbol{h}(k)$. With this characterization in mind we sought how the topological phase transition manifested itself in two-point correlation functions. In particular, correlation resonances and Cooper pairs of enlarged spatial extension were observed at the transitions. Finally, we compared the ground state fermion parity for periodic and anti-periodic boundary conditions, which depended on the presences or absence of the unpaired operators $c_0^\dagger$ and $c_\pi^\dagger$.

Chapter 4

The Open Kitaev Chain

So far, we have examined analytical expressions to understand various aspects of the closed Kitaev chain. As the boundary conditions are changed to open, one expects the interior of the chain – assuming the system is large – to have the same intrinsic properties as the closed one. Still, some qualitatively new phenomena may appear due to the open boundary. The main feature is the possible appearance of Majorana zero modes on the two ends [10]. Exploiting edge Majoranas in networks of one-dimensional wires has been proposed as a protocol of probing particles with exotic exchange statistics [7]. The Hamiltonian of the open Kitaev chain is

$$H = -\mu \sum_{x=1}^{N} c_x^\dagger c_x - \frac{1}{2} \sum_{x=1}^{N-1} \Big(t c_x^\dagger c_{x+1} + \Delta e^{i\phi} c_x c_{x+1} + \text{h.c.} \Big). \tag{4.1}$$

We open this chapter with a revisit of Kitaev's argument, demonstrating localized Majorana modes for a special choice of parameters. Thereafter, we depart from Kitaev's discussion and establish a more complete understanding of the degenerate ground states in terms of normal fermion occupancy states. We suggest and prove an induction hypothesis concerning the form of these ground states. Then, we relate these states to the unique one in the closed chain. Finally, we diagonalize the open Kitaev Hamiltonian numerically. Instead of focusing on domain walls in chemical potential, which is usually discussed in the literature [11, 12], we study the effect of a spatially varying order parameter $\Delta = \Delta_x$. Especially, we are interested in seeing the effect of an order parameter mimicking the profile of a vortex, even though this construction may be artificial in one dimension.

4.1 Introductory Demonstration of Edge Majoranas

The idea of Kitaev [10] is revisited to demonstrate that the Hamiltonian (4.1) supports a non-local fermionic operator formed by Majoranas. The fact that the fermion is a Dirac-particle and physically distinct from its antiparticle (reflected in $c_x \neq c_x^\dagger$) can be used to decompose the fermion operators in Majorana operators that lack

this degree of freedom. For convenience, we merge the dependency of the superconducting phase into the definition,

$$c_x \equiv \frac{1}{2} e^{-i\frac{\phi}{2}} (\gamma_{B,x} + i\gamma_{A,x}), \tag{4.2}$$

with

$$\gamma_{\alpha,x} = \gamma_{\alpha,x}^\dagger \quad \text{and} \quad \{\gamma_{\alpha,x}, \gamma_{\alpha',x'}\} = 2\delta_{\alpha,\alpha'}\delta_{x,x'}. \tag{4.3}$$

The fermion operators are in other words split into a real (B) and an imaginary (A) part dictated by the subscript $\alpha \in \{A, B\}$. There are in total $2N$ distinct γ operators. Assume next that $\mu = 0$ and $\Delta = t$. When (4.2) is inserted into the Hamiltonian in (4.1), one finds after simplification that

$$\begin{aligned} H &= -\frac{t}{2} \sum_{x=1}^{N-1} (c_x^\dagger c_{x+1} + e^{i\phi} c_x c_{x+1} + \text{h.c.}) \\ &= i\frac{t}{2} \sum_{x=1}^{N-1} \gamma_{A,x+1}\gamma_{B,x}. \end{aligned} \tag{4.4}$$

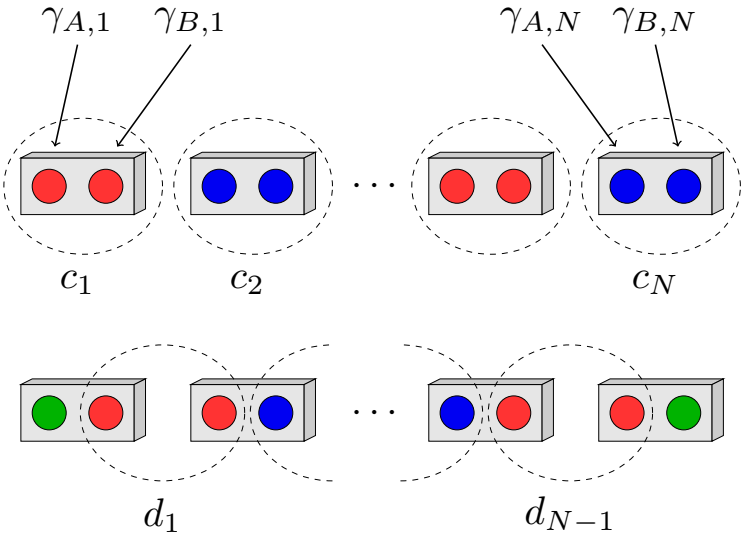

Figure 4.1: Top chain: fermionic operators c_x are split up into two Majorana operators. Bottom chain: pairing up Majorana operators from neighbouring c_x operators leaves a non-local operator formed by each end of the chain. The figure is inspired by [5].

By pairing up Majorana operators from neighbouring fermion sites, schematically depicted in Figure 4.1, H is diagonalized. We define new operators,

$$d_x \equiv \frac{1}{2}(\gamma_{A,x+1} + i\gamma_{B,x}). \tag{4.5}$$

They satisfy fermionic anticommutation relations,

$$\{d_x, d_{x'}^\dagger\} = \delta_{x,x'} \quad \text{and} \quad \{d_x, d_{x'}\} = \{d_x^\dagger, d_{x'}^\dagger\} = 0, \tag{4.6}$$

allowing us to interpret them as fermionic degrees of freedom.[1] This simplifies (4.4) to

$$H = t \sum_{x=1}^{N-1} \left(d_x^\dagger d_x - \frac{1}{2} \right). \tag{4.7}$$

This diagonal Hamiltonian supports $N-1$ states with constant energy spacing, t, formed by the $d_x^\dagger$ operators. Two Majorana operators, however, are missing in this Hamiltonian, namely $\gamma_{A,1}$ and $\gamma_{B,N}$. Thus, we define one non-local fermion operator,

$$d_0 \equiv \frac{1}{2}(\gamma_{A,1} + i\gamma_{B,N}). \tag{4.8}$$

This operator destroys an excitation of zero energy since it is absent in the Hamiltonian. Therefore, the ground state must be doubly degenerate. This is in contrast to the closed Kitaev chain where the ground state was unique. Furthermore, the Hamiltonian (4.7) should be compared to the trivial case $t = \Delta = 0$, in which it takes the form

$$H = -\mu \sum_{x=1}^{N} c_x^\dagger c_x. \tag{4.9}$$

The two Hamiltonians (4.7) and (4.9) represent the two distinct phases of the open Kitaev chain for the simplest choice of parameters. The latter Hamiltonian has a unique ground state, while the primer has unpaired Majorana operators on the open ends and degenerate ground states of opposite fermionic parity [10].

4.2 The Ground State Subspace

We take an analytical detour in an attempt obtain a more complete understanding of the degenerate ground states for the simple choice of parameters $\mu = 0$ and $\Delta = t$. It is of interest to find the many-body ground states expressed in terms of product states with well-defined fermion occupancies. There are a total of 2^N of these states, representing all possible combinations of occupation numbers. This is, of course, also the dimension of the Hilbert space of the system. Furthermore, how are the degenerate ground state of the open system related to the unique ground state, $|\Omega\rangle$, in the closed system? This is a question we will try to answer in this section. First, some notation must be introduced. The many-body vacuum with N

[1] In fact, one can pair up A- and B-types of Majorana operators from arbitrary sites to form new fermionic operators.

sites, denoted by $|0_N\rangle$ for clarity in this section, is defined to be the product state of zero fermion occupancy states in the position representation,

$$|0_N\rangle \equiv \bigotimes_{x=1}^{N} |0, x\rangle \equiv |00\ldots0\rangle\,. \tag{4.10}$$

This state is destroyed by any c_x operator. We define a state with some filled sites to have the order of *increasing* indices on fermion creation operators. For instance, the fully filled state, $|11\cdots1\rangle$, is defined as

$$|11\ldots1\rangle \equiv c_1^\dagger c_2^\dagger \cdots c_N^\dagger\,|0_N\rangle\,. \tag{4.11}$$

Acting with a fermion operator on some general state may therefore result in picking up a sign, depending on the fermion parity of the preceding part of the state. For instance,

$$c_j\,|\alpha_1\alpha_2\cdots\alpha_{j-1}\;1\;\alpha_{j+1}\cdots\alpha_N\rangle = (-1)^{\sum_{i=1}^{j-1}\alpha_i}\,|\alpha_1\alpha_2\cdots\alpha_{j-1}\;0\;\alpha_{j+1}\cdots\alpha_N\rangle\,, \tag{4.12}$$

with $\alpha_i \in \{0,1\}$. We know that the ground state subspace is two-dimensional since the fermionic operator $d_0^\dagger$ creates an excitation of zero energy. Two orthogonal states spanning the ground state, $\{|g_1\rangle\,, |g_2\rangle\}$, are therefore defined to satisfy

$$d_0\,|g_1\rangle = d_0^\dagger\,|g_2\rangle = 0. \tag{4.13}$$

The states are related by

$$d_0^\dagger\,|g_1\rangle = |g_2\rangle\,. \tag{4.14}$$

We start by constructing a ground state candidate, $|a\rangle$, naively by applying all d_x for $x \in \{1,\ldots,N-1\}$ on the vacuum state,

$$|a\rangle \equiv \prod_{x=1}^{N-1} d_x\,|0_N\rangle\,. \tag{4.15}$$

Normalization is taken care of later. The state $|a\rangle$ has by construction zero energy.[2] An immediate question should be raised. The ground state subspace is two-dimensional, and we have a set of three possible states at our disposal,

$$\mathcal{G} \equiv \Big\{\,|a\rangle\,, d_0\,|a\rangle\,, d_0^\dagger\,|a\rangle\,\Big\}. \tag{4.16}$$

[2]Again, the constant energy term in (4.7) is understood to be neglected. Therefore, the Hamiltonian with $t = \Delta$ and $\mu = 0$ is simply $H = t\sum_{x=1}^{N-1} d_x^\dagger d_x$.

By some means, one of the states in $\mathcal{G}$ must be eliminated as candidates for $|g_1\rangle$ and $|g_2\rangle$. In order to determine which, the state $|a\rangle$ should be calculated explicitly. We will do this by observing a pattern occurring with just a few sites, propose a hypothesis, and prove it by induction on the system size, N. The starting point is to express the d operators in terms of ordinary fermion operators. Using equations (4.2), (4.5) and (4.8) we find, assuming that $\phi = 0$,

$$d_x = \frac{i}{2}\left(c_x + c_x^\dagger - c_{x+1} + c_{x+1}^\dagger\right) \quad \text{and} \quad d_0 = \frac{i}{2}\left(c_N + c_N^\dagger - c_1 + c_1^\dagger\right). \tag{4.17}$$

To see the structure of $|a\rangle$ we look at the emerging pattern with $N \in \{2, 3, 4\}$. Applying d operators successively yields

$$d_1 |0_2\rangle = \frac{i}{2}\Big[\, |10\rangle + |01\rangle \,\Big], \tag{4.18}$$

$$d_2 d_1 |0_3\rangle = \left(\frac{i}{2}\right)^2 \Big[\, |000\rangle - |101\rangle - |110\rangle - |011\rangle \,\Big], \tag{4.19}$$

$$\begin{aligned} d_3 d_2 d_1 |0_4\rangle = \left(\frac{i}{2}\right)^3 \Big[\, & |0\rangle \otimes \Big(|10\rangle + |01\rangle \Big) \otimes |0\rangle - |1\rangle \otimes \Big(|10\rangle + |01\rangle \Big) \otimes |1\rangle \\ & + |1\rangle \otimes \Big(|00\rangle - |11\rangle \Big) \otimes |0\rangle + |0\rangle \otimes \Big(|00\rangle - |11\rangle \Big) \otimes |1\rangle \,\Big]. \end{aligned} \tag{4.20}$$

In (4.20) the states belonging to the end points are explicitly extracted to reveal a pattern. It motivates our induction hypothesis, denoted by I_N, on the general form of $|a\rangle$,

$$I_N: \quad |a\rangle \equiv \prod_{x=1}^{N-1} d_x |0_N\rangle = \left(\frac{i}{2}\right)^{N-1} \Big[\, |0\, b\, 0\rangle - |1\, b\, 1\rangle + |0\, c\, 1\rangle + |1\, c\, 0\rangle \,\Big]. \tag{4.21}$$

Above, $|b\rangle$ contains all 2^{N-3} combinations of odd (even) fermion parity states if N is even (odd). All the states in $|b\rangle$ have the same relative weights of either $+1$ or -1. Similarly, $|c\rangle$ contains all 2^{N-3} combinations of even (odd) fermion parity states if N is even (odd). The relative weights of the states in $|c\rangle$ are also either $+1$ or -1. We proceed by proving that $I_N \Rightarrow I_{N+1}$ when the number of sites is increased by one in the chain. This is, by induction, enough to prove that I_N holds for all N.

Proof. Assume first that N is odd. Thus, I_N tells us that $|a\rangle$ takes the form in (4.21) with $|b\rangle$ being an even parity state and $|c\rangle$ as an odd parity state. We must show that $|a'\rangle \equiv d_N |a\rangle \otimes |0\rangle$ is in accordance with the description imposed by I_{N+1}. In other words, $|a'\rangle$ must have $|b'\rangle$ as an odd parity state and $|c'\rangle$ as an even parity state since $N + 1$ is even. We find that

$$
\begin{aligned}
|a'\rangle &\equiv d_N\,|a\rangle \otimes |0\rangle \\
&= \left(\frac{i}{2}\right)^N \Big[\, |0\rangle \otimes \Big(\, |b\,1\rangle - |c\,0\rangle \,\Big) \otimes |0\rangle - |1\rangle \otimes \Big(\, |b\,1\rangle - |c\,0\rangle \,\Big) \otimes |1\rangle \\
&\qquad\qquad + |1\rangle \otimes \Big(\, |b\,0\rangle + |c\,1\rangle \,\Big) \otimes |0\rangle + |0\rangle \otimes \Big(\, |b\,0\rangle + |c\,1\rangle \,\Big) \otimes |1\rangle \,\Big] \\
&= \left(\frac{i}{2}\right)^N \Big[\, |0\,b'\,0\rangle - |1\,b'\,1\rangle + |0\,c'\,1\rangle + |1\,c'\,0\rangle \,\Big],
\end{aligned}
\tag{4.22}
$$

with

$$
|b'\rangle \equiv |b\,1\rangle - |c\,0\rangle \quad \text{and} \quad |c'\rangle \equiv |b\,0\rangle + |c\,1\rangle\,. \tag{4.23}
$$

Hence, $|b'\rangle$ is an odd parity state that contains all 2^{N-2} combinations, which follows from the induction hypothesis. In addition, $|c'\rangle$ must be an even parity state containing all 2^{N-2} combinations. This is exactly the properties required by I_{N+1}. In principle, we must also show that the same implication holds with N even. However, this is not necessary since the only change would be an overall sign in the above calculation, stemming from equation (4.12). We conclude that $I_N \Rightarrow I_{N+1}$ and I_N is true for all N. □

The basic properties of the state $|a\rangle$ are now established by equation (4.21). At this point it is convenient to split the discussion into even and odd N.

4.2.1 Odd N Ground States

According to (4.21), the state $|b\rangle$ contains combinations of even parity states with relative weights of either $+1$ or -1. Analogously, $|c\rangle$ contains combinations of odd parity states. Using once more the rule in equation (4.12) we find that

$$
d_0^\dagger\,|a\rangle = 0. \tag{4.24}
$$

In other words, the state $d_0^\dagger\,|a\rangle$ is trivial and should be excluded from $\mathcal{G}$. Calculating $d_0\,|a\rangle$ and normalizing the resulting states gives the proper ground states, $|g_1\rangle$ and $|g_2\rangle$, and corresponding fermion parities:

$$
\begin{aligned}
d_0\,|a\rangle \mapsto |g_1\rangle &= \frac{1}{\sqrt{2^{N-1}}}\Big[\, -|0\,c\,0\rangle + |1\,c\,1\rangle + |0\,b\,1\rangle + |1\,b\,0\rangle \,\Big] \quad \text{with} \quad P=-1, \\
|a\rangle \mapsto |g_2\rangle &= \frac{1}{\sqrt{2^{N-1}}}\Big[\, |0\,b\,0\rangle - |1\,b\,1\rangle + |0\,c\,1\rangle + |1\,c\,0\rangle \,\Big] \quad \text{with} \quad P=+1.
\end{aligned}
\tag{4.25}
$$

Notice how all the 2^N available combinations of parity states are involved in either $|g_1\rangle$ or $|g_2\rangle$.

4.2.2 Even N Ground States

Still, $|a\rangle$ is as described in (4.21), and it has $|b\rangle$ containing combinations of odd parity states and $|c\rangle$ containing combinations of even parity states. Again, by using the rule in equation (4.12) we find that

$$d_0 |a\rangle = 0. \tag{4.26}$$

Hence, the state $d_0 |a\rangle$ should now be excluded from $\mathcal{G}$. Normalizing $|a\rangle$ and $d_0^\dagger |a\rangle$ results in the ground states, which this time are denoted by $|\tilde{g}_1\rangle$ and $|\tilde{g}_2\rangle$ to distinguish them from the odd N ground states,

$$\begin{aligned} |a\rangle \mapsto |\tilde{g}_1\rangle &= \frac{1}{\sqrt{2^{N-1}}}\Big[\, |0\, b\, 0\rangle - |1\, b\, 1\rangle + |0\, c\, 1\rangle + |1\, c\, 0\rangle \,\Big] \quad \text{with} \quad P = -1, \\ d_0^\dagger |a\rangle \mapsto |\tilde{g}_2\rangle &= \frac{1}{\sqrt{2^{N-1}}}\Big[\, |0\, c\, 0\rangle - |1\, c\, 1\rangle - |0\, b\, 1\rangle - |1\, b\, 0\rangle \,\Big] \quad \text{with} \quad P = +1. \end{aligned} \tag{4.27}$$

4.2.3 Relation to the Closed Chain

The deduction above was restricted to the special case of $\Delta = t$ and $\mu = 0$. We have just seen that the degenerate ground states involve all fermion occupancy states with weights of equal magnitude. The basic parity properties found above are in satisfactory accordance with Kitaev's discussion [10]. However, our results give a more detailed picture of the ground state subspace structure that is not transparent *a priori*. Furthermore, we have seen that choosing the correct states from the set of candidates in $\mathcal{G}$ depends non-trivially on whether the number of sites are even or odd. A natural follow-up question is to ask what the relation between the degenerate ground states of the open chain and the unique ground state in the closed chain is. Recall from Figure 3.8 that the state $|\Omega\rangle$ in the periodic chain had $P = -1$ when $|\mu| < t$.

Imagine connecting the two ends of the open chain by adding the term $\lambda i \frac{t}{2} \gamma_{A,1} \gamma_{B,N}$ in equation (4.4) and gradually increasing λ from 0 to 1. Since the state $|g_1\rangle$ ($|\tilde{g}_1\rangle$) is of odd parity when N is odd (even), it should correspond to the unique ground state $|\Omega\rangle$ for odd (even) N. Recall further the defining property of the ground state in the periodic chain: it should be annihilated by any quasiparticle annihilation operator. This is in perfect agreement with the deduction above since both $|g_1\rangle$ and $|\tilde{g}_1\rangle$ are annihilated by d_0 (and by construction all the other d_x operators), $d_0 |\tilde{g}_1\rangle = d_0 |g_1\rangle = 0$.

Moreover, the state $|\Omega\rangle$ was of even fermion parity with anti-periodic boundary conditions. In this case, $|g_2\rangle$ ($|\tilde{g}_2\rangle$) would be the correct candidates for $|\Omega\rangle$ for odd (even) N. However, both $|g_2\rangle$ and $|\tilde{g}_2\rangle$ are annihilated by $d_0^\dagger$ and not d_0. Formally, this is equivalent to introducing the term $\lambda i \frac{t}{2} \gamma_{A,1} \gamma_{B,N}$ in the Hamiltonian but let λ change from 0 to -1 instead. Anti-periodic boundary conditions may therefore

be interpreted as a negative hopping between the ends of the open chain. To close the focus on the degenerate ground states, we calculate the entanglement entropy between the ends and the interior of the chain.

4.2.4 Entanglement Entropy

We seek further insight of the ground states with $\Delta = t$ and $\mu = 0$ by the dividing the system into two parts. Let $\mathcal{E}$ (edge) be the subsystem consisting of the end points, $x = 1$ and $x = N$, and $\mathcal{I}$ (internal) the internal part of the system, $x \in \{2, \ldots, N-1\}$. To keep our discussion concrete, we stick to odd N and make use of (4.25). However, our results can be checked to remain equally valid for both ground states with even N. We want to quantitatively establish the *entanglement entropy* of the composite system $\mathcal{I}+\mathcal{E}$ when being in one of the states $|g_1\rangle$ or $|g_2\rangle$. Generally, if the system is in some state $|\psi\rangle$, the *density operator* of the full system is defined to be

$$\rho \equiv |\psi\rangle \langle\psi| \,. \tag{4.28}$$

The density operator of the subsystem $\mathcal{E}$ is found by tracing over the states from $\mathcal{I}$ in ρ,

$$\rho_{\mathcal{E}} = \mathrm{Tr}_{\mathcal{I}} (\rho) = \sum_{i \in \mathcal{I}} \langle i|\rho|i\rangle \,. \tag{4.29}$$

The *von Neumann entropy* of $\rho_{\mathcal{E}}$ is then taken as a quantitative measure of the entanglement entropy of the composite system [23],

$$S_{\mathcal{E}} = -\mathrm{Tr}(\rho_{\mathcal{E}} \log \rho_{\mathcal{E}}) = -\sum_{k} \lambda_k^{(\mathcal{E})} \log \lambda_k^{(\mathcal{E})}, \tag{4.30}$$

with $\lambda_k^{(\mathcal{E})}$ the kth eigenvalue of $\rho_{\mathcal{E}}$. This framework is applied to $|\psi\rangle = |g_1\rangle$ and $\rho = |g_1\rangle \langle g_1|$. To trace out the internal system one may split up the sum in odd and even parity states in $\mathcal{I}$,

$$\begin{aligned} \rho_{\mathcal{E}} &= \sum_{i \in \mathcal{I}} \langle i|\rho|i\rangle \\ &= \sum_{\substack{i \in \mathcal{I} \\ i:\, P=-1}} \langle i|\rho|i\rangle + \sum_{\substack{j \in \mathcal{I} \\ j:\, P=+1}} \langle j|\rho|j\rangle \,. \end{aligned} \tag{4.31}$$

The reason for this is that $\langle i|\rho|i\rangle$ only contributes for terms containing $|c\rangle \langle c|$. Furthermore, we know from earlier that $|c\rangle$ contains 2^{N-3} states of odd parity with weights equal to ± 1. Therefore, $\langle i|c\rangle \langle c|i\rangle = 1$ in the odd parity trace. Similarly, the sum over even parity states picks out contributions with $|b\rangle \langle b|$ in ρ. Hence,

$$\sum_{\substack{i\in\mathcal{I}\\ i:\, P=-1}} \langle i|c\rangle\langle c|i\rangle = \sum_{\substack{j\in\mathcal{I}\\ j:\, P=+1}} \langle j|b\rangle\langle b|j\rangle = 2^{N-3}. \tag{4.32}$$

This means that the reduced density matrix $\rho_{\mathcal{E}}$ is

$$\begin{aligned}\rho_{\mathcal{E}} &= \sum_{\substack{i\in\mathcal{I}\\ i:\, P=-1}} \langle i|g_1\rangle\langle g_1|i\rangle + \sum_{\substack{j\in\mathcal{I}\\ j:\, P=+1}} \langle j|g_1\rangle\langle g_1|j\rangle \\ &= \frac{1}{4}\Big(|01\rangle\langle 01| + |10\rangle\langle 10| + |01\rangle\langle 10| + |10\rangle\langle 01| \\ &\qquad + |00\rangle\langle 00| + |11\rangle\langle 11| - |00\rangle\langle 11| - |11\rangle\langle 00|\Big) \\ &= \frac{1}{4}\begin{pmatrix} 1 & 0 & 0 & -1 \\ 0 & 1 & 1 & 0 \\ 0 & 1 & 1 & 0 \\ -1 & 0 & 0 & 1 \end{pmatrix},\end{aligned} \tag{4.33}$$

with the vector representation of states in the order $|00\rangle$, $|01\rangle$, $|10\rangle$, $|11\rangle$. This matrix has two eigenvalues, 0 and 1/2, both doubly degenerate. We are thereby left with the following value of the entanglement entropy:

$$S_{\mathcal{E}} = -\sum_k \lambda_k^{(\mathcal{E})} \log \lambda_k^{(\mathcal{E})} = \log 2. \tag{4.34}$$

One arrives at exactly the same reduced density matrix when $|\psi\rangle = |g_2\rangle$, and for both even N ground states as well. Since the dimension of $\mathcal{E}$ is $\dim(\mathcal{E}) = 4$, the value $S_{\mathcal{E}}$ is exactly 1/2 of its maximum. Intuitively, this is caused by the structure of $\rho_{\mathcal{E}}$ in (4.33), which respects fermion parity in the sense that only states of equal parity are connected. To summarize, we may say that the degenerate ground states are delicately *polarized in a fermion parity sense*; they are equally weighted combinations of all pure states of either even or odd parity. Furthermore, there is a significant entanglement between the edge and the internal part of the system in the ground states. These aspects of the physical state space are valuable to keep in mind, and they do not seem to be discussed in the literature.

4.3 Matrix Formulation of the Open Kitaev Chain

Recall the Kitaev Hamiltonian in (4.1),

$$H = -\mu\sum_{x=1}^{N} c_x^\dagger c_x - \frac{1}{2}\sum_{x=1}^{N-1}(tc_x^\dagger c_{x+1} + \Delta e^{i\phi} c_x c_{x+1} + \text{h.c.}). \tag{4.35}$$

The task of finding the energy spectrum and eigenstates for a general parameter choice can be formulated in terms of a matrix eigenvalue problem. The goal of this

section is to establish this formulation. We split up terms using the anticommutation relations in equation (3.2) to get a fully symmetrized version of the Hamiltonian. Including all available combinations of operators leaves us with

$$\begin{aligned} H = &-\frac{1}{2}\mu\sum_{x=1}^{N}\left(c_x^\dagger c_x - c_x c_x^\dagger\right) - \frac{1}{4}\sum_{x=1}^{N-1}\Big(t(c_x^\dagger c_{x+1} - c_{x+1}c_x^\dagger) \\ &+ \Delta e^{i\phi}\left(c_x c_{x+1} - c_{x+1}c_x\right) + \text{h.c.}\Big) + \text{const.} \end{aligned} \tag{4.36}$$

A column vector of fermion operators is introduced,

$$\mathbf{\Psi} \equiv \left(c_1,\ \ c_1^\dagger,\ \ c_2,\ \ c_2^\dagger,\ \ \ldots,\ \ c_N,\ \ c_N^\dagger\right)^T. \tag{4.37}$$

The Hamiltonian can now be compactly written on a *quadratic form*,

$$H = \mathbf{\Psi}^\dagger \mathcal{M} \mathbf{\Psi}. \tag{4.38}$$

Above, the matrix $\mathcal{M}$ is $2N \times 2N$, hermitian, *pentadiagonal* and found by comparing elements with equation (4.36),

$$\mathcal{M} = \frac{1}{2}\begin{pmatrix} -\mu & 0 & -\frac{t}{2} & \frac{\Delta}{2}e^{-i\phi} & 0 & \ldots & 0 & 0 & 0 \\ 0 & \mu & -\frac{\Delta}{2}e^{i\phi} & \frac{t}{2} & 0 & \ldots & 0 & 0 & 0 \\ -\frac{t}{2} & -\frac{\Delta}{2}e^{-i\phi} & -\mu & 0 & -\frac{t}{2} & \ldots & 0 & 0 & 0 \\ \frac{\Delta}{2}e^{i\phi} & \frac{t}{2} & 0 & \mu & -\frac{\Delta}{2}e^{i\phi} & \ddots & 0 & 0 & 0 \\ 0 & 0 & -\frac{t}{2} & -\frac{\Delta}{2}e^{-i\phi} & -\mu & \ddots & 0 & 0 & 0 \\ \vdots & \vdots & \vdots & \ddots & \ddots & \ddots & \ddots & \ddots & \vdots \\ 0 & 0 & 0 & 0 & 0 & \ddots & \mu & -\frac{\Delta}{2}e^{i\phi} & \frac{t}{2} \\ 0 & 0 & 0 & 0 & 0 & \ddots & -\frac{\Delta}{2}e^{-i\phi} & -\mu & 0 \\ 0 & 0 & 0 & 0 & 0 & \ldots & \frac{t}{2} & 0 & \mu \end{pmatrix}. \tag{4.39}$$

Suppose that a matrix Q diagonalizes H such that

$$H = \mathbf{\Psi}^\dagger Q^\dagger D Q \mathbf{\Psi}, \tag{4.40}$$

with $D = \text{diag}(E_1, \ldots, E_{2N})$ containing the energy eigenvalues. Due to the particle-hole symmetry, the energy spectrum is expected to be symmetric. We can force it to be symmetric around $E = 0$ if we neglect the constant in equation (4.36). The matrix $\mathcal{M}$ has twice the dimension of the number of fermionic degrees of freedom. Diagonalization will thus result in an overcounting, similar to the situation encountered in the closed Kitaev chain and equation (3.26),

$$H = \frac{1}{2}\sum_{i=1}^{N} E_i(d_i^\dagger d_i - d_i d_i^\dagger), \tag{4.41}$$

with d_i being quasiparticle annihilation operators,

$$d_i = \sum_{j=1}^{N} (q_{2i-1,2j} c_j^\dagger + q_{2i-1,2j-1} c_j). \tag{4.42}$$

The numbers $q_{i,j}$ are the matrix elements of Q. Specifically, $q_{2i-1,2j}$ and $q_{2i-1,2j-1}$ are numerical weights giving information of how present the fermion and hole state j is in the ith eigenstate respectively. The operators appearing in (4.42) are components of the vector

$$\boldsymbol{d} \equiv \begin{pmatrix} d_1, & d_1^\dagger, & d_2, & d_2^\dagger, & \dots, & d_N, & d_N^\dagger \end{pmatrix}^T = Q\boldsymbol{\Psi}. \tag{4.43}$$

One way of visualizing the eigenstates, corresponding to the positive eigenvalue (in front of $d_i^\dagger d_i$), is to plot the coefficients $q_{2i-1,2j}$ and $q_{2i-1,2j-1}$ against $j \in \{1, \dots, N\}$ to see the spatial distribution of the fermion content. Recall the Majorana zero modes we are expecting for $\Delta = t$ and $\mu = 0$, $\gamma_{A,1} = -i(c_1 - c_1^\dagger)$ and $\gamma_{B,N} = c_N + c_N^\dagger$. These modes should be combined to form the zero energy fermionic d_0 operator as in equation (4.17), $d_0 = i(c_N + c_N^\dagger - c_1 + c_1^\dagger)/2$. The appearance of d_0, corresponding to zero energy, can be used as a consistency check of the numerical implementation. We will return to this in the discussion.

4.4 Numerical Implementation, Results and Discussion

The diagonalization problem outlined in the last section was implemented numerically in a `C++` script, and the results were plotted with `Python`. Since the linear algebra package `Armadillo` in `C++` offers a wide range of effective methods, it was chosen as the preferred tool for the task [27]. The `Armadillo` package has a built-in function called `eig_sym()` that returns the eigenvectors and eigenvalues of any symmetric matrix. For simplicity, the superconducting phase was fixed to $\phi = 0$. Then, the matrix $\mathcal{M}$ becomes real and symmetric, and the matrix diagonalization theorem ensures that Q is orthogonal, $Q^T = Q^{-1}$. The core of the `C++` code can be found attached in Appendix D.1. It exemplifies the implementation for a spatially varying order parameter. However, as a first demonstration we fix $\Delta = \Delta_0 = \text{const}$.

4.4.1 Results with Constant Order Parameter

In the inset of Figure 4.2, a plot of the (double) energy spectrum with constant order parameter is shown for a representative range of chemical potentials, $\mu \in [-2t, 2t]$. Notice that there are exactly two values – meaning one fermionic state – approaching zero energy at $|\mu| = t$. At the transitions, $\mu = \pm t$, we observe that the energy gap closes and reopens as $|\mu| < t$, with two values staying at zero energy.

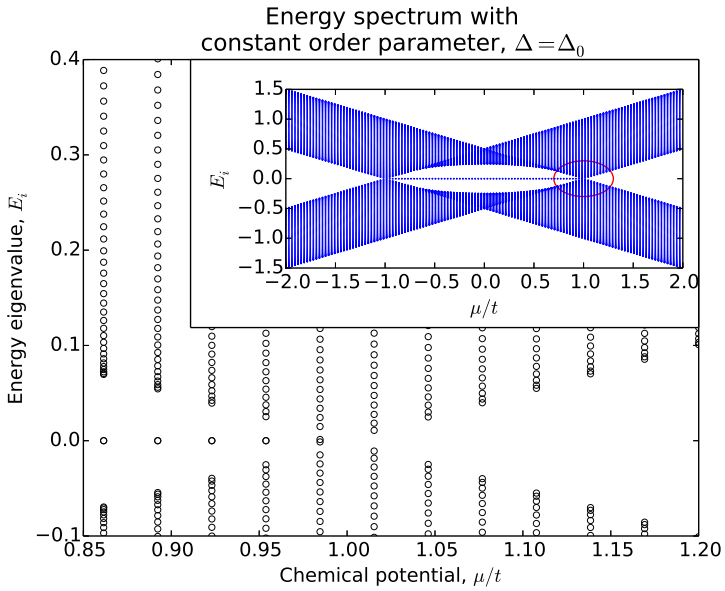

Figure 4.2: Energy spectrum of an open Kitaev chain with constant order parameter $\Delta = \Delta_0 = 0.5$. The main plot shows a zoomed energy spectrum close to the phase transition $\mu = t$. The inset shows the full spectrum plotted for different values of chemical potential in the range $\mu \in [-2t, 2t]$ with the zoom marked in red. The number of sites was set to $N = 80$, meaning that there are 160 energy eigenvalues for each value of μ. The hopping parameter was fixed to $t = 1.0$.

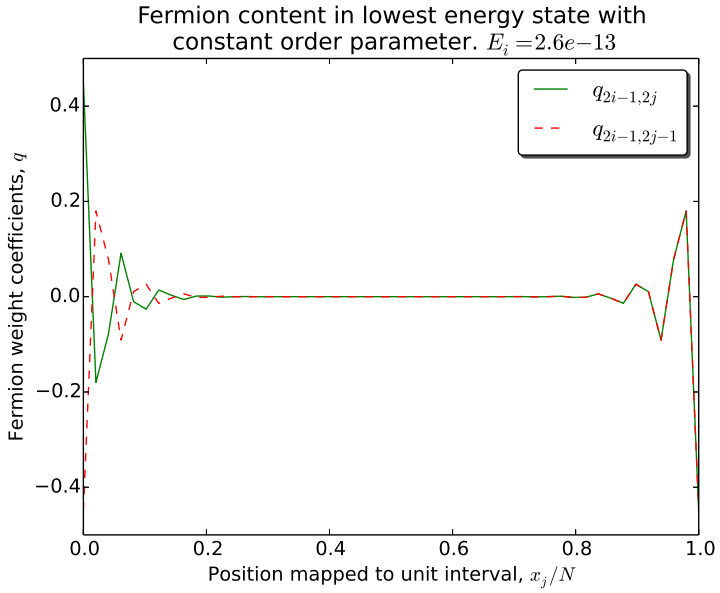

Figure 4.3: Fermion content of the lowest energy fermionic state in the open Kitaev chain. The matrix coefficients q from equation (4.42) are plotted against x_j/N. This plot was produced with $N = 50$ sites, hopping parameter $t = 1.0$, order parameter $\Delta = \Delta_0 = 0.5$ and chemical potential $\mu = 0.3t$. The energy E_i in the figure title refers to the numerically found (positive) eigenvalue.

In Figure 4.3 the coefficients $q_{2i-1,2j}$ (in front of $c_j^\dagger$) and $q_{2i-1,2j-1}$ (in front of c_j), with E_i corresponding to the smallest (positive) energy value, are plotted as function

of j in the topological phase, $\mu = 0.3t$. We observe that the coefficients have significant contributions towards the two ends, and that the coefficients are of equal absolute magnitude. Note also that the orthogonality of the eigenvectors, $Q^T Q = \mathbb{1}$, determines the normalization of the matrix coefficients in this figure. We return to the choices of parameters and a discussion of the results in the end of this section.

4.4.2 Results with Spatially Varying Order Parameter

Next, we study the effect of having a position dependent order parameter $\Delta = \Delta_x$. This is partly motivated by the fact that we in the next chapter study how a single Majorana mode is localized close to the core of a vortex in two spatial dimensions. A vortex will there be characterized by an order parameter with a certain radial profile approaching zero in the vortex center. Perhaps similar effects can take place with a position dependent order parameter in a one-dimensional model. Let therefore Δ_x be a (real) function that at some point passes zero and has the asymptotic value Δ_0. We propose the following parametrized model of a kinked order parameter:

$$\Delta_x = -\Delta_0 \tanh\Big((x - N/2)/s\Big). \tag{4.44}$$

This function crosses zero at $x = N/2$. Its steepness towards the crossing is controlled by adjusting the parameter s. *A priori*, one might question the necessity of a sign change in Δ_x, so we will do exactly same analysis with $|\Delta_x|$ for comparison. In Figure 4.4 we have plotted Δ_x and $|\Delta_x|$ from equation (4.44) with $s = 10$ for reference.

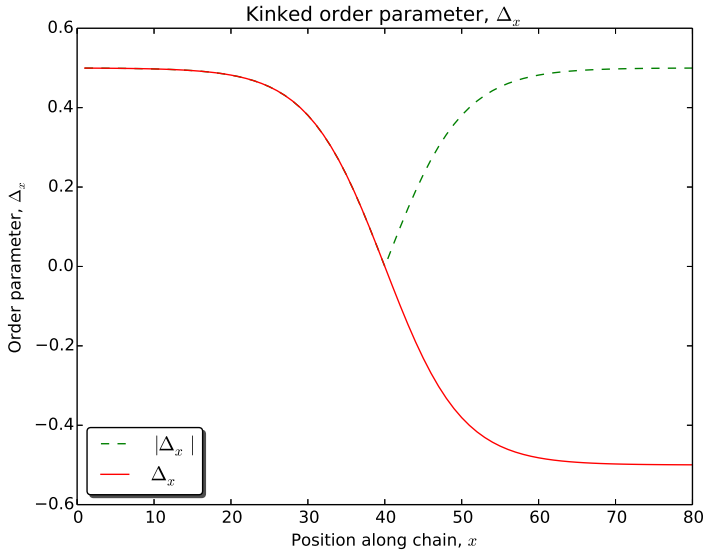

Figure 4.4: Position varying order parameter, Δ_x (red) and $|\Delta_x|$ (green). The function Δ_x is described in equation (4.44) and plotted here with $s = 10$ and $\Delta_0 = 0.5$. The number of sites was fixed to $N = 80$.

A diagonalization similar to that with constant Δ was implemented with the kinked order parameter, both Δ_x and $|\Delta_x|$. The resulting energy spectra are shown in Figure 4.5. There is one immediate observation to be made. When Δ changes sign, a total of four energy values – meaning two fermionic degrees of freedom – approaches zero energy at $|\mu| = t$, whereas no additional zero energy states appear when the sign of Δ is constant. It can be seen in Figure 4.5(b) that one energy band is deflected into the gapped regime at $|\mu| < t$, apparently the band that approaches zero energy in Figure 4.5(a).

Finally, we provide a plot of the zero energy states as they appear with $\Delta = \Delta_x$ in Figure 4.5(a). Denote the two smallest (positive) energies by E_i and E_l. In Figure 4.6 the matrix weighting coefficients $q_{2i-1,2j}$, $q_{2i-1,2j-1}$, $q_{2l-1,2j}$ and $q_{2l-1,2j-1}$ are plotted as function of j. Note that the four coefficients are associated with two fermionic annihilation operators, d_i and d_l, as in equation (4.42). The weights have all non-zero contributions on both ends of the chain (as before) and additional weight in the central region where Δ_x crosses zero.

4.4.3 Discussion and Comparison with the Literature

During these simulations, energy values appearing in pairs of opposite signs was used as a program test. That is, the resulting energy values are supposed to respect the particle-hole symmetry. Numerically, however, we observed that when N was increased, or μ chosen sufficiently close to zero, the resulting ground state energy become of equal magnitude as the floating point precision of the computer.[3] Consequently, the lowest energy pair did not appear exactly equal in absolute value. This numerical violation the particle-hole symmetry also resulted in eigenstates rotated within the ground state manifold, preferably giving weights on one or the other side of the chain. This problem boils down to how the `Armadillo` function `eig_sym()` specifically finds eigenvectors, and it could possibly have been avoided by developing a code from scratch. Instead, we kept the system sizes small and used the appearance of paired eigenvalues as an indication of whether the correct eigenvectors were returned or not. Exactly this problematic effect was present when fixing $\Delta = t$ and $\mu = 0$. Instead of observing the weights of d_0 returned, the numerics yielded the Majorana modes $-c_1 + c_1^\dagger$ or $c_N + c_N^\dagger$ with weights on either side of the system. The system size and parameters in the figures were chosen to avoid this problem, which is the reason for using $N = 50$ and not $N = 80$ in Figure 4.3.

The results with constant order parameter demonstrate that there is a non-trivial and important consequence of having an open Kitaev chain in the topological phase, $|\mu| < t$. Namely, that one Majorana zero mode emerge on each of the open ends. The modes are the constituents of a fermionic operator associated with (exponentially close to) zero energy. When the order parameter was varied spatially, $\Delta = \Delta_x$, we observe in Figure 4.5(a) that two new Majorana modes appear when Δ changes

[3] Typically, a number with `double` floating-point precision in `C++` have 15-17 significant decimal digits [27].

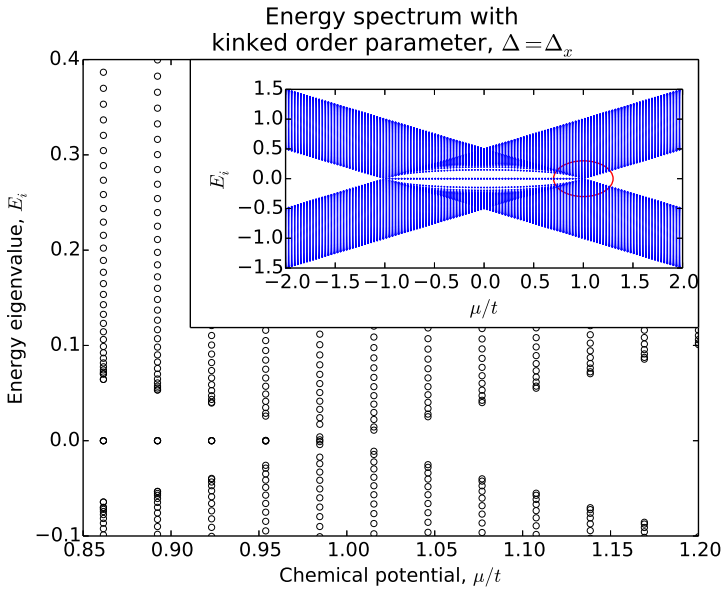

(a)

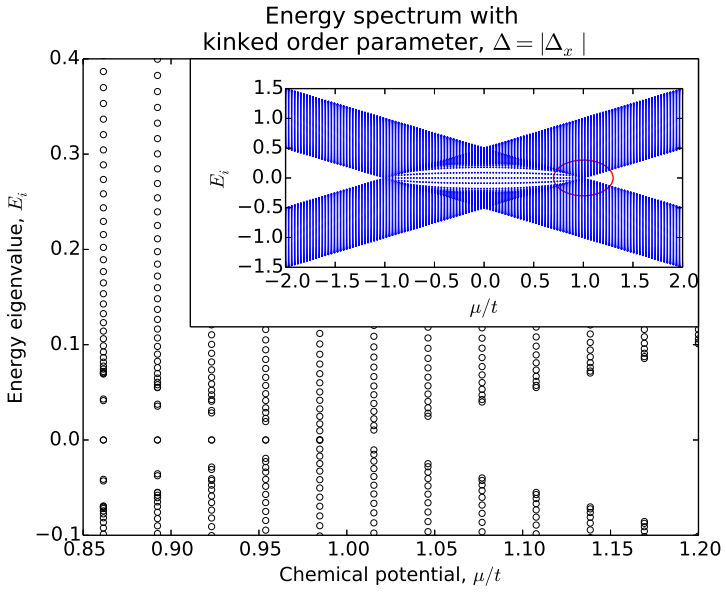

(b)

Figure 4.5: Energy spectrum of open Kitaev chain with **(a)** $\Delta = \Delta_x$ and **(b)** $\Delta = |\Delta_x|$. The order parameter is given by equation (4.44) with $s = 10$ and $\Delta_0 = 0.5$. The main plots show the zoomed energy spectra close to the phase transition $\mu = t$. The insets show the spectra plotted for different values of chemical potential in the range $\mu \in [-2t, 2t]$ with the zoom marked in red. The number of sites was set to $N = 80$. The hopping parameter was fixed to $t = 1.0$.

sign. This basic observation was seen to be robust in s. Specifically, by increasing s significantly – making the zero-crossing of Δ_x more spread out in space – the only observed change was that the central peaks in Figure 4.6 were widened. In crucial contrast, new zero modes did never seem to appear with $\Delta_x = |\Delta_x|$, still independent of s. Moreover, the central zero modes appearing with $\Delta = \Delta_x$ have a significant overlap but they nonetheless coexist, i.e. they do not split in energy and

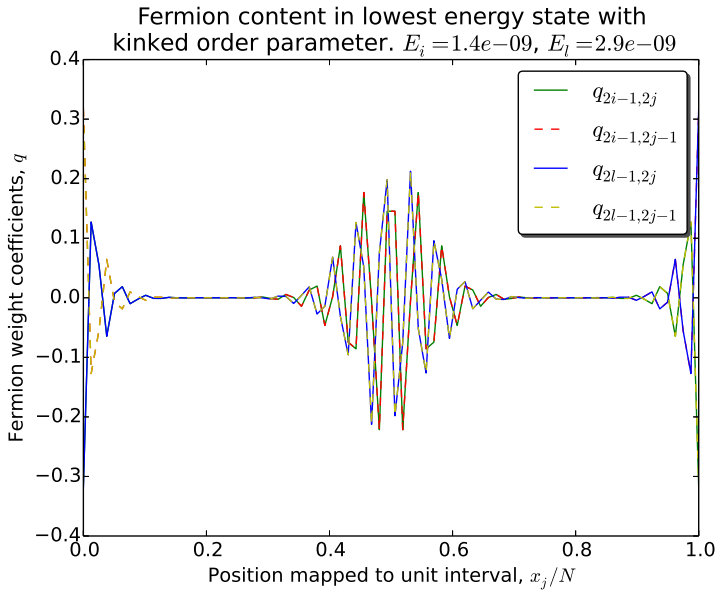

Figure 4.6: Fermion content of the two lowest energy fermionic states in the open Kitaev chain with position varying order parameter. The matrix coefficients q, as in equation (4.42), are plotted against x_j/N. This plot was produced with $N = 80$ sites, hopping parameter $t = 1.0$, chemical potential $\mu = 0.3t$ and $\Delta = \Delta_x$ as in equation (4.44) with $s = 10$ and $\Delta_0 = 0.5$. The energies E_i and E_l refer to the numerically found (positive) eigenvalues.

hybridize. This leads us to think that the sign change of Δ has roots in topological properties of the Kitaev chain.

While working with this problem we became aware of a recent article where similar effects are studied. In [28] T. H. Hansson et al. discuss zero modes resulting from π-junctions in Δ on more general grounds. In their treatment, *phase winding junctions*, where the phase of the order parameter winds by a position dependent angle, are considered. They argue that a real order parameter going through zero always gives rise to two additional zero modes in the topological phase for p-wave chains. This happens regardless of the details on how the order parameter passes zero. However, when the phase winding becomes genuinely complex, i.e. not rotating from 0 to π from one site to the next, no additional zero modes than those on the ends of the chain appear.

The difference between complex and real junctions, they argue, is more deeply rooted in symmetry classes. The authors observe that the Kitaev chain with real order parameter and real hopping strength belongs to the BDI symmetry class (TRS is +1), while it belongs to class D (TRS is 0) when they are both complex. A BDI Kitaev chain has two distinct realizations of the topological phase. A key observation supporting this view can actually be made from Figure 3.3. With $\phi = 0$ we see that the transformation $\Delta \to -\Delta$ alters the circulation of $\boldsymbol{h}(k)$ from clockwise to counter-clockwise in the yz-plane. The two values $\pm\Delta$ correspond to opposite winding numbers, ν. In other words, $\pm\Delta$ are distinct topological phases, and two

zero energy Majorana modes appear on the boundary between the phases. The simulations shown in Figure 4.5 and 4.6 are in agreement with and underpins this conclusion. Finally, that $\pm\Delta$ are distinct realizations of the topological phase might explain the fact that we observe two coexisting zero modes with significant spatial overlap in Figure 4.6. Overlapping zero modes are normally expected to split in a finite $\pm E$ pair. With these remarks we conclude our discussion of the Kitaev chain.

Chapter 5

The $p + ip$ Model and Vortices with Majorana Modes

A two-dimensional model with p-wave paired and effectively spinless electrons is studied. First, we establish the formal framework for the model. This includes deriving the diagonalization equations. Thereafter, the idea of a space varying order parameter will be pursued. In particular, we search for Majorana zero mode solutions in an infinite system with a rotationally symmetric vortex. In 2007 V. Guriare and L. Radzihovsky studied this system analytically in the limit where $|\Delta(\boldsymbol{r})|$ is non-constant in an infinitesimally small region [13]. We depart from their study by using a vortex solution in accordance with Ginzburg-Landau theory. Moreover, we propose an argument that implies non-Abelian exchange statistics in a system of several vortices. This property is known from Ivanov's compact consideration [6]. However, our argument is, in contrast to Ivanov's derivation, based on conservation of fermion parity. The $p + ip$ mean field model, which is valid with a non-homogeneous order parameter (see for instance [6, 12]), is given by

$$H = \int \mathrm{d}^2 r\, \psi^\dagger(\boldsymbol{r}) \left(-\frac{\hbar^2}{2m}\nabla^2 - \mu \right) \psi(\boldsymbol{r}) + \frac{1}{2} \int \mathrm{d}^2 r\, \mathrm{d}^2 r' \left(\psi^\dagger(\boldsymbol{r}) D(\boldsymbol{r}, \boldsymbol{r}') \psi^\dagger(\boldsymbol{r}') + \mathrm{h.c.} \right). \tag{5.1}$$

Above, $\psi^\dagger(\boldsymbol{r})$ is the creation operator of a spinless fermion in position $\boldsymbol{r}$. The operators satisfy fermionic anticommutation relations

$$\{\psi(\boldsymbol{r}), \psi^\dagger(\boldsymbol{r}')\} = \delta^{(2)}(\boldsymbol{r} - \boldsymbol{r}') \quad \text{and} \quad \{\psi(\boldsymbol{r}), \psi(\boldsymbol{r}')\} = \{\psi^\dagger(\boldsymbol{r}), \psi^\dagger(\boldsymbol{r}')\} = 0, \tag{5.2}$$

with $\delta^{(2)}(\boldsymbol{r} - \boldsymbol{r}')$ being the two-dimensional Dirac delta function. The pairing function $D(\boldsymbol{r}, \boldsymbol{r}')$ is defined by

$$D(\boldsymbol{r}, \boldsymbol{r}') = \Delta \left(\frac{\boldsymbol{r} + \boldsymbol{r}'}{2} \right) (\partial_{x'} + i\partial_{y'}) \delta^{(2)}(\boldsymbol{r} - \boldsymbol{r}'). \tag{5.3}$$

We open the chapter with a brief presentation of the model in an in infinite system with constant order parameter to point out the analogy to the closed Kitaev chain and to motivate the topological classification.

5.1 Homogeneous System

We summarize some essential properties of the model as discussed in [11, 24] for completeness. Assume that the order parameter is homogeneous, $\Delta(\boldsymbol{r}) = \Delta_0 e^{i\phi}$, with ϕ some general phase and Δ_0 a real, positive constant. The Hamiltonian in (5.1) reduce to[1]

$$H = \int \mathrm{d}^2 r \left(\psi^\dagger(\boldsymbol{r}) \left(-\frac{\hbar^2}{2m}\nabla^2 - \mu \right) \psi(\boldsymbol{r}) + \frac{\Delta_0}{2} \left(e^{i\phi}\psi^\dagger(\boldsymbol{r})(\partial_x + i\partial_y)\psi^\dagger(\boldsymbol{r}) + \text{h.c.} \right) \right). \tag{5.4}$$

By introducing a momentum representation of the fermionic operators,

$$\psi(\boldsymbol{k}) = \int \mathrm{d}^2 r \, e^{-i\boldsymbol{k}\cdot\boldsymbol{r}} \psi(\boldsymbol{r}) \quad \text{and} \quad \psi(\boldsymbol{r}) = \int \frac{\mathrm{d}^2 k}{(2\pi)^2} e^{i\boldsymbol{k}\cdot\boldsymbol{r}} \psi(\boldsymbol{k}), \tag{5.5}$$

one may diagonalize the Hamiltonian. Inserting the transformed operators in the Hamiltonian (5.4) and using $\int \mathrm{d}^2 r \, e^{i\boldsymbol{r}\cdot(\boldsymbol{k}-\boldsymbol{k}')} = (2\pi)^2 \delta^{(2)}(\boldsymbol{k} - \boldsymbol{k}')$, results in the expression (compare with equation (3.12)),

$$H = \frac{1}{2} \int \frac{\mathrm{d}^2 k}{(2\pi)^2} \boldsymbol{\Psi}^\dagger(\boldsymbol{k}) \mathcal{H}(\boldsymbol{k}) \boldsymbol{\Psi}(\boldsymbol{k}), \tag{5.6}$$

with

$$\boldsymbol{\Psi}(\boldsymbol{k}) \equiv \begin{pmatrix} \psi(\boldsymbol{k}) \\ \psi^\dagger(-\boldsymbol{k}) \end{pmatrix} \quad \text{and} \quad \mathcal{H}(\boldsymbol{k}) \equiv \begin{pmatrix} \epsilon(k) & \Delta(\boldsymbol{k}) \\ \Delta^*(\boldsymbol{k}) & -\epsilon(k) \end{pmatrix}. \tag{5.7}$$

Moreover, we introduced the functions

$$\epsilon(k) \equiv \frac{\hbar^2 k^2}{2m} - \mu \quad \text{and} \quad \Delta(\boldsymbol{k}) \equiv i\Delta_0 e^{i\phi}(k_x + ik_y). \tag{5.8}$$

The eigenvalues of $\mathcal{H}(\boldsymbol{k})$ define the quasiparticle spectrum and are given by

$$\pm E(k) = \pm\sqrt{\epsilon(k)^2 + |\Delta(\boldsymbol{k})|^2} = \pm\sqrt{\left(\frac{\hbar^2 k^2}{2m} - \mu \right)^2 + \Delta_0^2 k^2}. \tag{5.9}$$

[1] This follows by making use of the Dirac delta function property $\int \mathrm{d}x \, f(x)\partial_{x'}\delta(x - x') = \frac{\mathrm{d}f(x')}{\mathrm{d}x'}$.

A plot of the spectrum is shown in Figure 5.1; it should be compared to Figure 3.1. In the present case, the energy gap closes only at $\mu = 0$ for $k = 0$. We will not derive a topological classification of this model similar to what was done in section 3.3. However, the energy spectrum in Figure 5.1, along with the knowledge established in earlier chapters, should at this point give a strong indication that $\mu > 0$ and $\mu < 0$ determine the distinction between the topological and the trivial regime. Read and Green demonstrated that $\mu > 0$ should be characterized as the topological and $\mu < 0$ as the trivial phase [24]. The distinction, they showed, is reflected in the long range behaviour of the inverse Fourier transform of the analogue of the coefficient g_k from equation (3.34). It decays exponentially in the trivial region and algebraically in the topological region. We will simply keep this characterization in mind and search for zero modes with the assumption that $\mu > 0$.

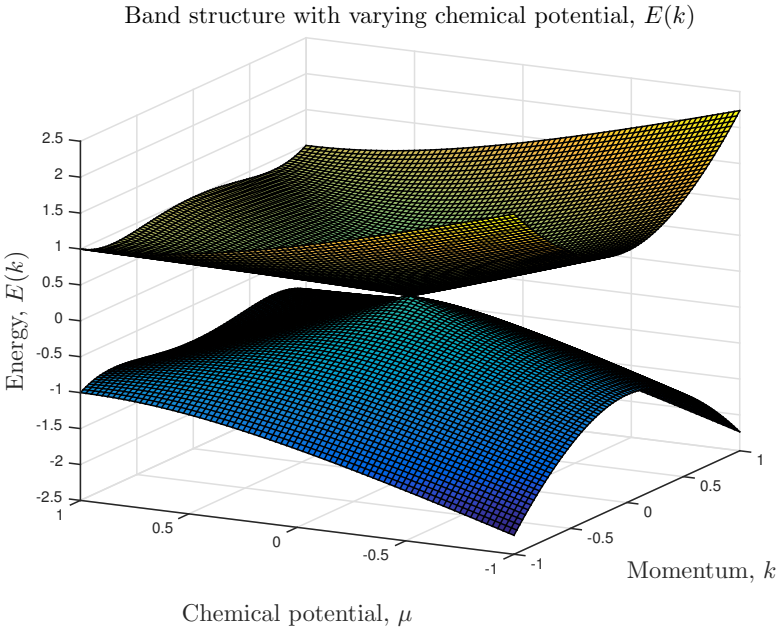

Figure 5.1: Energy spectrum as function of momentum $k \in [-1, 1]$ and chemical potential μ in the range $\mu \in [-1, 1]$. Both the order parameter and the kinetic prefactor were fixed to $\Delta_0 = \hbar^2/(2m) = 1.0$. The gap closes at $k = 0$ for $\mu = 0$.

Read and Green also make a thorough analysis of the ground state for all four combinations of closed boundary conditions, i.e. periodic or anti-periodic in k_x and/or k_y. The $\boldsymbol{k} = (0, 0)$ mode is present only with periodic boundary conditions in both directions, and it essentially plays the same role as the unpaired mode $k = 0$ that we encountered in the closed Kitaev chain.

5.2 Derivation of the BdG Equations

This section is devoted to a derivation of the Bogoliubov-de-Gennes (BdG) equations for the general model in (5.1). The philosophy of our approach is inspired by [29], but we fill in several details that were not found described in that reference. Recall the Hamiltonian we are considering,

$$H = \int \mathrm{d}^2 r\, \psi^\dagger(\boldsymbol{r}) \left(-\frac{\hbar^2}{2m}\nabla^2 - \mu \right) \psi(\boldsymbol{r}) + \frac{1}{2} \int \mathrm{d}^2 r\, \mathrm{d}^2 r' \left(\psi^\dagger(\boldsymbol{r}) D(\boldsymbol{r}, \boldsymbol{r}') \psi^\dagger(\boldsymbol{r}') + \text{h.c.} \right). \tag{5.10}$$

Assume that there is a countable set of many-particle operators, $\{\Gamma_n\}_{n=1}^{\infty}$, that diagonalize the Hamiltonian,[2]

$$H = E_\Omega + \sum_n E_n\, \Gamma_n^\dagger \Gamma_n, \tag{5.11}$$

with E_Ω as the ground state energy, which we simply neglect. The sum runs over positive eigenvalues, $E_n \geq 0$. Zero modes, denoted by γ_n corresponding to $E_n = 0$, do clearly not contribute to this spectral decomposition. The ansatz (5.11) can be motivated by the related expression we arrived at in the case of the closed Kitaev chain. Recall from equation (3.26) that the positive and negative energy bands merged in a single sum running over the positive eigenvalues. This had to do with our definition of the quasiparticle operators being associated with positive energy. The new field operators should preserve the fermionic statistics of the normal fermions. We therefore impose them to satisfy

$$\{\Gamma_n, \Gamma_m^\dagger\} = \delta_{m,n} \quad \text{and} \quad \{\Gamma_n, \Gamma_m\} = \{\Gamma_n^\dagger, \Gamma_m^\dagger\} = 0. \tag{5.12}$$

If we were to assume that the new operators should satisfy bosonic commutation relations, we would quickly run into consistency problems with the completeness relations that are soon to be derived. A Bogoliubov transformation determines the relation between $\psi(\boldsymbol{r})$ and Γ_n,

$$\psi(\boldsymbol{r}) = \sum_n \Big(u_n(\boldsymbol{r}) \Gamma_n + v_n^*(\boldsymbol{r}) \Gamma_n^\dagger \Big). \tag{5.13}$$

Combining (5.13) with the anticommutation relations (5.2) and (5.12) leads to restrictions on the expansion coefficients, $u_n(\boldsymbol{r})$ and $v_n(\boldsymbol{r})$, which are not described in [29]. We find the following *completeness relations*:

$$\begin{aligned} \sum_n \Big[u_n(\boldsymbol{r}) u_n^*(\boldsymbol{r}') + v_n(\boldsymbol{r}') v_n^*(\boldsymbol{r}) \Big] &= \delta^{(2)}(\boldsymbol{r} - \boldsymbol{r}'), \\ \sum_n \Big[u_n(\boldsymbol{r}) v_n^*(\boldsymbol{r}') + u_n(\boldsymbol{r}') v_n^*(\boldsymbol{r}) \Big] &= 0. \end{aligned} \tag{5.14}$$

The two relations enable us to find the inverse transformation of (5.13). It can quickly be verified, by inserting (5.13), that

[2] This basic assumption may be questioned as it seems that we demand a map from an uncountable infinity (set of fermion operators) to a countable one (set of quasiparticle operators). Since we will focus on the zero energy modes, one may hope that subtleties related to this mapping will not interfere with the argument.

$$\Gamma_n = \int \mathrm{d}^2 r \Big(u_n^*(\boldsymbol{r})\psi(\boldsymbol{r}) + v_n^*(\boldsymbol{r})\psi^\dagger(\boldsymbol{r}) \Big). \tag{5.15}$$

When this expression is combined with the anticommutation relations in (5.12), we find a set of *orthonormality relations* in the continuous position space,

$$\begin{aligned} \int \mathrm{d}^2 r \Big(u_n^*(\boldsymbol{r})u_m(\boldsymbol{r}) + v_n^*(\boldsymbol{r})v_m(\boldsymbol{r}) \Big) &= \delta_{n,m}, \\ \int \mathrm{d}^2 r \Big(v_n(\boldsymbol{r})u_m(\boldsymbol{r}) + u_n(\boldsymbol{r})v_m(\boldsymbol{r}) \Big) &= 0. \end{aligned} \tag{5.16}$$

One may think of (5.16) as orthogonality of two-components spinors,

$$\boldsymbol{\phi}_n(\boldsymbol{r}) \equiv \begin{pmatrix} u_n(\boldsymbol{r}) \\ v_n(\boldsymbol{r}) \end{pmatrix}, \tag{5.17}$$

with the following type of inner product:

$$\langle \boldsymbol{\phi}_n | \boldsymbol{\phi}_m \rangle \equiv \int \mathrm{d}^2 r \; \boldsymbol{\phi}_n^\dagger(\boldsymbol{r}) \boldsymbol{\phi}_m(\boldsymbol{r}). \tag{5.18}$$

This spinor description will be used frequently in the next chapter. The most important consequence of demanding fermionic anticommutation of the Γ_n operators is, however, obtained by combination of (5.11) and (5.12) (this idea is taken from [29]),

$$[H, \Gamma_n] = -E_n \, \Gamma_n \quad \text{and} \quad [H, \Gamma_n^\dagger] = E_n \, \Gamma_n^\dagger. \tag{5.19}$$

This is exploited to determine the equations that u_n and v_n have to satisfy in order to diagonalize the Hamiltonian.[3] We calculate $[H, \psi(\boldsymbol{r})]$ in two different ways. First, we exploit (5.13):

$$\begin{aligned} [H, \psi(\boldsymbol{r})] &= \sum_n \left(u_n(\boldsymbol{r})[H, \Gamma_n] + v_n^*(\boldsymbol{r})[H, \Gamma_n^\dagger] \right) \\ &= \sum_n E_n \left(-u_n(\boldsymbol{r})\Gamma_n + v_n^*(\boldsymbol{r})\Gamma_n^\dagger \right). \end{aligned} \tag{5.20}$$

Secondly, we calculate $[H, \psi(\boldsymbol{r})]$ explicitly. The pairing term in the Hamiltonian, let it be denoted by H_Δ, should be slightly rewritten to easier evaluate $[H_\Delta, \psi(\boldsymbol{r})]$. After making use of the properties of the Dirac delta function and the Fermi-Dirac statistics, $(\psi^\dagger(\boldsymbol{r}))^2 = 0$, it may be expressed as

[3] Exploiting the relations in (5.19) to find the diagonalization condition should in principle amount to the same as inserting (5.13) directly into the Hamiltonian and demand the off-diagonal terms to vanish. However, the latter procedure quickly becomes a tedious approach.

$$H_\Delta \equiv \frac{1}{2}\int \mathrm{d}^2r\, \mathrm{d}^2r'\, \psi^\dagger(\boldsymbol{r})D(\boldsymbol{r},\boldsymbol{r}')\psi^\dagger(\boldsymbol{r}') = \frac{1}{2}\int \mathrm{d}^2r\, \psi^\dagger(\boldsymbol{r})\Delta(\boldsymbol{r})\partial_{z^*}\psi^\dagger(\boldsymbol{r}). \tag{5.21}$$

Above, the complex variable $z = x + iy$ was introduced such that

$$\partial_{z^*} = \partial_x + i\partial_y = e^{i\theta}(\partial_r + \frac{i}{r}\partial_\theta). \tag{5.22}$$

The hermitian conjugate of the pairing term, $H_\Delta^\dagger$, simply commutes with $\psi(\boldsymbol{r})$. The commutator of the kinetic term in H and $\psi(\boldsymbol{r})$ is trivially found by using the anticommutation relations in (5.2). In total, the commutator evaluates to

$$[H, \psi(\boldsymbol{r})] = \left(\frac{\hbar^2}{2m}\nabla^2 + \mu\right)\psi(\boldsymbol{r}) - \frac{1}{2}\{\Delta(\boldsymbol{r}), \partial_{z^*}\}\psi^\dagger(\boldsymbol{r}). \tag{5.23}$$

Inserting the Bogoliubov transformation (5.13) in this expression and comparing termwise with (5.20) gives

$$-E_n u_n \Gamma_n + E_n v_n^* \Gamma_n^\dagger = \left(\frac{\hbar^2}{2m}\nabla^2 + \mu\right)(u_n\Gamma_n + v_n^*\Gamma_n^\dagger) - \frac{1}{2}\{\Delta(\boldsymbol{r}), \partial_{z^*}\}(u_n^*\Gamma_n^\dagger + v_n\Gamma_n). \tag{5.24}$$

Equating terms in front of Γ_n and $\Gamma_n^\dagger$ separately yields the BdG equations,

$$\begin{aligned} -\left(\frac{\hbar^2}{2m}\nabla^2 + \mu\right)u_n(\boldsymbol{r}) + \frac{1}{2}\{\Delta(\boldsymbol{r}), \partial_{z^*}\}v_n(\boldsymbol{r}) &= E_n u_n(\boldsymbol{r}), \\ \left(\frac{\hbar^2}{2m}\nabla^2 + \mu\right)v_n(\boldsymbol{r}) - \frac{1}{2}\{\Delta^*(\boldsymbol{r}), \partial_z\}u_n(\boldsymbol{r}) &= E_n v_n(\boldsymbol{r}). \end{aligned} \tag{5.25}$$

5.2.1 Majorana Zero Modes

Some of the above expressions are slightly altered for zero modes, γ_n. A Majorana operator associated with zero energy is by definition hermitian and commutes with the Hamiltonian,

$$\gamma_n = \gamma_n^\dagger \quad \text{and} \quad [H, \gamma_n] = 0. \tag{5.26}$$

The expansion (5.15) reveals that it must satisfy $u_n(\boldsymbol{r}) = v_n^*(\boldsymbol{r})$, and it thereby constitutes half a fermionic degree of freedom,

$$\gamma_n = \int \mathrm{d}^2r\Big(u_n^*(\boldsymbol{r})\psi(\boldsymbol{r}) + u_n(\boldsymbol{r})\psi^\dagger(\boldsymbol{r})\Big). \tag{5.27}$$

The hermiticity of γ_n forces us to modify the fundamental commutation relations in (5.12). We adopt a common normalization convention, for instance used in [5, 11], and demand that

$$\{\gamma_n, \gamma_m\} = 2\delta_{n,m} \quad \text{such that} \quad \gamma_n^2 = 1. \tag{5.28}$$

In terms of the completeness relation in (5.16), normalization of the zero modes is done according to

$$\int \mathrm{d}^2 r \left(u_n^*(\boldsymbol{r}) u_m(\boldsymbol{r}) + u_m^*(\boldsymbol{r}) u_n(\boldsymbol{r}) \right) = 2\delta_{n,m} \Rightarrow \int \mathrm{d}^2 r \, |u_n(\boldsymbol{r})|^2 = 1. \tag{5.29}$$

The quantity $|u_n(\boldsymbol{r})|^2$ is interpreted as describing the spatial probability density of the zero mode.

5.3 Radial Zero Mode Equation

The formalism from the previous section will now be put to use. An equation governing a Majorana zero mode bound to a vortex is derived. The starting point of this derivation is inspired by [13]. However, we will depart from the description in that reference when arguing how the vorticity (mod 2) determines if zero modes are allowed. Moreover, we will in the next section combine the zero mode equation with a vortex profile in accordance with a minimal Ginzburg-Landau description, not restricting ourselves to studying infinitesimally small vortex cores. As far as we know, this more complete description has not been explored in detail before. The BdG equations will be solved numerically. They may, according to (5.25), be formulated as[4]

$$\begin{pmatrix} -\frac{\hbar^2}{2m}\nabla^2 - \mu & \frac{1}{2}\{\Delta(\boldsymbol{r}), \partial_{z^*}\} \\ -\frac{1}{2}\{\Delta^*(\boldsymbol{r}), \partial_z\} & \frac{\hbar^2}{2m}\nabla^2 + \mu \end{pmatrix} \begin{pmatrix} u(\boldsymbol{r}) \\ v(\boldsymbol{r}) \end{pmatrix} = E \begin{pmatrix} u(\boldsymbol{r}) \\ v(\boldsymbol{r}) \end{pmatrix}. \tag{5.30}$$

Above, we suppressed the index n. An alternative formulation is

$$\begin{aligned} -\left(\frac{\hbar^2}{2m}\nabla^2 + \mu \right) u(\boldsymbol{r}) + \sqrt{\Delta(\boldsymbol{r})}\partial_{z^*} \left[v(\boldsymbol{r}) \sqrt{\Delta(\boldsymbol{r})} \right] &= E u(\boldsymbol{r}), \\ \left(\frac{\hbar^2}{2m}\nabla^2 + \mu \right) v(\boldsymbol{r}) - \sqrt{\Delta^*(\boldsymbol{r})}\partial_z \left[u(\boldsymbol{r}) \sqrt{\Delta^*(\boldsymbol{r})} \right] &= E v(\boldsymbol{r}). \end{aligned} \tag{5.31}$$

We consider an ansatz for the order parameter, $\Delta(\boldsymbol{r})$, describing a rotationally symmetric vortex. Its radial profile is determined by some real function $g_\ell^2(r)$ (the power of 2 is simply included for convenience),

[4] Notice that the matrix in (5.30) is traceless, meaning that its two eigenvalues take the form $\pm E$. This manifestation of the particle-hole symmetry is also seen by observing that the matrix anticommutes with $\Xi \equiv \sigma_x \kappa$, where κ is the complex conjugation operator.

$$\Delta(\boldsymbol{r}) = g_\ell^2(r)e^{i\ell\theta + i\pi}. \tag{5.32}$$

Above, we chose to include an overall sign; this sign does not reflect anything measurable, and it functions merely as a redefinition of the order parameter to make the following consideration more fluent. The integer $\ell \in \mathbb{Z}$ is the *vorticity*, and $\hbar\ell$ is the angular momentum of the vortex fluid. Recall from section 2.3 that the vorticity is restricted to being integer by requiring that the order parameter is *single valued*. This will in fact be a crucial observation in the argument below. Later, it will be discussed how the ℓ-dependency of the profile g_ℓ^2 is determined. To keep notation simple, the subscript in g_ℓ will sometimes be abbreviated. A Majorana mode is characterized by

$$u(\boldsymbol{r}) = v^*(\boldsymbol{r}). \tag{5.33}$$

This condition, in combination with $E = 0$, ensures that the two equations in (5.31) reduce to the one and same. Therefore, it suffices to consider the first of them as long as (5.33) is fulfilled. Inserting the vortex ansatz (5.32) with $E = 0$ results in the (complex) equation

$$\begin{aligned} -\frac{\hbar^2}{2m}\Big(\frac{\partial^2}{\partial r^2} + \frac{1}{r}\frac{\partial}{\partial r} + \frac{1}{r^2}\frac{\partial^2}{\partial\theta^2}\Big)u(\boldsymbol{r}) - \mu u(\boldsymbol{r}) \\ - g(r)e^{i\theta\left(\frac{\ell}{2}+1\right)}\left(\frac{\partial}{\partial r} + \frac{i}{r}\frac{\partial}{\partial\theta}\right)\left[g(r)v(\boldsymbol{r})e^{i\theta\frac{\ell}{2}}\right] = 0. \end{aligned} \tag{5.34}$$

5.3.1 Solution Constraints

In order to discuss the solutions of this equation another argument is brought on stage. If the vortex in equation (5.32) is well behaved there are no terms in the Hamiltonian (5.1) that are singular at any point. Consequently, it is reasonable to assume that the solutions behave smoothly as well. Therefore, the fermionic fields $\psi(\boldsymbol{r})$ are required to be single valued, $\psi(r, \theta + 2\pi) = \psi(r, \theta)$. In turn, this puts restrictions on $u(\boldsymbol{r})$ and $v(\boldsymbol{r})$ seen by the expansion in (5.13). Both $u(\boldsymbol{r})$ and $v(\boldsymbol{r})$ must be single valued during a 2π winding of θ.

With these considerations in mind, one may try to transform away the polar angle dependency in (5.34) and obtain a (real) radial equation. In particular, we assume that the expansion coefficients are eigenstates of the angular momentum operator and apply the separational ansatz

$$u(\boldsymbol{r}) = \tilde{u}(r)e^{im\theta} \quad \text{and} \quad v(\boldsymbol{r}) = \tilde{v}(r)e^{-im\theta}, \tag{5.35}$$

with $m \in \mathbb{Z}$ denoting quantized angular momentum. This is in accordance with the criterion of single valued coefficients and the Majorana criterion (5.33), in particular if $\tilde{u}$ is real: $\tilde{u} = \tilde{u}^* = \tilde{v}$. Why the radial coefficient should be real will be understood

more clearly in the next chapter. To phrase it shortly, if $\tilde{u}$ was allowed to have an imaginary component, the solution would be increasing exponentially for large r. This is clearly in conflict with normalizability. Inserting (5.35) into (5.34), and requiring the polar angle dependency to be transformed away, leads to the connection

$$m = (\ell + 1)/2. \tag{5.36}$$

Crucially, this contradicts the fact that $m \in \mathbb{Z}$ when ℓ is even. Thus, if ℓ is even we are forced to implement an additional dependency on θ in $\tilde{u}(r)$ in order to respect the fermion fields being single valued: $\tilde{u}(r) \mapsto \tilde{u}(r)\exp(i\theta/2)$. However, letting $\tilde{u}$ be complex contradicts the realness criterion, $\tilde{u} = \tilde{u}^*$, and thereby equation (5.33). In turn, if $u(\boldsymbol{r}) \neq v^*(\boldsymbol{r})$ the two equations in (5.31) are not identical any more, and a possible solution of the equations does not describe a Majorana mode. We have therefore, by assuming ℓ to be even, arrived at a contradiction. Note that this does not prove that the equations (5.31) have *no* zero energy solutions for even vorticity. It demonstrates that possible zero energy solutions can not be Majorana solutions for even vorticity. Therefore, the possibility of *Majorana zero modes for even ℓ is excluded*.

On the other hand, if ℓ is assumed odd we can apply the separational ansatz in (5.35) with $m = (\ell + 1)/2$ to remove the angular dependency in equation (5.34) identically. The equation then reduces to

$$-\frac{\hbar^2}{2m}\left(\frac{\mathrm{d}^2}{\mathrm{d}r^2} + \frac{1}{r}\frac{\mathrm{d}}{\mathrm{d}r} - \frac{1}{r^2}\left(\frac{\ell+1}{2}\right)^2\right)\tilde{u} - \mu\tilde{u} - g^2\frac{\mathrm{d}\tilde{u}}{\mathrm{d}r} - g\frac{\mathrm{d}g}{\mathrm{d}r}\tilde{u} - \frac{g^2}{2r}\tilde{u} = 0. \tag{5.37}$$

Using more compact notation, $\tilde{u}' = \mathrm{d}\tilde{u}/\mathrm{d}r$ etc., we arrive at a homogeneous, second order differential equation,

$$\frac{\hbar^2}{2m}\tilde{u}'' + \left(g^2 + \frac{\hbar^2}{2mr}\right)\tilde{u}' + \left(\mu + \frac{g^2}{2r} + gg' - \frac{\hbar^2}{2mr^2}\left(\frac{\ell+1}{2}\right)^2\right)\tilde{u} = 0. \tag{5.38}$$

Note that equation (5.38) has an explicit breaking of the symmetry in ℓ about $\ell = 0$ that one might *a priori* expect. It can be traced back to arise from the $\partial_x + i\partial_y$ term in $D(\boldsymbol{r}, \boldsymbol{r}')$ in (5.3). This term makes the $p+ip$ model chiral, and it favours counter-clockwise complex rotations. If one instead were to consider the $p - ip$ model, the resulting zero mode equation becomes equal to (5.38) with the replacement $\ell \to -\ell$. The term containing ℓ is instead symmetric about $\ell = -1$. Thus, $\ell = -1$ will represent the fundamental vortex, $\ell = -3$ the next possible vorticity, and so on.

5.3.2 Dimensionless Formulation

Equation (5.38) is made dimensionless and ready for numerical implementation by introducing new variables. In particular, length is scaled with the *Ginzburg-Landau*

coherence length, a, as it appeared in section 2.3,

$$\rho \equiv \frac{r}{a}\,, \quad \xi \equiv \frac{\hbar^2}{2m}\,, \quad \eta \equiv \frac{a^2}{\xi}\mu \quad \text{and} \quad \tilde{g} \equiv \sqrt{\frac{a}{\xi}}g. \tag{5.39}$$

The dimensionless vortex equation becomes

$$\tilde{u}'' + \left(\tilde{g}^2 + \frac{1}{\rho}\right)\tilde{u}' + \left(\eta + \frac{\tilde{g}^2}{2\rho} + \tilde{g}\tilde{g}' - \frac{(\ell+1)^2}{4\rho^2}\right)\tilde{u} = 0, \tag{5.40}$$

where the derivatives are with respect to ρ. Equation (5.29) determines the normalization,

$$2\pi \int_0^\infty \mathrm{d}\rho\, \rho |\tilde{u}(\rho)|^2 = 1. \tag{5.41}$$

5.3.3 The Solutions in Limiting Cases

We consider two different limits of (5.40). First, we specialize to vanishing order parameter. If $\tilde{g}(\rho) = 0$ and $\eta > 0$, the differential equation in (5.40) is, not surprisingly, reduced to *Bessel's equation* (the reader is referred to Appendix C for more details),

$$\tilde{u}'' + \frac{\tilde{u}'}{\rho} + \left(\eta - \frac{(\ell+1)^2}{4\rho^2}\right)\tilde{u} = 0 \tag{5.42}$$

Two linearly independent solutions to this equation are spanned by Bessel functions,

$$\left\{ J_{\frac{|\ell+1|}{2}}(\sqrt{\eta}\rho), Y_{\frac{|\ell+1|}{2}}(\sqrt{\eta}\rho) \right\}. \tag{5.43}$$

However, equation (5.41) tells us that $\rho|\tilde{u}(\rho)|^2$ must be integrable for the solution to be normalizable. This is not satisfied by the Bessel functions. To be more precise, in Appendix C we prove that some absolute power of the nth order Bessel function, $|J_n(x)|^p$, is integrable only for $p > 2$. Hence, *no zero modes appear if* $\tilde{g}(\rho) = 0$. Moreover, the Bessel function $Y_n(x)$ is not finite at $x = 0$ and should anyhow be discarded as an acceptable solution of the problem. The contribution from the $\tilde{g}$-dependent parts of the equation contributes crucially to an exponential suppression of the solution, guaranteeing normalizability. Let us see this explicitly. We apply a separation trick,

$$\tilde{u}(\rho) = \chi(\rho) \exp\Big(-\frac{1}{2}\int_0^\rho \mathrm{d}\rho'\, \tilde{g}^2(\rho') \Big), \tag{5.44}$$

which reduces equation (5.40) to

$$\chi'' + \frac{\chi'}{\rho} + \left(\eta - \left(\frac{\tilde{g}^2}{2} \right)^2 - \frac{(\ell+1)^2}{4\rho^2} \right) \chi. \tag{5.45}$$

Thus, if the order parameter profile is $\tilde{g}^2(\rho) \equiv \delta_0$ with δ_0 constant and $(\delta_0/2)^2 < \eta$, equation (5.45) becomes Bessel's equation for χ. Therefore, the solutions with homogeneous order parameter are spanned by

$$\left\{ J_{\frac{|\ell+1|}{2}}(\sqrt{\eta - (\delta_0/2)^2}\rho) e^{-\frac{\delta_0}{2}\rho}, Y_{\frac{|\ell+1|}{2}}(\sqrt{\eta - (\delta_0/2)^2}\rho) e^{-\frac{\delta_0}{2}\rho} \right\}. \tag{5.46}$$

These special cases help building intuition about the solutions. We now discuss how to take a realistic vortex profile into account and then solve equation (5.40) numerically.

5.4 The Vortex Profile

Recall the vortex ansatz from equation (5.32), $\Delta(\boldsymbol{r}) = g_\ell^2(r) e^{i\ell\theta + i\pi}$. What remains unspecified is the radial vortex profile, $g_\ell^2(\rho)$. It is not trivial to determine this function rigorously. Still, BCS-theory offers one approach that was exploited by N. Hayashi et al. in [30] for a s-wave type-II superconductor. The authors solve the self-consistent *gap equation* to find the radial order parameter, even at finite temperatures. Another method is based on the phenomenological theory of Ginzburg and Landau. In section 2.3 Ginzburg-Landau theory was used to derive a non-linear equation that the superfluid pseudo wavefunction should satisfy. We will apply solutions of that equation as a description of the vortex.

In principle, the Ginzburg-Landau free energy should be extended for p-wave pairing, but this will not be considered for several reasons. Firstly, determining g_ℓ^2 properly would have become a comprehensive process, and the focus of our analysis would be shifted considerably towards a detailed description of vortices. Secondly, after a scan of relevant literature, no easily accessible approach to the proper Ginzburg-Landau description with p-wave pairing was found. Finally, and most importantly, the zero mode solutions will turn out to have only a weak dependency on the specific shape of the vortex profile. The basic and most important properties are already captured by the minimal description from section 2.3. Recall the non-linear and dimensionless superfluid equation,

$$\nabla^2 \hat{\psi} + (1 - |\hat{\psi}|^2)\hat{\psi} = 0. \tag{5.47}$$

Assume that the pseudo wavefunction is equal to the order parameter (up to an unimportant sign), $\hat{\psi}(\boldsymbol{\rho}) = \tilde{g}_\ell^2(\rho) e^{i\ell\theta}$. This is essentially the relation established by Gor'kov, and in reality it is an approximation at zero temperature [3, 18]. To be rigorous, we may include a factor of proportionality, but the prefactor will be fixed such that $\lim_{\rho\to\infty} \tilde{g}_\ell^2(\rho) = 1$ for simplicity in the simulations. For notational convenience in this section we introduce

$$f_\ell(\rho) \equiv \tilde{g}_\ell^2(\rho). \tag{5.48}$$

Inserting $\hat{\psi}(\boldsymbol{\rho}) = f_\ell(\rho)e^{i\ell\theta}$ into (5.47) gives the radial equation

$$f_\ell'' + \frac{1}{\rho}f_\ell' + \left(1 - \frac{\ell^2}{\rho^2}\right) f_\ell - f_\ell^3 = 0, \tag{5.49}$$

with the boundary value conditions

$$f_\ell(0) = 0 \quad \text{and} \quad f_\ell(\infty) = 1. \tag{5.50}$$

The boundary values ensure that the vortex core is located at $\rho = 0$, and that the fluid is homogeneous for large ρ. Some properties of f_ℓ close to the vortex core may be deduced analytically before proceeding with the numerical implementation. As a first approximation, we neglect the cubic term and (5.49) reduces to Bessel's equation. It means that f_ℓ in this limit is approximatively

$$f_\ell(\rho) \approx AJ_{|\ell|}(\rho) = \frac{A}{\Gamma(|\ell| + 1)} \left(\frac{\rho}{2}\right)^{|\ell|} + \mathcal{O}(\rho^{|\ell|+2}) \propto \rho^{|\ell|} \quad \text{for} \quad \rho \ll 1. \tag{5.51}$$

Above, we applied the small argument expansion of the Bessel function $J_{|\ell|}(\rho)$ (see Appendix C), and A is some constant that in principle may depend on ℓ. As ρ increases, the cubic term in (5.49) becomes important, and an asymptotic solution is of the form $f_\ell(\rho) = 1 + \mathcal{O}(\rho^{-2})$. Let it be mentioned that there are reasonable and analytic approximations to the solution, for example stated by A. Fetter in [31]. His discussion concerns $|\ell| = 1$ and the approximation reads

$$f_{|\ell|=1}(\rho) \approx \frac{\rho}{\sqrt{\rho^2 + \alpha^2}}, \tag{5.52}$$

with α a parameter that could be adjusted to give the correct slope of the curve for $\rho = 0$ by Taylor expansion. Another suitable approximation is mentioned by M. Tinkham [3],

$$f_{|\ell|=1}(\rho) \approx \tanh(\rho/\beta). \tag{5.53}$$

The constant β should be chosen equal to α. Both approximations have the small ρ expansion demanded by (5.51). The validity of these approximations in this context can be discussed after implementing (5.40) numerically, since a slight modification to the vortex profile will reveal how sensitive the solution $\tilde{u}(\rho)$ is to $f_\ell(\rho)$.

A numerical solution of the two-point boundary value problem in (5.49) and (5.50) was found and tabulated for $|\ell| \in \{1, 2, 3\}$ by M. Kawatra and R. Pathria in 1966 [32]. Since the tabulated values easily can be interpolated to give results of high precision, we do so instead of solving the problem again. Solving the equation again

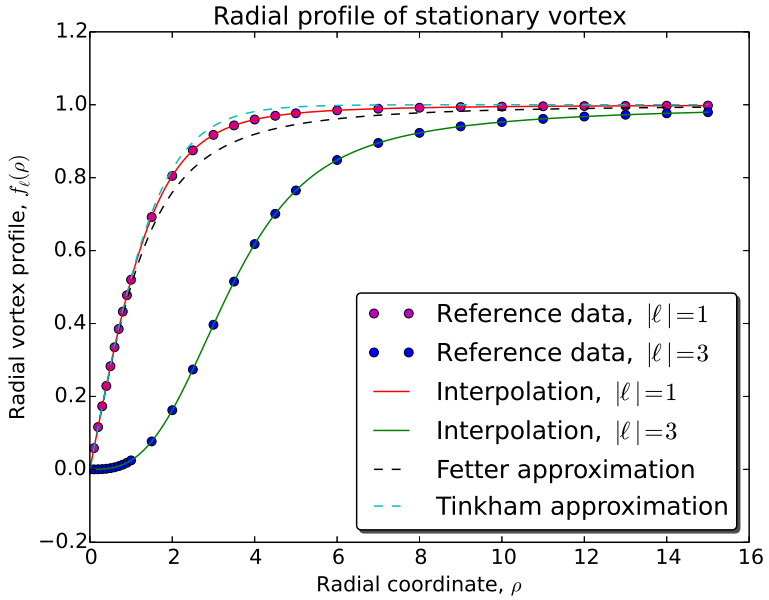

Figure 5.2: Radial profile of a stationary vortex, $f_\ell(\rho) = \tilde{g}_\ell^2(\rho)$, as a function of ρ for $|\ell| \in \{1, 3\}$. The reference data, taken from [32], are shown as coloured circles with cubic spline interpolated values plotted as continuous curves. The two approximations for $|\ell| = 1$ in equation (5.52) and (5.53) are shown for visual reference as dashed curves. The constants α and β were chosen to agree with the slope of the reference data at $\rho = 0$.

would not contribute with any new physical insights, and it involves instability subtleties that are time consuming and must be handled carefully.[5] In Figure 5.2 we have visualized the reference data from [32] for $|\ell| \in \{1, 3\}$ along with cubic spline interpolated curves. As visual reference, we have also shown the two approximations in (5.52) and (5.53). The interpolated values for f_ℓ are used in the next section where (5.40) is solved numerically.

5.5 Numerical Solutions and Discussion

Numerical results were obtained by application of Runge-Kutta method of 4th order for ordinary differential equations in a `Python` script. The basic `Python` script can be found attached in Appendix D.2. It makes use of a compact module called `ODESolver` that is described in [33]. We used a grid resolution of $N = 800$ in ρ. The solutions were plotted for $\rho \leq 15$ since they were typically localized within this value for our choice of parameters. Initial conditions were chosen to agree with the expected properties of the solution for small arguments. That is, when $\rho \ll 1$ and $f_\ell(\rho) \ll 1$, equation (5.42) and (5.43) predict that the solution inherits the properties of $J_{|\ell+1|/2}$. Therefore, with $\ell = -1$, we fixed the initial conditions to $\tilde{u}(0) = 1$ and $\mathrm{d}\tilde{u}/\mathrm{d}\rho|_{\rho=0} = 0$ since this agrees with the properties of J_0. With $\ell = -3$, we instead

[5] The basic strategy would be to apply a so-called *shooting algorithm* combined with an ordinary differential equation solver, for instance the Runge-Kutta 4th order method [27].

applied the conditions $\tilde{u}(0) = 0$ and $\mathrm{d}\tilde{u}/\mathrm{d}\rho|_{\rho=0} = 1$. Thereafter, the solutions were normalized according to (5.41).

5.5.1 Selected Results

A representative selection of solutions to (5.40) are shown in Figure 5.3. In Figure 5.3(a) we have used the spline interpolated values for $f_\ell(\rho)$. As both visual and numerical reference, a solution of the same equation with Fetter's vortex approximation is shown in Figure 5.3(b). The effect of increasing η can be seen in Figure 5.3(c). Finally, the solution obtained with increased vorticity, $\ell = -3$, is seen in Figure 5.3(d). Even though the solutions of the vortex-free equations, $f_\ell(\rho) = 0$, dictated by equation (5.42), are non-normalizable, they are plotted with green dashed curves for visual comparison (multiplied with the same normalization constant as the true solutions). This is mainly to see how the solutions have similar oscillatory behaviour and agree for small radial arguments. The presented solutions extend those presented by Gurarie and Radzihovsky [13] in the sense that they are not found in the limit of an infinitesimally small vortex core. As a suggestion to quantify the decay length of the solutions, we define a critical distance ρ_c, such that

$$|\tilde{u}(\rho > \rho_c)| \leq p \max_{\rho\in[0,\infty)} |\tilde{u}(\rho)| \quad \text{for some} \quad p \in (0, 1). \tag{5.54}$$

With $p = 0.01$, the critical distances were computed to $\rho_c = 8.1$ and $\rho_c = 8.2$ for the solutions in Figure 5.3(a) and 5.3(b) respectively. For the solutions in Figure 5.3(c) and 5.3(d), the values became $\rho_c = 6.5$ and $\rho_c = 10.3$ respectively. At the critical distances ρ_c, the vortex profile, $f_\ell(\rho_c)$, was typically less than 5% away from its asymptotic value. Hence, a single Majorana zero mode is localized within some small multiple of a from the vortex center, at least for low vorticity.

5.5.2 Discussion of the Results

The solutions in Figure 5.3(a) and 5.3(b) are strikingly similar. In fact, the computed normalization integrals typically differed in the third leading digit for the two solutions. This indicates that the solutions depend weakly on the detailed shape of $f_\ell(\rho)$. The approximative approach of determining the vortex profile does, therefore, not imply a great loss of precision in the solution. In any case, we are merely interested in illustrating basic properties of the Majorana modes and are not in the need of high precision solutions to achieve this.

Recall that ℓ, in addition to being the vorticity, according to equations (5.35) and (5.36) also plays the role as the angular momentum of the solution. More precicely, the spinor components $u(\boldsymbol{r})$ and $v(\boldsymbol{r})$ have angular momentum of $\pm\hbar(\ell + 1)/2$ respectively. In Figure 5.3(d) the effect of increased vorticity is seen. The nodes of the resulting Majorana zero mode are shifted radially outwards. A similar tendency is observed in other quantum systems. For instance, the radial wavefunctions in the hydrogen atom get nodes shifted further from the origin as the angular momentum

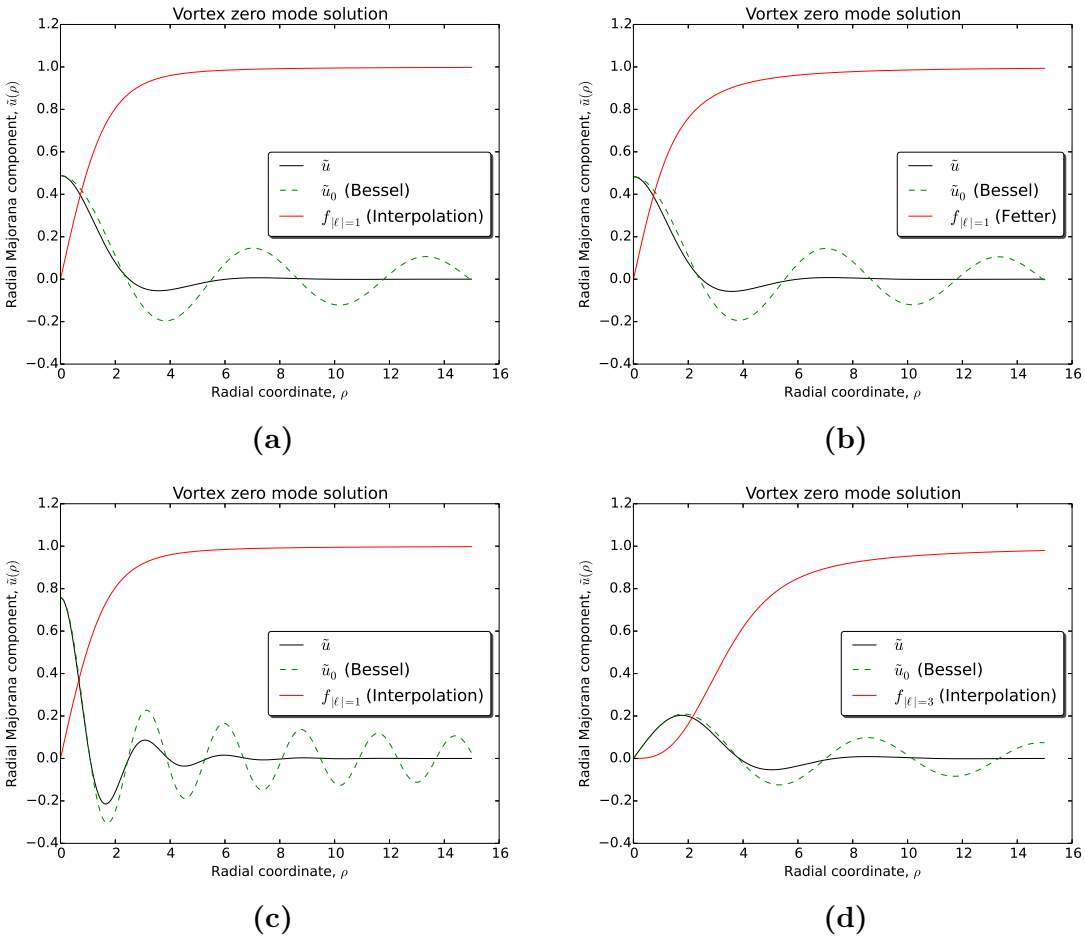

Figure 5.3: Radial Majorana zero mode component/wavefunction $\tilde{u}(\rho)$ as function of radial distance ρ, i.e. units of the Ginzburg-Landau coherence length. The solutions were normalized according to (5.41), and the radial vortex profile is shown in red. The green dashed curves, $\tilde{u}_0(\rho)$, are the non-normalizable solutions (Bessel functions) of the vortex-free equation, i.e. with $\Delta = 0$, multiplied with the same normalization constant as $\tilde{u}$. The parameters were fixed to **(a)** $|\ell| = 1$, $\eta = 1.0$, **(b)** $|\ell| = 1$, $\eta = 1.0$, **(c)** $|\ell| = 1$, $\eta = 5.0$, and **(d)** $|\ell| = 3$, $\eta = 1.0$. In all figures, except for **(b)**, the vortex profiles are cubic spline interpolations of the reference data from [32]. In **(b)** the profile is given by Fetter's approximation from equation (5.52).

is increased [17].

Peculiarly, and as noted earlier, both the solutions $\tilde{u}(\rho)$, and the vortex profile itself $f_\ell(\rho)$, are approximatively Bessel functions for small arguments,

$$\tilde{u}(\rho) \sim J_{\frac{|\ell+1|}{2}}(\sqrt{\eta}\rho) \quad \text{and} \quad f_\ell(\rho) \sim J_{|\ell|}(\rho) \quad \text{when} \quad \rho \ll 1. \tag{5.55}$$

The dependency on η here is roughly confirmed by the increased oscillation frequency seen for $\eta = 5.0$ in Figure 5.3(c). It is interesting that only an odd-vorticity vortex supports a single Majorana zero mode. One may qualitatively explain this by

imagining that every unit of vorticity is induced by a fundamental vortex of $|\ell| = 1$, with one Majorana zero mode bound to it. A vortex of vorticity n is thought of as being formed by adiabatically merging n fundamental vortices. Furthermore, if a pair of zero modes have great spatial overlap, they split in energy and hybridize to a finite $\pm E$ pair, i.e. one positive energy quasiparticle. In this picture, only odd ℓ vortices will be able to leave a zero mode in excess. One may question next why it seems that a single Majorana mode, which represent half a fermionic degree of freedom, appears isolated. Since we consider an infinite system, there is no outer boundary to host a second Majorana mode. This is perhaps artificial by construction since physical systems are finite. The consequence of having an outer boundary is explored in the next chapter.

Some of the weaknesses related to our calculations have already been commented on when discussing the vortex profile. One important simplification is the following. The vortex profile we used was taken from a reference that is based on vortex formations in superfluid Helium II (a certain phase of ^{4}He [16]), which is known to have conventional s-wave pairing. The model studied in this chapter, on the other hand, have p-wave pairing. The $\partial_x + i\partial_y$ term in $D(\boldsymbol{r}, \boldsymbol{r}')$ induces an intrinsic angular momentum in the order parameter. This is reflected in the fact that $\ell = -1$ is the lowest lying rotation state. Partly in ignorance, we have neglected how p-wave pairing affects the Ginzburg-Landau equation. Determining how to take this pairing properly into account is left here as an open problem that it would be interesting to study in future work.

5.6 Braiding Majorana Vortices

We suggest an argument that results in an exchange transformation in a system of several Majorana zero modes. The transformation has a non-Abelian representation as demonstrated in section 2.7. D. Ivanov minimalistically derived this transformation in 2001 [6]. His argument is compact and elegant, but the level of abstraction is high. As an alternative route, we consider a consequence of preserved fermion parity. I would like to thank Mats Horsdal for constructive aid in establishing this argument. Still, let it be emphasised that we merely propose this argument, and that the true physical content of it might turn out to be deficient.

Consider the expression (5.27) in the context of the solutions from the last sections. Inserting (5.35) with $m = (\ell + 1)/2$ and ℓ assumed odd yields the expansion

$$\gamma = \int \mathrm{d}^2 r \; \tilde{u}(r) \left(e^{-i\theta \frac{\ell+1}{2}} \psi^\dagger(\boldsymbol{r}) + e^{i\theta \frac{\ell+1}{2}} \psi(\boldsymbol{r}) \right). \tag{5.56}$$

Above, $\tilde{u}(r)$ is a radial solution like those from Figure 5.3. We imagine an idealized system of $2N$ vortices with positions $\{\boldsymbol{r}_j\}_{j=1}^{2N}$. Assume that the vortices at all times are separated spatially by a distance much larger than the coherence length,

$$|\boldsymbol{r}_i - \boldsymbol{r}_j| \gg a \quad \text{for} \quad i,j \in \{1,\ldots,2N\},\ i \neq j. \tag{5.57}$$

Thus, we neglect the *energy splitting* between the Majorana modes. In the next chapter we will return heavily to the consequences of energy splitting on an annulus geometry. For now, it suffices to mention that the splitting between two Majorana modes in vortices was treated as a tunnelling problem by M. Cheng et al. in [34]. The result presented there, roughly speaking, is an energy splitting exponentially small in the vortex separation. A cartoon picture of the situation is shown in Figure 5.4. Each vortex has exactly one Majorana zero mode, γ_j, bound to it,

$$\gamma_j = \int \mathrm{d}^2 r\, \tilde{u}_j(r - r_j) \left(e^{-i\theta\frac{\ell+1}{2}} \psi^\dagger(\boldsymbol{r} - \boldsymbol{r}_j) + e^{i\theta\frac{\ell+1}{2}} \psi(\boldsymbol{r} - \boldsymbol{r}_j) \right). \tag{5.58}$$

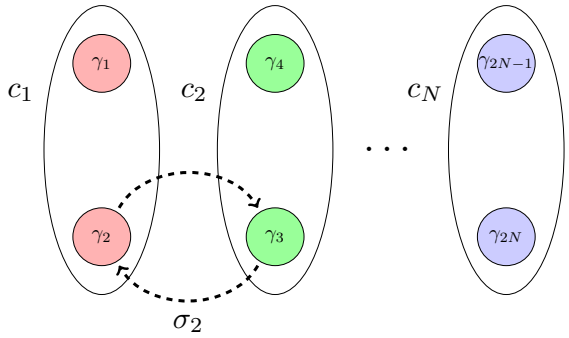

Figure 5.4: Illustration of $2N$ Majorana modes, thought of as localized in vortices, paired up to form N fermionic operators. The ellipses encapsulate the fermion operators. A basic exchange process is denoted by σ_2, and it exchanges γ_2 and γ_3 belonging to fermionic degrees of freedom c_1 and c_2 respectively.

The labels are chosen such that γ_j and γ_{j+1} are paired up to form a normal fermion operator. This is analogous to equation (4.2), and it may be thought of as choice of basis,

$$c_j = \frac{1}{2}(\gamma_{2j-1} + i\gamma_{2j}) \quad \text{with} \quad \{\gamma_i, \gamma_j\} = 2\delta_{i,j} \quad \text{and} \quad [H, \gamma_j] = 0. \tag{5.59}$$

The ground state will have a degeneracy of 2^N. This is because the fermion occupation numbers can take two values for each pair of Majoranas. In terms of γ_j operators, the occupation number operators are

$$n_j = c_j^\dagger c_j = \frac{1}{2}(1 + i\gamma_{2j-1}\gamma_{2j}) \ \forall\, j \in \{1,\ldots,N\}. \tag{5.60}$$

An immediate consequence is that any two occupation operators commute, and integer powers of the operators are trivial,

$$[n_i, n_j] = 0 \quad \text{and} \quad n_j^m = n_j \ \forall\, m \in \mathbb{N}. \tag{5.61}$$

The mean field Hamiltonians we have been considering conserve total fermion parity. In other words, they only contain quadratic terms (schematically) like $\psi^\dagger\psi$, $\psi\psi$ and $\psi^\dagger\psi^\dagger$. Let P denote the total fermion parity operator of the system. Up to an overall sign, this operator is represented to have the eigenvalues $+1$ if $\sum_j n_j$ is even and -1 if $\sum_j n_j$ is odd, as in equation (3.37). Thus,

$$[H, P] = 0 \quad \text{with} \quad P = e^{i\pi \sum_{j=1}^{N} n_j}. \tag{5.62}$$

This operator becomes particularly simple when expressed in terms of Majorana operators, and it constitutes the core ingredient of this argument. We apply the *Campbell-Baker-Hausdorff formula* to the exponential operator P. For the sake of completeness, the relation for non-commuting operators A and B reads (from [23])

$$\exp(A)\exp(B) = \exp\left(A + B + \frac{1}{2}[A, B] + \frac{1}{12}\Big([A, [A, B]] + [B, [B, A]] \Big) + \dots \right), \tag{5.63}$$

with dots indicating higher order commutators of A and B. Applying it to P in (5.62), while using (5.61), yields a chain of simplifications,

$$\begin{aligned} P &= e^{i\pi \sum_{j=1}^{N} n_j} \\ &= \prod_{j=1}^{N} \sum_{m=0}^{\infty} \frac{(i\pi)^m}{m!} n_j^m \\ &= \prod_{j=1}^{N} \left(1 + n_j \sum_{m=1}^{\infty} \frac{(i\pi)^m}{m!} \right) \\ &= \prod_{j=1}^{N} (1 - 2n_j) \\ &= (-i)^N \prod_{j=1}^{N} \gamma_{2j-1}\gamma_{2j}. \end{aligned} \tag{5.64}$$

We emphasise that the last expression is a product of anticommuting operators. Assume next that Majorana γ_k and γ_l are exchanged adiabatically in a clockwise manner without encapsulating any other vortices, as exemplified in Figure 5.4. If the system prior to the change is in the ground state, the Adiabatic Theorem (see Appendix B) ensures that it will remain in the 2^N-dimensional ground state manifold during the exchange. As the vortex in position $\boldsymbol{r}_k$ is moved to position $\boldsymbol{r}_l$, the Majorana operator can at most pick up a sign in order to remain real ($\gamma^\dagger = \gamma$). The same applies for the vortex in position $\boldsymbol{r}_l$ being moved to $\boldsymbol{r}_k$,

$$\gamma_k \mapsto e^{i\alpha}\gamma_l \quad \text{and} \quad \gamma_l \mapsto e^{i\beta}\gamma_k, \tag{5.65}$$

with α and β restricted to being integer multiples of π. The exchange have the following effect on the parity operator:

$$\begin{aligned} P = (-i)^N \gamma_1\gamma_2\cdots\gamma_k\cdots\gamma_l\cdots\gamma_{2N} &\mapsto e^{i\alpha}e^{i\beta}(-i)^N\gamma_1\gamma_2\cdots\gamma_l\cdots\gamma_k\cdots\gamma_{2N} \\ &= -e^{i\alpha}e^{i\beta}(-i)^N\gamma_1\gamma_2\cdots\gamma_k\cdots\gamma_l\cdots\gamma_{2N} \\ &= -e^{i\alpha}e^{i\beta}P. \end{aligned} \tag{5.66}$$

The sign change above occurs as we apply anticommutator relations an odd number of times, independent of $|k-l|$, to reconstruct the expression for P. The phases α and β are dependent since we demand P to be invariant. It means that

$$e^{i\alpha}e^{i\beta} = -1. \tag{5.67}$$

Hence, we have arrived at the conclusion that the operators γ_k and γ_l must pick up opposite signs. The overall choice of sign change is a gauge choice. We take $\gamma_j \mapsto \gamma_{j+1}$ and $\gamma_{j+1} \mapsto -\gamma_j$ for the clockwise exchange of neighbouring pairs. The operators not taking part in the exchange, γ_j for $j \notin \{i, i+1\}$, are assumed to remain unaffected, which is a locality assumption. The transformation rule for exchange of neighbouring Majorana vortices may therefore be summarized as

$$\sigma_i : \begin{cases} \gamma_i \mapsto \gamma_{i+1} & \\ \gamma_{i+1} \mapsto -\gamma_i & \\ \gamma_j \mapsto \gamma_j & \text{if } \ j \notin \{i, i+1\} \end{cases}, \tag{5.68}$$

which is the same transformation rule as presented by Ivanov [6]. In the introductory chapter, specifically in section 2.7, we demonstrated how a representation of the transformation rule in (5.68) resulted in non-Abelian exchange statistics of the Majorana vortices. We therefore close our derivation at this point and summarize this chapter.

5.6.1 Reflections and Concluding Remarks

One of the limitations in the argument above is that it does not add any great insights about the actual exhange process of vortices. We merely arrive at the same conclusion as Ivanov by considering conservation of total fermion parity. The exchange operator in (5.68) is the result of a finite, discrete process. It would have been more satisfactory to see this transformation rule as the result of a continuous exchange calculation. However, how to set up this calculation properly is not clear at the time of writing. Let it be mentioned that an exhaustive calculation was proposed in a network of elementary Kitaev chains and T-shaped junctions by J. Alicea et al. some years ago [7]. Their calculation supports the non-Abelian transformation described by Ivanov, despite considering a construction of connected one-dimensional systems. Understanding these exchange processes better and on a more elementary level is something that would be interesting to study in future work.

This chapter was opened with quite general considerations of the $p+ip$ model and a formal derivation of the BdG equations. Thereafter, the discussion was specialized in the sense that we searched for Majorana zero mode solutions with an order parameter describing a symmetric vortex. We argued how single valued fermion operators led to the conclusion that only vortices of odd vorticity support a Majorana zero mode. With a vortex profile in accordance with a minimal Ginzburg-Landau description, we solved the differential equation numerically. The simulations demonstrated that the coherence length, a, is the scale over which the resulting Majorana mode is localized. In a system of several well separated vortices – each supporting one Majorana mode – we suggested an argument that resulted in an exchange transformation with a non-Abelian representation.

Chapter 6

Edge Modes in the $p + ip$ Model

In this chapter we study the $p+ip$ model on an annulus, motivated by Jason Alicea's brief presentation in [11]. We seek a more complete and detailed understanding of the edge modes. Specifically, we focus on how they split in energy and how the splitting depends on the separation between the circular boundaries. Our approach to calculating the energy splitting is not based on any reference. Still, we harvest inspiration from [34, 35], of which we also compare our results to. The philosophy of our approach is to approximate the ground state with a trial solution that consists of edge modes from systems having only an inner and an outer edge respectively. This is thought to be a good approximation when the boundary separation becomes large. Mats Horsdal has participated with very useful advices in the calculation procedure. Finally, the BdG equations are formulated as an eigenvalue problem by discretizing derivatives. We solve the eigenvalue problem numerically using `C++`, and the solutions are compared to analytical results for verification and comparison. The Hamiltonian,

$$H = \int \mathrm{d}^2 r\, \psi^\dagger(\boldsymbol{r}) \left(-\frac{\hbar^2}{2m}\nabla^2 - \mu \right) \psi(\boldsymbol{r}) + \frac{1}{2} \int \mathrm{d}^2 r\, \mathrm{d}^2 r' \left(\psi^\dagger(\boldsymbol{r}) D(\boldsymbol{r}, \boldsymbol{r}') \psi^\dagger(\boldsymbol{r}') + \mathrm{h.c.} \right), \tag{6.1}$$

has the corresponding BdG equations

$$\begin{pmatrix} -\frac{\hbar^2}{2m}\nabla^2 - \mu & \frac{1}{2}\{\Delta(\boldsymbol{r}), \partial_{z^*}\} \\ -\frac{1}{2}\{\Delta^*(\boldsymbol{r}), \partial_z\} & \frac{\hbar^2}{2m}\nabla^2 + \mu \end{pmatrix} \begin{pmatrix} u_n(\boldsymbol{r}) \\ v_n(\boldsymbol{r}) \end{pmatrix} = E_n \begin{pmatrix} u_n(\boldsymbol{r}) \\ v_n(\boldsymbol{r}) \end{pmatrix}. \tag{6.2}$$

Recall the operator $\partial_{z^*} = e^{i\theta}(\partial_r + \frac{i}{r}\partial_\theta)$ and that $\Delta(\boldsymbol{r})$ denotes the superconducting order parameter. The coefficients $u(\boldsymbol{r})$ and $v(\boldsymbol{r})$ are complex weights that form quasiparticle operators according to

$$\Gamma_n = \int \mathrm{d}^2 r \Big(u_n^*(\boldsymbol{r})\psi(\boldsymbol{r}) + v_n^*(\boldsymbol{r})\psi^\dagger(\boldsymbol{r}) \Big). \tag{6.3}$$

The quasiparticle operators are assumed to diagonalize H,

$$H = E_\Omega + \sum_n E_n \Gamma_n^\dagger \Gamma_n, \tag{6.4}$$

with $E_n > 0$.

6.1 Formulating the Problem

The annulus geometry $\mathcal{D}$, depicted in Figure 6.1, defines the topological domain that we will restrict ourselves to. In polar coordinates this domain is

$$\mathcal{D} = \Big\{ (r, \theta) \mid r \in [R_1, R_2], \;\; \theta \in [0, 2\pi) \Big\}. \tag{6.5}$$

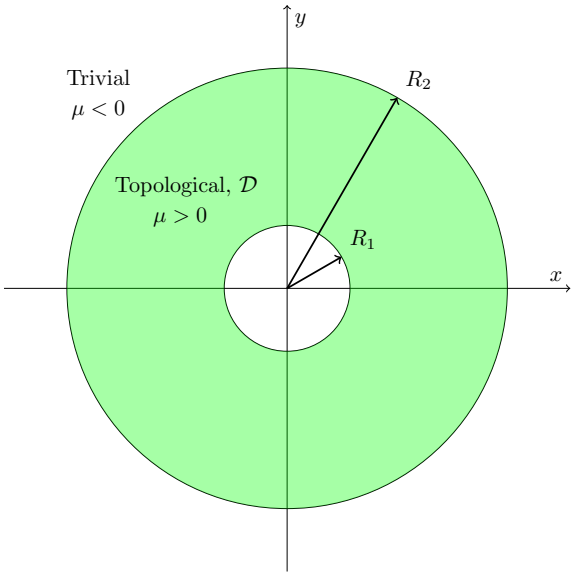

Figure 6.1: Annulus geometry $\mathcal{D}$. It is defined to be a region in $\mathbb{R}^2$ within two concentric rings of radii R_1 and R_2. In this region $\mu > 0$ is constant and the order parameter is constant in absolute value.

One simplification of Alicea's approach is to neglect the kinetic term containing ∇^2 in the Hamiltonian, which allows him to find simple analytical solutions for systems that have only an inner and an outer boundary [11]. It is therefore of interest to see the consequences of including the kinetic term and to perform a numerical diagonalization of the system to find exact solutions. In contrast to the system in the previous chapter, having an outer boundary is expected to result in the appearance of an additional Majorana mode. Numerically, we will apply *Dirichlet boundary conditions*,

$$u_n(R_1, \theta) = u_n(R_2, \theta) = v_n(R_1, \theta) = v_n(R_2, \theta) = 0. \tag{6.6}$$

In other words, the wavefunctions vanish identically outside $\mathcal{D}$. Formally, this is achieved by letting $\mu \to -\infty$ outside the topological disk. Analytically, however,

this limit will not be taken immediately, but we comment on this throughout the next section. We formulate the BdG equations as coupled differential equations and make them dimensionless. Assume also that the order parameter takes the form

$$\Delta(\boldsymbol{r}) = \Delta_0 e^{i\ell\theta + i\pi}, \tag{6.7}$$

with Δ_0 constant and $\ell \in \mathbb{Z}$ the vorticity. Again, an overall sign, which simply means a redefinition of the order parameter, is included for convenience. One may think of the angular momentum as being induced by a magnetic flux threading the center (trivial) part of the disk, inducing a vortex. In the topological region, $\mathcal{D}$, the radial vortex profile has reached its asymptotic value Δ_0. This is underpinned by assuming that $R_1, R_2 \gg a$, with a the Ginzburg-Landau coherence length. In the previous chapter we stressed that only odd values of ℓ supported the assumption of single valued fermion fields. Thus, ℓ is assumed to be odd at this point. We apply the same separation of variables for $u_n(\boldsymbol{r})$ and $v_n(\boldsymbol{r})$ as before,

$$u_n(\boldsymbol{r}) = \tilde{u}_n(r) e^{i\theta\frac{\ell+1}{2}} \quad \text{and} \quad v_n(\boldsymbol{r}) = \tilde{v}_n(r) e^{-i\theta\frac{\ell+1}{2}}, \tag{6.8}$$

such that the radial BdG equations are

$$\begin{aligned} -\frac{\hbar^2}{2m}\left(\frac{\mathrm{d}^2}{\mathrm{d}r^2} + \frac{1}{r}\frac{\mathrm{d}}{\mathrm{d}r} - \frac{1}{r^2}\left(\frac{\ell+1}{2}\right)^2\right)\tilde{u}_n(r) - \mu\tilde{u}_n(r) \\ - \Delta_0\left(\frac{\mathrm{d}}{\mathrm{d}r} + \frac{1}{2r}\right)\tilde{v}_n(r) = E_n\tilde{u}_n(r), \\ \frac{\hbar^2}{2m}\left(\frac{\mathrm{d}^2}{\mathrm{d}r^2} + \frac{1}{r}\frac{\mathrm{d}}{\mathrm{d}r} - \frac{1}{r^2}\left(\frac{\ell+1}{2}\right)^2\right)\tilde{v}_n(r) + \mu\tilde{v}_n(r) \\ + \Delta_0\left(\frac{\mathrm{d}}{\mathrm{d}r} + \frac{1}{2r}\right)\tilde{u}_n(r) = E_n\tilde{v}_n(r). \end{aligned} \tag{6.9}$$

The equations are made dimensionless by introducing the variables

$$\rho \equiv \frac{r}{a}, \quad \xi \equiv \frac{\hbar^2}{2m}, \quad \eta \equiv \frac{a^2}{\xi}\mu, \quad \delta_0 \equiv \frac{a}{\xi}\Delta_0, \quad \text{and} \quad \varepsilon_n \equiv \frac{a^2}{\xi}E_n. \tag{6.10}$$

The coupled equations in (6.9) become

$$\begin{aligned} -\left(\frac{\mathrm{d}^2}{\mathrm{d}\rho^2} + \frac{1}{\rho}\frac{\mathrm{d}}{\mathrm{d}\rho} - \frac{1}{\rho^2}\left(\frac{\ell+1}{2}\right)^2 + \eta\right)\tilde{u}_n(\rho) - \delta_0\left(\frac{\mathrm{d}}{\mathrm{d}\rho} + \frac{1}{2\rho}\right)\tilde{v}_n(\rho) = \varepsilon_n\tilde{u}_n(\rho), \\ \left(\frac{\mathrm{d}^2}{\mathrm{d}\rho^2} + \frac{1}{\rho}\frac{\mathrm{d}}{\mathrm{d}\rho} - \frac{1}{\rho^2}\left(\frac{\ell+1}{2}\right)^2 + \eta\right)\tilde{v}_n(\rho) + \delta_0\left(\frac{\mathrm{d}}{\mathrm{d}\rho} + \frac{1}{2\rho}\right)\tilde{u}_n(\rho) = \varepsilon_n\tilde{v}_n(\rho). \end{aligned} \tag{6.11}$$

The solutions may be represented by two-component spinors as mentioned briefly in section 5.2,

$$\boldsymbol{\phi}_n \equiv \begin{pmatrix} \tilde{u}_n(\rho) e^{i\theta\frac{\ell+1}{2}} \\ \tilde{v}_n(\rho) e^{-i\theta\frac{\ell+1}{2}} \end{pmatrix}. \tag{6.12}$$

These spinors are normalized according to

$$\langle \boldsymbol{\phi}_n | \boldsymbol{\phi}_n \rangle \equiv \int \mathrm{d}^2\rho\, \boldsymbol{\phi}_n^\dagger \boldsymbol{\phi}_n = 2\pi \int_0^\infty \mathrm{d}\rho\, \rho \left(|\tilde{u}_n|^2 + |\tilde{v}_n|^2 \right) = 1. \tag{6.13}$$

The compact notation

$$\nabla^2 \equiv \frac{\mathrm{d}^2}{\mathrm{d}\rho^2} + \frac{1}{\rho}\frac{\mathrm{d}}{\mathrm{d}\rho} - \frac{1}{\rho^2}\left(\frac{\ell+1}{2}\right)^2 \quad \text{and} \quad \partial \equiv \frac{\mathrm{d}}{\mathrm{d}\rho} + \frac{1}{2\rho}, \tag{6.14}$$

will sometimes be applied. The BdG Hamiltonian acting on spinors, as in equation (6.12), may therefore be expressed as

$$\mathcal{H} = \begin{pmatrix} -\nabla^2 - \eta & -\delta_0 \partial \\ \delta_0 \partial & \nabla^2 + \eta \end{pmatrix}. \tag{6.15}$$

6.2 The Energy Splitting

We find an approximative expression for the ground state spinor of the system in Figure 6.1. This is done with associations of the double well tunnelling problem known from quantum mechanics [17]. We calculate approximative and asymptotic zero energy spinors of the two systems containing only one edge each. A linear combination of the spinors is used as a ground state trial spinor for the two-edged system. The resulting energy becomes a function of the boundary separation $\Delta\rho = \rho_2 - \rho_1$. We stress that this calculation is done with the aim of obtaining a simple closed form expression of the energy splitting. The procedure will reveal useful insights and predictions that later can be compared to numerical results in the correct limit.

6.2.1 A General Consideration

Consider a one-edged system $\mathcal{H}_1$, as in (6.15), with a chemical potential described by a step function that separates a trivial region, $\eta_0 < 0$, and a topological region, $\eta_T > (\delta_0/2)^2 > 0$,

$$\eta_1(\rho) = \begin{cases} \eta_0 & \text{if } \rho \in [0, \rho_1) \\ \eta_T & \text{if } \rho \in [\rho_1, \infty) \end{cases}. \tag{6.16}$$

Note that a topological region is in the $p+ip$ model characterized by $\eta > 0$, but the additional assumption of $\eta > (\delta_0/2)^2$ will turn out to imply spatial oscillations in the wavefunctions. The consequences of this will be commented on in the discussion. A similar system with an outer edge at ρ_2 is described by $\mathcal{H}_2$ and the chemical potential

$$\eta_2(\rho) = \begin{cases} \eta_T & \text{if } \rho \in [0, \rho_2] \\ \eta_0 & \text{if } \rho \in (\rho_2, \infty) \end{cases} . \tag{6.17}$$

Assume further that the spinors

$$\boldsymbol{\phi}_1 = \begin{pmatrix} \tilde{u}_1 e^{i\theta(\ell+1)/2} \\ \tilde{u}_1^* e^{-i\theta(\ell+1)/2} \end{pmatrix} \quad \text{and} \quad \boldsymbol{\phi}_2 = \begin{pmatrix} \tilde{u}_2 e^{i\theta(\ell+1)/2} \\ \tilde{u}_2^* e^{-i\theta(\ell+1)/2} \end{pmatrix} \tag{6.18}$$

are zero modes of $\mathcal{H}_1$ and $\mathcal{H}_2$ respectively,

$$\mathcal{H}_1 \boldsymbol{\phi}_1 = \mathcal{H}_2 \boldsymbol{\phi}_2 = 0. \tag{6.19}$$

The situation is depicted qualitatively in Figure 6.2. Details related to this general picture are progressively found throughout the next few subsections. The two-edged system, $\mathcal{H}$, is described by the combined chemical potential

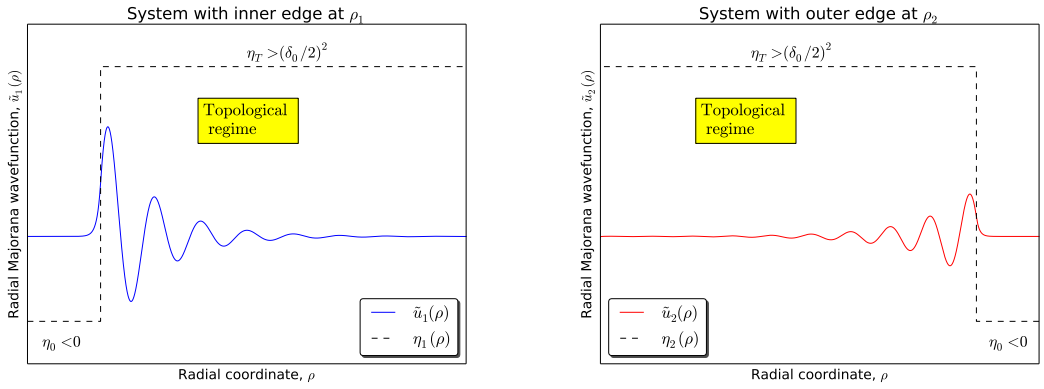

(a) **(b)**

Figure 6.2: A qualitative picture of Majorana zero modes located on the circular boundaries of an annulus. **(a)** System with an inner edge at ρ_1 and a chemical potential described by the step function $\eta_1(\rho)$ as in equation (6.16). **(b)** System with an outer edge at ρ_2 described by the step function $\eta_2(\rho)$ from equation (6.17).

$$\eta(\rho) = \begin{cases} \eta_0 & \text{if } \rho \in [0, \rho_1) \\ \eta_T & \text{if } \rho \in [\rho_1, \rho_2] \\ \eta_0 & \text{if } \rho \in (\rho_2, \infty) \end{cases} . \tag{6.20}$$

The full system can be expressed compactly in terms of the single-edged Hamiltonians,

$$\begin{aligned}\mathcal{H} &= \mathcal{H}_1 + \begin{pmatrix} \eta_T - \eta_0 & 0 \\ 0 & -(\eta_T - \eta_0) \end{pmatrix} \Theta(\rho - \rho_2) \\ &= \mathcal{H}_1 + \Delta\eta\, \Theta(\rho - \rho_2)\sigma_z \\ &= \mathcal{H}_2 + \Delta\eta\, \Theta(\rho_1 - \rho)\sigma_z,\end{aligned} \tag{6.21}$$

with σ_z the third Pauli matrix, $\Delta\eta \equiv \eta_T - \eta_0$, and $\Theta(\rho)$ the Heaviside function. We make ansatzes for trial spinors $\boldsymbol{\phi}_\pm$ that serve as candidates for the ground state spinor of the full system. At the moment, these ansatzes are merely postulated. *A posteriori*, it will turn out that the spinors are diagonal in the energy basis. Let

$$\boldsymbol{\phi}_\pm = \frac{1}{\sqrt{2}} \left(\boldsymbol{\phi}_1 \pm i\boldsymbol{\phi}_2 \right), \tag{6.22}$$

assuming that both $\boldsymbol{\phi}_1$ and $\boldsymbol{\phi}_2$ are normalized. One might object that overlap integrals, such as $\langle \boldsymbol{\phi}_1 | \boldsymbol{\phi}_2 \rangle$, contradict the normalization in $\boldsymbol{\phi}_\pm$. However, it is expected that $\boldsymbol{\phi}_1$ and $\boldsymbol{\phi}_2$ are (exponentially) localized around ρ_1 and ρ_2 respectively [11]. Therefore, if $\rho_2 \gg \rho_1$ the overlap integrals will be highly suppressed. The trial spinors are used to find a general expression for $E_\pm = \langle \boldsymbol{\phi}_\pm | \mathcal{H} | \boldsymbol{\phi}_\pm \rangle$. First, observe that several terms vanish identically. We expand $E_\pm$,

$$\begin{aligned}E_\pm &= \langle \boldsymbol{\phi}_\pm | \mathcal{H} | \boldsymbol{\phi}_\pm \rangle \\ &= \frac{1}{2} \langle \boldsymbol{\phi}_1 | \mathcal{H} | \boldsymbol{\phi}_1 \rangle + \frac{1}{2} \langle \boldsymbol{\phi}_2 | \mathcal{H} | \boldsymbol{\phi}_2 \rangle \pm \frac{i}{2} \langle \boldsymbol{\phi}_1 | \mathcal{H} | \boldsymbol{\phi}_2 \rangle \mp \frac{i}{2} \langle \boldsymbol{\phi}_2 | \mathcal{H} | \boldsymbol{\phi}_1 \rangle \\ &= \pm\frac{i}{2}\Delta\eta\ \langle \boldsymbol{\phi}_1 | \Theta(\rho_1 - \rho)\sigma_z | \boldsymbol{\phi}_2 \rangle \mp \frac{i}{2}\Delta\eta\ \langle \boldsymbol{\phi}_2 | \Theta(\rho - \rho_2)\sigma_z | \boldsymbol{\phi}_1 \rangle \\ &= \pm\frac{i}{2}\Delta\eta \int_0^{2\pi} \mathrm{d}\theta \int_0^{\rho_1} \mathrm{d}\rho\, \rho\, \boldsymbol{\phi}_1^\dagger \sigma_z \boldsymbol{\phi}_2 \mp \frac{i}{2}\Delta\eta \int_0^{2\pi} \mathrm{d}\theta \int_{\rho_2}^{\infty} \mathrm{d}\rho\, \rho\, \boldsymbol{\phi}_2^\dagger \sigma_z \boldsymbol{\phi}_1 \\ &= \pm\pi i \Delta\eta \int_0^{\rho_1} \mathrm{d}\rho\, \rho \left(\tilde{u}_1^* \tilde{u}_2 - \tilde{u}_1 \tilde{u}_2^* \right) \mp \pi i \Delta\eta \int_{\rho_2}^{\infty} \mathrm{d}\rho\, \rho \left(\tilde{u}_1 \tilde{u}_2^* - \tilde{u}_1^* \tilde{u}_2 \right).\end{aligned} \tag{6.23}$$

The reason why the diagonal terms vanish is seen by inserting the appropriate expression from (6.21) while using (6.19). For instance,

$$\begin{aligned}\langle \boldsymbol{\phi}_1 | \mathcal{H} | \boldsymbol{\phi}_1 \rangle &= \langle \boldsymbol{\phi}_1 | \mathcal{H}_1 + \Delta\eta\, \Theta(\rho - \rho_2)\sigma_z | \boldsymbol{\phi}_1 \rangle \\ &= \Delta\eta \int_0^{2\pi} \mathrm{d}\theta \int_{\rho_2}^{\infty} \mathrm{d}\rho\, \rho\, \boldsymbol{\phi}_1^\dagger \sigma_z \boldsymbol{\phi}_1 \\ &= 2\pi\Delta\eta \int_{\rho_2}^{\infty} \mathrm{d}\rho\, \rho \left(|\tilde{u}_1|^2 - |\tilde{u}_1|^2 \right) = 0.\end{aligned} \tag{6.24}$$

Hence, calculating $E_+ = -E_-$ is reduced to two radial integrals in (6.23). It is interesting that both integrals run over trivial regions where $\eta = \eta_0 < 0$. When

actually calculating these integrals later, we do it in the limit $|\eta_0| \gg \eta_T > (\delta_0/2)^2$ and still get a finite contribution independent of η_0. To insist on calculating the splitting before taking this limit $\eta_0 \to -\infty$ might seem counter intuitive, but it actually turned out to be crucial while working with this problem. The next task is to find approximations for the single-edged spinors described by $\tilde{u}_1$ and $\tilde{u}_2$. Note further that since $E_+ = -E_-$, the two spinors $\boldsymbol{\phi}_\pm$ are particle-hole symmetric states.

6.2.2 Finding the Spinors

The general criterion for a Majorana mode is that $\Gamma^\dagger = \Gamma$. By looking back at (6.3), it means that $\tilde{u} = \tilde{v}^*$ after the separation of variables. Without making any further assumptions on the realness of $\tilde{u}$ or $\tilde{v}$, we are free to make the separation

$$\tilde{u}(\rho) = f(\rho) + ig(\rho), \tag{6.25}$$

with both f and g being real functions. Inserting this into (6.11) leads to two real equations (the notation from (6.14) is used),

$$\Big(\nabla^2 + \eta + \delta_0\partial\Big) f(\rho) = 0 \quad \text{and} \quad \Big(\nabla^2 + \eta - \delta_0\partial\Big) g(\rho) = 0. \tag{6.26}$$

These equations are made more familiar by introducing

$$f(\rho) = \chi(\rho) e^{-\frac{\delta_0}{2}\rho} \quad \text{and} \quad g(\rho) = \chi(\rho) e^{+\frac{\delta_0}{2}\rho}. \tag{6.27}$$

Both equations in (6.26) imply Bessel's equation for $\chi(\rho)$,

$$\frac{\mathrm{d}^2\chi}{\mathrm{d}\rho^2} + \frac{1}{\rho}\frac{\mathrm{d}\chi}{\mathrm{d}\rho} + \left(\eta - \left(\frac{\delta_0}{2}\right)^2 - \frac{1}{\rho^2}\left(\frac{\ell+1}{2}\right)^2\right)\chi = 0. \tag{6.28}$$

The reader is referred to Appendix C for details about the properties of the solutions. Assume first that $\eta > (\delta_0/2)^2$, and define the frequency

$$\omega \equiv \sqrt{\eta - (\delta_0/2)^2}. \tag{6.29}$$

A general solution to (6.28) is in this case a linear combination of Bessel functions,

$$\chi(\rho) = a_1 J_{\frac{|\ell+1|}{2}}(\omega\rho) + a_2 Y_{\frac{|\ell+1|}{2}}(\omega\rho), \tag{6.30}$$

with a_1 and a_2 integration constants. If instead $\eta < (\delta_0/2)^2$, we define

$$\lambda \equiv \sqrt{(\delta_0/2)^2 - \eta}, \tag{6.31}$$

and the general solution of (6.28) is a linear combination of *hyperbolic* Bessel functions,

$$\chi(\rho) = b_1 I_{\frac{|\ell+1|}{2}}(\lambda\rho) + b_2 K_{\frac{|\ell+1|}{2}}(\lambda\rho), \tag{6.32}$$

with b_1 and b_2 integration constants. In order to do any predictive calculation analytically, we will compute everything that follows in the limit $\rho \gg 1/\omega, 1/\lambda$. Hence, instead of using the general solutions in (6.30) and (6.32), we may use a solution basis spanned by their asymptotic forms. This is the main simplification of this calculation. The asymptotic forms of the Bessel functions and the hyperbolic Bessel functions are (see Appendix C):

$$\begin{aligned}
J_n(x) &\sim \sqrt{\frac{2}{\pi x}} \cos\left(x - \frac{2n+1}{4}\pi\right)\Big(1 + \mathcal{O}(x^{-1})\Big),\\
Y_n(x) &\sim \sqrt{\frac{2}{\pi x}} \sin\left(x - \frac{2n+1}{4}\pi\right)\Big(1 + \mathcal{O}(x^{-1})\Big),\\
I_n(x) &\sim \frac{1}{\sqrt{2\pi x}} e^{x}\Big(1 + \mathcal{O}(x^{-1})\Big),\\
K_n(x) &\sim \sqrt{\frac{\pi}{2x}} e^{-x}\Big(1 + \mathcal{O}(x^{-1})\Big).
\end{aligned} \tag{6.33}$$

In this asymptotic limit the ℓ-dependent term in (6.28) is suppressed since it falls off with ρ as $\mathcal{O}(\rho^{-2})$. It will lead to approximative solutions that do not depend on ℓ, which clearly is a simplification. We return to this observation in the final discussion. Observe also that all leading order terms in the asymptotic expansion above have the dependency on $1/\sqrt{x}$ in common. We therefore separate this factor to make the next sections simpler; this factor will be identically cancelled by the polar coordinate Jacobian in the integrals from (6.23). Let

$$f(\rho) = F(\rho)/\sqrt{\rho} \quad \text{and} \quad g(\rho) = G(\rho)/\sqrt{\rho}. \tag{6.34}$$

Thus, if $\eta > (\delta_0/2)^2$, we use a basis spanning the asymptotic solutions,

$$\begin{aligned}
F(\rho) &= \left[A_1 \cos(\omega\rho) + A_2 \sin(\omega\rho)\right] e^{-\frac{\delta_0}{2}\rho},\\
G(\rho) &= \left[B_1 \cos(\omega\rho) + B_2 \sin(\omega\rho)\right] e^{+\frac{\delta_0}{2}\rho}.
\end{aligned} \tag{6.35}$$

On the other hand, if $\eta < (\delta_0/2)^2$, we use

$$\begin{aligned}
F(\rho) &= C_1 e^{(\lambda - \frac{\delta_0}{2})\rho} + C_2 e^{(-\lambda - \frac{\delta_0}{2})\rho},\\
G(\rho) &= D_1 e^{(\lambda + \frac{\delta_0}{2})\rho} + D_2 e^{(-\lambda + \frac{\delta_0}{2})\rho},
\end{aligned} \tag{6.36}$$

where $A_1, \ldots, D_2$ are integration constants. The asymptotic solutions above may now be exploited to calculate the spinor $\boldsymbol{\phi}_1$ ($\boldsymbol{\phi}_2$) corresponding to $\mathcal{H}_1$ ($\mathcal{H}_2$). This is done by patching together solutions on each side of the respective steps in chemical potential. Extra subscripts on the constants from (6.29) and (6.31) will be added, ω_T and λ_0, to remind ourselves on being in the topological or trivial regimes respectively.

6.2.3 Inner Edge at ρ_1

We calculate the spinor $\boldsymbol{\phi}_1$ belonging to $\mathcal{H}_1$ with $\eta_1(\rho)$ as in equation (6.16). The real solution, F, is denoted by F_{I} when $\rho < \rho_1$ and F_{II} when $\rho > \rho_1$. Analogously, the imaginary solution is called G_{I} for $\rho < \rho_1$ and G_{II} for $\rho > \rho_2$. The functions are patched together at ρ_1 by making them continuous and differentiable,

$$F_{\mathrm{I}}(\rho_1) = F_{\mathrm{II}}(\rho_1) \quad \text{and} \quad \frac{\mathrm{d}F_{\mathrm{I}}}{\mathrm{d}\rho}(\rho_1) = \frac{\mathrm{d}F_{\mathrm{II}}}{\mathrm{d}\rho}(\rho_1), \tag{6.37}$$

and similarly for G_{I} and G_{II}. The function G_{II} is given by equation (6.35). However, this function is exponentially increasing in ρ, and we are forced to put $B_1 = B_2 = 0$ in order to have $\lim_{\rho\to\infty} G_{\mathrm{II}}(\rho) = 0$. Thus, the solution has only a real component for $\rho > \rho_1$ and we may conclude that $G_{\mathrm{I}} = 0$. We take the real part of the solution to be localized around ρ_1. This just means a redefinition of the constants A_1, A_2, C_1 and C_2 as they appear in (6.35) and (6.36), and it also makes the later patching simple,

$$\begin{aligned} F_{\mathrm{I}}(\rho) &= C_1 e^{(\lambda_0 - \frac{\delta_0}{2})(\rho-\rho_1)} + C_2 e^{(-\lambda_0 - \frac{\delta_0}{2})(\rho-\rho_1)}, \\ F_{\mathrm{II}}(\rho) &= \left[A_1 \cos\Big(\omega_T(\rho-\rho_1)\Big) + A_2 \sin\Big(\omega_T(\rho-\rho_1)\Big)\right] e^{-\frac{\delta_0}{2}(\rho-\rho_1)}. \end{aligned} \tag{6.38}$$

We use (6.37) and additionally require that $\mathrm{d}F_{\mathrm{I}}(0)/\mathrm{d}\rho = 0$ to avoid unwanted kinks at the origin. The result is a real spinor component given by

$$\begin{aligned} \tilde{u}_1(\rho) = \frac{N_1}{\sqrt{\rho}} \Bigg\{ & \Theta(\rho_1 - \rho) \left[b e^{(\lambda_0 - \frac{\delta_0}{2})(\rho-\rho_1)} + e^{(-\lambda_0 - \frac{\delta_0}{2})(\rho-\rho_1)} \right] \\ & + \Theta(\rho - \rho_1) \left[(b+1)\cos\Big(\omega_T(\rho-\rho_1)\Big) + \frac{\lambda_0}{\omega_T}(b-1)\sin\Big(\omega_T(\rho-\rho_1)\Big) \right] e^{-\frac{\delta_0}{2}(\rho-\rho_1)} \Bigg\}, \end{aligned} \tag{6.39}$$

with N_1 being a normalization constant and

$$b = \frac{\lambda_0 + \frac{\delta_0}{2}}{\lambda_0 - \frac{\delta_0}{2}} e^{2\lambda_0\rho_1}. \tag{6.40}$$

To generally find N_1, determined by $1 = 4\pi N_1^2 \int_0^\infty \mathrm{d}\rho\, \rho |\tilde{u}_1|^2$, is tedious. Instead, we carefully apply $|\eta_0| \gg \eta_T > (\delta_0/2)^2$ during the calculation and keep only the greatest powers of λ_0. In this limit, the exponential part of $\tilde{u}_1$ for $\rho < \rho_1$ shrinks while the sinusoidal part for $\rho > \rho_1$ is dominating; see Figure 6.2(a). After basic integration we acquire the result

$$N_1 \approx \sqrt{\frac{\delta_0 \eta_T}{2\pi}} \frac{1}{\lambda_0} e^{-2\lambda_0\rho_1}. \tag{6.41}$$

6.2.4 Outer Edge at ρ_2

The system $\mathcal{H}_2$ is not fully a mirror reflection of $\mathcal{H}_1$, and this is due to the radial nature of the problem. However, when ρ_2 becomes large we can, based on exponential suppression, apply reasonable approximations. One may use the solutions in (6.35) and (6.36) to set up the real solutions, F_{I} and F_{II}. After using (6.37), with evaluation at ρ_2 instead of ρ_1, one runs into inconsistency problems when demanding $\mathrm{d}F_{\mathrm{I}}(0)/\mathrm{d}\rho = 0$. More intuitively, F_{I} will have an unacceptable kink at the origin due to its exponential dependency. This makes us require $F_{\mathrm{I}} = F_{\mathrm{II}} = 0$, and $\tilde{u}_2$ is consequentially restricted to being imaginary. We therefore study the solutions G_{I} and G_{II},

$$\begin{aligned} G_{\mathrm{I}}(\rho) &= \left[B_1 \cos\Big(\omega_T(\rho-\rho_2)\Big) + B_2 \sin\Big(\omega_T(\rho-\rho_2)\Big)\right] e^{\frac{\delta_0}{2}(\rho-\rho_2)}, \\ G_{\mathrm{II}}(\rho) &= D_1 e^{(\lambda_0+\frac{\delta_0}{2})(\rho-\rho_2)} + D_2 e^{(-\lambda_0+\frac{\delta_0}{2})(\rho-\rho_2)}. \end{aligned} \tag{6.42}$$

This time we may (only) fix $D_1 = 0$ to have $\lim_{\rho\to\infty} G_{\mathrm{II}}(\rho) = 0$ (recall that $\lambda_0 > \delta_0/2$). Furthermore, if we assume that $\rho_2\delta_0/2 \gg 1$, the derivative at the origin is highly suppressed $\mathrm{d}G_{\mathrm{I}}(0)/\mathrm{d}\rho \approx 0$ due to the exponential part of the function. We use the patching criterion in (6.37) at ρ_2 on the remaining solution and obtain the asymptotic spinor component

$$\begin{aligned} \tilde{u}_2(\rho) = \frac{iN_2}{\sqrt{\rho}} \Bigg\{ &\Theta(\rho_2-\rho)\left[\cos\Big(\omega_T(\rho-\rho_2)\Big) - \frac{\lambda_0}{\omega_T}\sin\Big(\omega_T(\rho-\rho_2)\Big)\right] e^{\frac{\delta_0}{2}(\rho-\rho_2)} \\ &+ \Theta(\rho-\rho_2) e^{(-\lambda_0+\frac{\delta_0}{2})(\rho-\rho_2)} \Bigg\}. \end{aligned} \tag{6.43}$$

Again, the normalization constant N_2 is calculated by keeping only the greatest powers of λ_0 while assuming that $\rho_2\delta_0/2 \gg 1$. The result is

$$N_2 \approx \sqrt{\frac{\delta_0\eta_T}{2\pi}}\frac{1}{\lambda_0}. \tag{6.44}$$

Note that there is a slight asymmetry in N_1 and N_2. This has to do exactly with the assumption $\rho_2\delta_0/2 \gg 1$, such that terms of the order $\mathcal{O}(e^{-\delta_0\rho_2})$ were neglected.

6.2.5 Calculating the Energy Splitting

The remaining task of calculating the energy splitting is now a matter of basic integration. We focus on E_+, since $E_- = -E_+$, and look at the two terms in (6.23) separately, $E_+ \equiv E_1 + E_2$. During the following calculation we make repeated use of $|\eta_0| \gg \eta_T > (\delta_0/2)^2$ and keep only the terms with the greatest powers of λ_0.

Observe also that the constant b in equation (6.40) tends to $b \to e^{2\lambda_0\rho_1}$ and that $\Delta\eta \approx |\eta_0| \approx \lambda_0^2$ in this limit. We find that

$$\begin{aligned}
E_1 &= \pi i\, \Delta\eta \int_0^{\rho_1} \mathrm{d}\rho\, \rho\, \overbrace{(\tilde{u}_1^* \tilde{u}_2 - \tilde{u}_1 \tilde{u}_2^*)}^{2i\tilde{u}_1 \mathrm{Im}(\tilde{u}_2)} \\
&\approx -2\pi N_1 N_2\, \Delta\eta \int_0^{\rho_1} \mathrm{d}\rho\, \left[b e^{(\lambda_0 - \frac{\delta_0}{2})(\rho-\rho_1)} + e^{(-\lambda_0 - \frac{\delta_0}{2})(\rho-\rho_1)} \right] \\
&\qquad \times \left[\cos\Big(\omega_T(\rho-\rho_2)\Big) - \frac{\lambda_0}{\omega_T} \sin\Big(\omega_T(\rho-\rho_2)\Big) \right] e^{\frac{\delta_0}{2}(\rho-\rho_2)} \\
&\approx 2\pi N_1 N_2 \frac{\lambda_0}{\omega_T} b e^{-\lambda_0\rho_1} e^{-\frac{\delta_0}{2}\Delta\rho}\, \Delta\eta \int_0^{\rho_1} \mathrm{d}\rho\, e^{\lambda_0\rho} \sin\Big(\omega_T(\rho-\rho_2)\Big) \\
&\approx -2\pi N_1 N_2 \frac{\lambda_0^2}{\omega_T(\lambda_0^2+\omega_T^2)} b\, \Delta\eta\, \sin(\omega_T\Delta\rho) e^{-\frac{\delta_0}{2}\Delta\rho} \\
&\approx -\frac{\delta_0 \eta_T}{\omega_T} \sin(\omega_T\Delta\rho) e^{-\frac{\delta_0}{2}\Delta\rho}.
\end{aligned} \tag{6.45}$$

The other contributing integral, E_2, is evaluated in the same limit,

$$\begin{aligned}
E_2 &= -\pi i\, \Delta\eta \int_{\rho_2}^{\infty} \mathrm{d}\rho\, \rho\, \overbrace{(\tilde{u}_1 \tilde{u}_2^* - \tilde{u}_1^* \tilde{u}_2)}^{-2i\tilde{u}_1 \mathrm{Im}(\tilde{u}_2)} \\
&\approx -2\pi N_1 N_2\, \Delta\eta \int_{\rho_2}^{\infty} \mathrm{d}\rho\, \left[(b+1)\cos\Big(\omega_T(\rho-\rho_1)\Big) + \frac{\lambda_0}{\omega_T}(b-1)\sin\Big(\omega_T(\rho-\rho_1)\Big) \right] \\
&\qquad \times e^{-\frac{\delta_0}{2}(\rho-\rho_1)} e^{(-\lambda_0 + \frac{\delta_0}{2})(\rho-\rho_2)} \\
&\approx -2\pi N_1 N_2 \frac{\lambda_0}{\omega_T}(b-1) e^{\lambda_0\rho_2} e^{-\frac{\delta_0}{2}\Delta\rho}\, \Delta\eta \int_{\rho_2}^{\infty} \mathrm{d}\rho\, e^{-\lambda_0\rho} \sin\Big(\omega_T(\rho-\rho_1)\Big) \\
&\approx -2\pi N_1 N_2 \frac{\lambda_0^2}{\omega_T(\lambda_0^2+\omega_T^2)}(b-1)\, \Delta\eta\, \sin(\omega_T\Delta\rho) e^{-\frac{\delta_0}{2}\Delta\rho} \\
&\approx -\frac{\delta_0 \eta_T}{\omega_T} \sin(\omega_T\Delta\rho) e^{-\frac{\delta_0}{2}\Delta\rho}.
\end{aligned} \tag{6.46}$$

Hence, the energy $E_+ = E_1 + E_2$ is in the limit $\eta_0 \to -\infty$ given by

$$\boxed{E_+(\Delta\rho) \approx -\frac{2\delta_0\eta_T}{\sqrt{\eta_T - \left(\frac{\delta_0}{2}\right)^2}} \sin\left(\sqrt{\eta_T - (\delta_0/2)^2}\Delta\rho \right) e^{-\frac{\delta_0}{2}\Delta\rho}}. \tag{6.47}$$

It is expected to be an asymptotic result valid when $\Delta\rho \gg 2/\delta_0$ and both $\rho_1, \rho_2 \gg 1/\omega_T$. Note that since $E_1 = E_2$, within our approximation, terms of the type $\langle \boldsymbol{\phi}_+ | \mathcal{H} | \boldsymbol{\phi}_- \rangle = -E_1 + E_2$ result in 0. This means that the spinors $\boldsymbol{\phi}_\pm$ are in fact diagonal in the energy basis. The expression derived above has some important

consequences that deserve being commented before we compare it to numerical results.

6.2.6 Interpretation and Consequences

The Majorana (quasiparticle) operators corresponding to the spinors $\boldsymbol{\phi}_\pm$ are given by (6.3),

$$\Gamma_\pm = \int \mathrm{d}^2 r \left(\frac{\tilde{u}_1^* \mp i\tilde{u}_2^*}{\sqrt{2}} \psi(\boldsymbol{r}) e^{-i\theta\frac{\ell+1}{2}} + \frac{\tilde{u}_1 \pm i\tilde{u}_2}{\sqrt{2}} \psi^\dagger(\boldsymbol{r}) e^{i\theta\frac{\ell+1}{2}} \right). \tag{6.48}$$

The expression in equation (6.47) predicts that these Majorana operators are associated with zero energy excitations only for particular values of the domain separation, which we denote by $\Delta\rho_c$. Thus, a *zero mode criterion*,

$$\Delta\rho_c = \frac{n\pi}{\sqrt{\eta_T - \left(\frac{\delta_0}{2}\right)^2}}, \tag{6.49}$$

for integers $n \in \mathbb{N}$. However, since the result is assumed to hold for large $\Delta\rho$, the integers n satisfying (6.49) may potentially be large. Whenever $\Delta\rho = \Delta\rho_c$ there are two degenerate ground states, $|G_1\rangle$ and $|G_2\rangle = \Gamma_+^\dagger |G_1\rangle$. The states $|G_1\rangle$ and $|G_2\rangle$ can in principle be constructed with the same procedure as studied in detail in section 4.2 for the open Kitaev chain. The zero mode condition gives strong associations of an interference phenomenon. We interpret it as being caused by the oscillating edge modes that convolute in a destructive manner when $\Delta\rho = \Delta\rho_c$. In 2013 B. Rosenstein et al. [35] studied the same circular system of *small size*, in our terminology $\delta_0\Delta\rho/2 \approx 1$. In that case, the same zero energy criterion is found in the limit $\eta_T \gg (\delta_0/2)^2$ by imposing Dirichlet boundary conditions on the wavefunctions directly.

Generally, when $\Delta\rho \neq \Delta\rho_c$, equation (6.47) predicts that there is an energy splitting of $E_+ \neq 0$ between the states $|G_1\rangle$ and $|G_2\rangle$. The oscillating sign of $E_+(\Delta\rho)$ is reflecting an alternating preference on the ground state combination, i.e. $\boldsymbol{\phi}_+$ or $\boldsymbol{\phi}_-$. For instance, if $\sin(\omega_T\Delta\rho) < 0$, then $E_+ > 0$ and $\boldsymbol{\phi}_+$ is the positive energy spinor, which we interpret as the physical ground state spinor. Recall that quasiparticles were defined to have positive energy. This shifting preference on the ground state combination is in contrast to the double well problem, in which the symmetric configuration is the permanently preferred one [17]. Recall that we have assumed that $\eta_T > (\delta_0/2)^2$. If $0 < \eta_T < (\delta_0/2)^2$ the solutions in the topological region also become hyperbolic with no spatial oscillations, meaning the effective solutions in equation (6.35). It is expected to have the effect of replacing the sinusoidal function in (6.47) with a hyperbolic sine. In other words, no true zero modes should occur when $0 < \eta_T < (\delta_0/2)^2$. By the word "true" we mean not taking into account exponentially small energies.

In 2010 M. Cheng et al. [34] calculated the energy splitting between Majorana modes localized in two vortices of separation of R in the limit $R \gg \xi$, with ξ the coherence length. They found an energy splitting of

$$E_+ \approx \sqrt{\frac{2}{\pi}}\Delta_0 \frac{\cos\left(k_F R + \frac{\pi}{4}\right)}{\sqrt{k_F R}} e^{-\frac{R}{\xi}}, \tag{6.50}$$

with $k_F = \sqrt{2m\epsilon_F - \Delta_0^2/v_F^2}$ and $\Delta_0 \ll \epsilon_F$. It reminds of our result, expect for an even stronger fall-off in separation in the additional factor of $1/\sqrt{R}$. The Majorana modes live on a circular boundary in the disk geometry we have studied. This is in contrast to point-like vortices where (6.50) holds. The dimensional difference in the platforms hosting the modes may intuitively explain this observation.

6.3 Matrix Formulation by Discretization

The BdG equations are now approached by discretization of the derivatives, with the aim of formulating them as a matrix eigenvalue problem. This method is commonly applied in computational physics [27]. We discretize the integration domain by some (large) integer N and a corresponding step length h,

$$\rho_i = \rho_{\min} + ih, \quad \text{with} \quad h \equiv \frac{\rho_{\max} - \rho_{\min}}{N+1}. \tag{6.51}$$

Above, we used the notation $\rho_{\min}$ and $\rho_{\max}$ instead of ρ_1 and ρ_2 to avoid confusion with the discretized positions ρ_i. It means that we are interested in the solutions on the N internal points, which we denote $\tilde{u}(\rho_i) \equiv \tilde{u}_i \; \forall i \in \{1, \ldots, N\}$. Symmetric approximations for derivatives are used,

$$\frac{\mathrm{d}^2\tilde{u}(\rho)}{\mathrm{d}\rho^2} \approx \frac{\tilde{u}(\rho_i + h) - 2\tilde{u}(\rho_i) + \tilde{u}(\rho_i - h)}{h^2} = \frac{1}{h^2}\left(\tilde{u}_{i+1} - 2\tilde{u}_i + \tilde{u}_{i-1}\right), \tag{6.52}$$

and

$$\frac{\mathrm{d}\tilde{u}(\rho)}{\mathrm{d}\rho} \approx \frac{\tilde{u}(\rho_i + h) - \tilde{u}(\rho_i - h)}{2h} = \frac{\tilde{u}_{i+1} - \tilde{u}_{i-1}}{2h}. \tag{6.53}$$

Both approximations have local truncation errors of $\mathcal{O}(h^2)$. Inserting these approximation in (6.11) leads to the discretized eigenvalue equations

$$\begin{aligned}
&\left[-\frac{1}{h^2}+\frac{1}{2h\rho_i}\right]\tilde{u}_{i-1}+\left[\frac{2}{h^2}+\frac{1}{\rho_i^2}\left(\frac{\ell+1}{2}\right)^2-\eta\right]\tilde{u}_i+\left[-\frac{1}{h^2}-\frac{1}{2h\rho_i}\right]\tilde{u}_{i+1}\\
&\qquad\qquad -\frac{\delta_0}{2h}\tilde{v}_{i-1}+\frac{\delta_0}{2\rho_i}\tilde{v}_i+\frac{\delta_0}{2h}\tilde{v}_{i+1}=\varepsilon\tilde{u}_i,\\
&-\left[-\frac{1}{h^2}+\frac{1}{2h\rho_i}\right]\tilde{v}_{i-1}-\left[\frac{2}{h^2}+\frac{1}{\rho_i^2}\left(\frac{\ell+1}{2}\right)^2-\eta\right]\tilde{v}_i-\left[-\frac{1}{h^2}-\frac{1}{2h\rho_i}\right]\tilde{v}_{i+1}\\
&\qquad\qquad +\frac{\delta_0}{2h}\tilde{u}_{i-1}-\frac{\delta_0}{2\rho_i}\tilde{u}_i-\frac{\delta_0}{2h}\tilde{u}_{i+1}=\varepsilon\tilde{v}_i.
\end{aligned} \tag{6.54}$$

It is convenient to express this as a matrix equation. We introduce several quantities to have a manageable notation:

$$a_i \equiv -\frac{1}{h^2}-\frac{1}{2h\rho_i}, \quad b_i \equiv -\frac{1}{h^2}+\frac{1}{2h\rho_i}, \tag{6.55}$$

$$c_i \equiv \frac{2}{h^2}+\frac{1}{\rho_i^2}\left(\frac{\ell+1}{2}\right)^2-\eta, \quad d \equiv \frac{\delta_0}{2h} \quad \text{and} \quad e_i \equiv \frac{\delta_0}{2\rho_i}. \tag{6.56}$$

Finally, a vector of coefficients is introduced,

$$\mathbf{\Phi} \equiv \left(\tilde{u}_1,\ \tilde{v}_1,\ \tilde{u}_2,\ \tilde{v}_2,\ \ldots,\ \tilde{u}_N,\ \tilde{v}_N\right)^T. \tag{6.57}$$

The discretized BdG equations are now expressed as the eigenvalue problem

$$\mathcal{A}\mathbf{\Phi} = \varepsilon\mathbf{\Phi}, \tag{6.58}$$

with $\mathcal{A}$ equal to the following $2N \times 2N$, *heptadiagonal* matrix:

$$\mathcal{A} = \begin{pmatrix}
c_1 & -e_1 & a_1 & -d & 0 & 0 & 0 & 0 & \ldots & 0\\
e_1 & -c_1 & d & -a_1 & 0 & 0 & 0 & 0 & \ldots & 0\\
b_2 & d & c_2 & -e_2 & a_2 & -d & 0 & 0 & \ldots & 0\\
-d & -b_2 & e_2 & -c_2 & d & -a_2 & 0 & 0 & \ldots & 0\\
0 & 0 & b_3 & d & c_3 & -e_3 & a_3 & -d & \ldots & 0\\
0 & 0 & -d & -b_3 & e_3 & -c_3 & d & -a_3 & \ddots & 0\\
\vdots & \vdots & \vdots & \ddots & \ddots & \ddots & \ddots & \ddots & \ddots & \vdots\\
0 & 0 & 0 & 0 & 0 & 0 & 0 & 0 & \ddots & -e_N\\
0 & 0 & 0 & 0 & 0 & 0 & 0 & 0 & \ldots & -c_N
\end{pmatrix}. \tag{6.59}$$

The matrix above is real but not symmetric. Still, the eigenvalues of $\mathcal{A}$ should be real and respect the particle-hole-symmetry; they should come in pairs of opposite signs – a readily available test of the implementation. Even though the symbol ε was used in this section to denote dimensionless energy, we will denote the numerically computed ground state energy by E_0 in the remainder of this chapter.

6.4 Numerical Diagonalization and Discussion

This section contains a brief description on how the eigenproblem formulation in the previous section was implemented in `C++`. Then, we present a selection of results where the numerically computed solutions are compared to the approximative solutions found in section 6.2. The chapter is closed with a discussion of the results and conclusive remarks.

6.4.1 Implementation

In close analogy to the one-dimensional Kitaev chain diagonalization, the linear algebra package `Armadillo` was used as tool. Specifically, its built-in eigenproblem solver `eig_gen()` was applied. Returned eigenvectors and eigenvalues, corresponding to the smallest (positive) energy in absolute magnitude, were extracted and written to text files.[1] Normalization of the numerically found eigenvectors was done according to (6.13) with the Trapezoidal rule. A symmetric spectrum was used as a program test, indicating whether the discretization integer N was chosen large enough or not. Notice that the matrix $\mathcal{A}$ has $2N$ eigenvalues, such that the numerically found spectrum becomes extensive when we tune the resolution up. Typically, a full matrix diagonalization with $N > 10^3$ became slow and memory demanding. The general structure of the core `C++` script is not attached since it is a reuse of the the code structure in Appendix D.1. `Python` and the plotting package `matplotlib` were used for reading information from files and plotting results.

It is of interest to numerically compute the energy splitting as function of boundary separation, mainly to see how the energy agrees with our analytical approximation from equation (6.47). We denote the numerically computed value by $E_0(\Delta\rho)$ to distinguish it from $E_+(\Delta\rho)$. The script that was written to find eigenvalues was applied a large number of times. More precisely, we kept ρ_1 fixed and let ρ_2 take m uniformly spaced values in some interval. For each value of ρ_2, we set up the matrix $\mathcal{A}$ and diagonalized it as before. For practical purposes, the value of N was kept fixed as ρ_2 increased, meaning that precision in practice is reduced with $\Delta\rho$.

6.4.2 Results

The numerically computed wavefunctions should be compared to the asymptotic spinors from section 6.2. We therefore summarize the one-edge spinors in the limit $\eta_0 \to -\infty$ (ρ_1 and ρ_2 are now used to denote the inner and outer boundaries again). We stress that these approximations are valid when $\Delta\rho \gg 2/\delta_0$ and $\rho_1, \rho_2 \gg 1/\omega_T$,

[1] A pair of eigenvalues with clearly smaller magnitude than the rest, and of opposite signs, were generally recognized in the spectrum when $\eta > 0$. When $\eta < 0$, no such pair appeared, in agreement with the distinction between the topological and the trivial regime in the $p + ip$ model.

$$\begin{aligned}\boldsymbol{\phi}_1 &= \frac{N}{\sqrt{\rho}}\sin\Big(\omega_T(\rho-\rho_1)\Big)\Theta(\rho-\rho_1)\Theta(\rho_2-\rho)e^{-\frac{\delta_0}{2}(\rho-\rho_1)}\begin{pmatrix}e^{i\theta(\ell+1)/2}\\ e^{-i\theta(\ell+1)/2}\end{pmatrix},\\ \boldsymbol{\phi}_2 &= \frac{N}{\sqrt{\rho}}\sin\Big(\omega_T(\rho_2-\rho)\Big)\Theta(\rho-\rho_1)\Theta(\rho_2-\rho)e^{-\frac{\delta_0}{2}(\rho_2-\rho)}\begin{pmatrix}ie^{i\theta(\ell+1)/2}\\ -ie^{-i\theta(\ell+1)/2}\end{pmatrix}.\end{aligned} \tag{6.60}$$

Normalized on the interval $\rho\in[\rho_1,\rho_2]$, the constant N evaluates to

$$N=\sqrt{\delta_0/\left[2\pi\left(1-\frac{(\delta_0/2)^2}{\eta_T}\right)\right]}, \tag{6.61}$$

when terms of the order $\mathcal{O}(e^{-\delta_0\Delta\rho})$ are neglected. The linear combinations

$$\boldsymbol{\phi}_\pm=\frac{1}{\sqrt{2}}\left(\boldsymbol{\phi}_1\pm i\boldsymbol{\phi}_2\right) \tag{6.62}$$

are used as visual comparison to the numerically obtained solutions. To pick out the correct combination, we simply checked the sign of $\sin(\omega_T\Delta\rho)$ numerically; if it is negative $\boldsymbol{\phi}_+$ is chosen and vice versa. Note that unless $\Delta\rho=\Delta\rho_c$, the spinors in (6.60) do not, strictly speaking, obey the Dirichlet boundary conditions that the two-edged system demands. They are still used as approximative solutions.

In Figure 6.3 we have plotted the lowest energy state resulting from a numerical diagonalization of $\mathcal{A}$ with $\ell=-1$ as coloured triangles for a representative sample of positions. They are plotted along with the analytical approximations form equation (6.62) and (6.60). The choice of ℓ was based on the previous chapter, in which we discussed how $\ell=-1$ corresponded to the fundamental vorticity. The parameters are kept fixed but $\Delta\rho$ gradually increased through the subfigures (a) to (d). The discretization integer was fixed to $N=1500$. More details are provided in the figure caption. In Figure 6.4 the numerically computed energy splitting, $E_0(\Delta\rho)$, and the analytical approximation, $E_+(\Delta\rho)$, are plotted as function of $\Delta\rho$, with the inner boundary at $\rho_1=40$ and the outer boundary in the range $\rho_2\in[42,60]$ for $m=500$ uniformly spaced values. This simulation was done with the discretization integer constantly fixed to $N=500$.

6.4.3 Discussion and Conclusive Remarks

From Figure 6.3 we see that the trial spinors from (6.62) agree visually with the numerical solutions. The edge modes are expectedly localized close to the boundaries and, as anticipated from equation (6.62) and (6.60), exponentially suppressed towards the center part of the disk $\mathcal{D}$. A general observation was made during the simulations. When the energy of the ground state was close to the floating point precision, typically of the order $\mathcal{O}(10^{-15})$, the resulting eigenvectors did not fit well with the analytical approximations. This is related to the specific details of how the

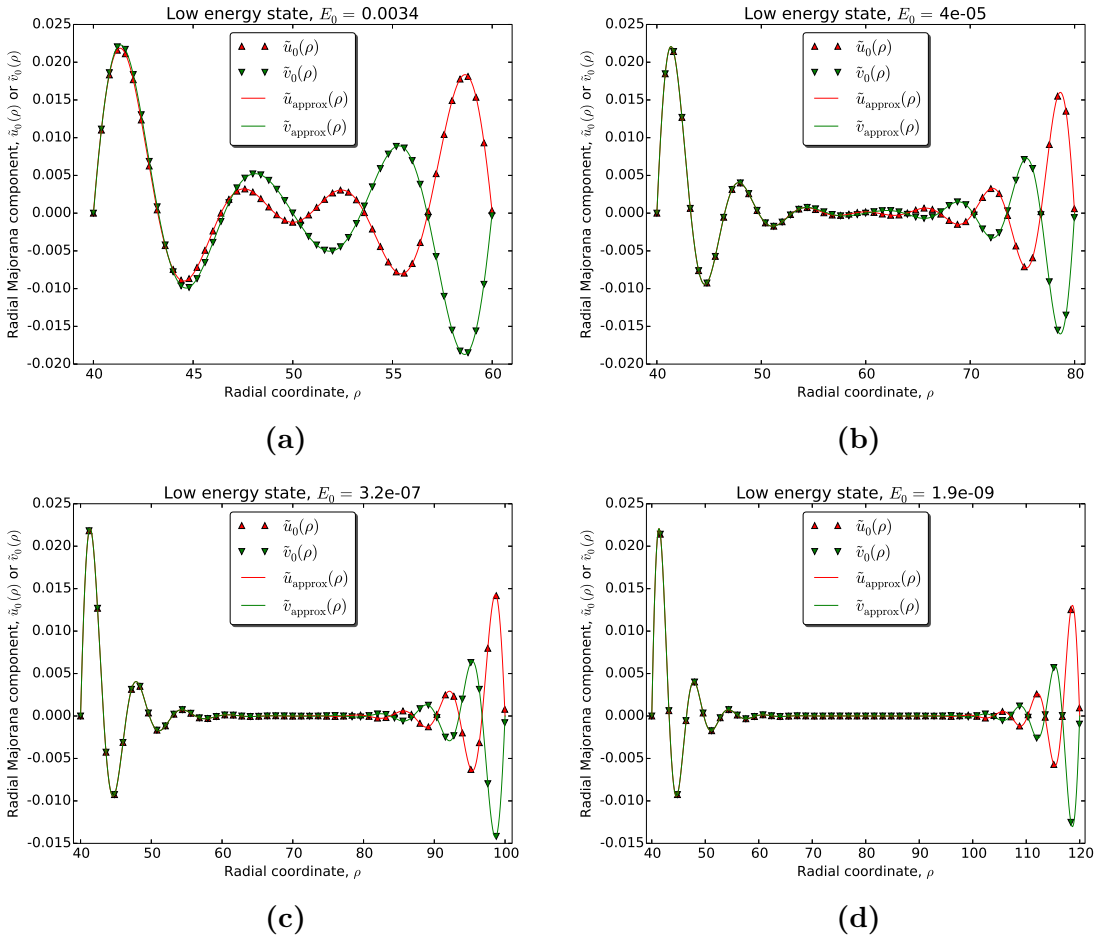

Figure 6.3: Radial Majorana component/wavefunction, $\tilde{u}_0(\rho)$ or $\tilde{v}_0(\rho)$, as function of radial distance ρ for the lowest energy state. Parameters were fixed to $\eta = 1.0$, $\delta_0 = 0.5$, $\ell = -1$ with discretization integer $N = 1500$. The smallest positive energy, denoted by E_0, is displayed in the respective titles. Analytical approximations, denoted here by $\tilde{u}_{\text{approx}}(\rho)$ or $\tilde{v}_{\text{approx}}(\rho)$, corresponding to the components of either $\boldsymbol{\phi}_+$ or $\boldsymbol{\phi}_-$ from equation (6.62) and (6.60), are plotted as continuous curves. Sample values from the numerical experiment are shown as triangles. The inner boundary was kept at $\rho_1 = 40$ and the outer boundary varied according to **(a)** $\rho_2 = 60$, **(b)** $\rho_2 = 80$, **(c)** $\rho_2 = 100$ and **(d)** $\rho_2 = 120$. Even for boundary separation, $\Delta\rho = 20$, there is good agreement between the trial spinor and the numerical solution.

solver `eig_gen()` works. However, it is thought to stem from the fact that we could receive rotations of eigenvectors within what is numerically seen as a zero energy subspace. Problems related to this were generally avoided by reducing $\Delta\rho$, and by checking that the eigenvalues were returned in pairs of opposite signs. Note that exactly the same problem was present and discussed in the diagonalization of the open Kitaev chain.

The energy splitting from Figure 6.4 shows a satisfactory agreement between the numerically obtained values and the analytical approximation when the boundary separation increases. This is quite remarkable when considering all the simplifica-

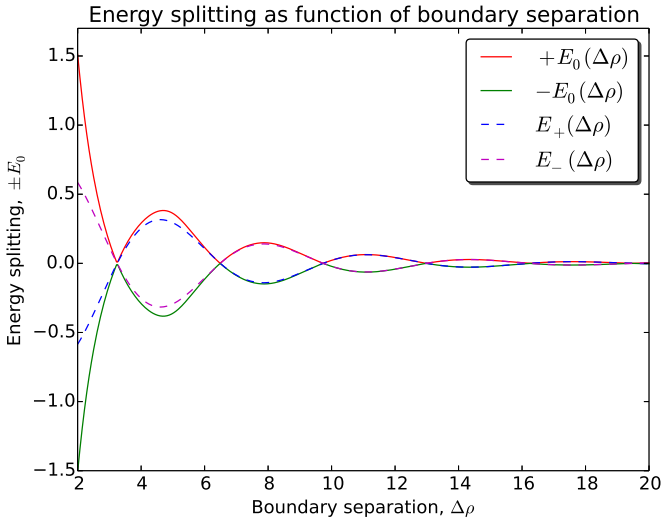

(a)

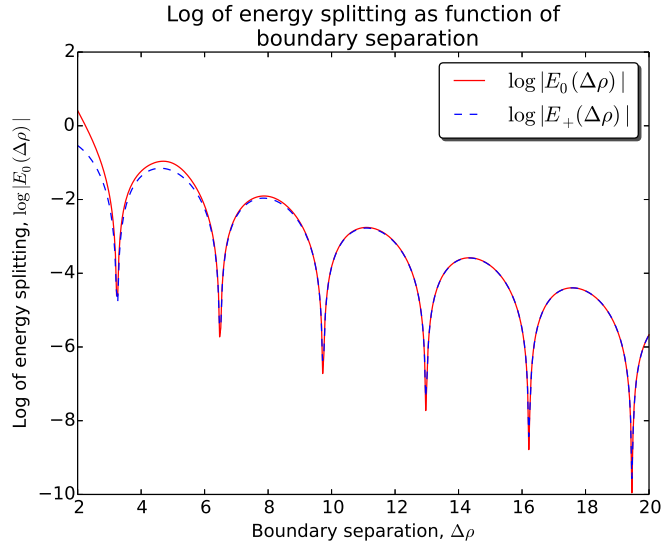

(b)

Figure 6.4: The energy splitting as function of boundary separation with parameters $\eta = 1.0$, $\delta_0 = 0.5$ and discretization integer $N = 500$ for $\ell = -1$. The value $\rho_1 = 40$ was held fixed and $\rho_2 \in [42, 60]$ with $m = 500$ uniformly spaced values. **(a)** The energies $\pm E_0(\Delta\rho)$ – numerical values and continuous curves – and $E_\pm(\Delta\rho)$ – analytical values and dashed curves – as function of $\Delta\rho$. **(b)** The logarithms $\log|E_0(\Delta\rho)|$ and $\log|E_+(\Delta\rho)|$ as function of $\Delta\rho$. Already for $\delta_0\Delta\rho/2 \approx 3$, corresponding to $\Delta\rho \approx 12$ in the figure, the two curves are in satisfactory agreement. The analytical approximation from equation (6.47) is confirmed as a limiting result.

tions performed to arrive at the result. From a numerical perspective, these simulations quickly became slow since a matrix of dimension $2N \times 2N$ is diagonalized for each of the m values of boundary separations. Hence, N was, just by consideration of computation time, restricted to $N = 500$. The limited resolutions, determined by m and N, also explain why the logarithmic values in Figure 6.4(b) do not diverge at the critical boundary separations. Hitting the exact values of $\Delta\rho_c$ is very unlikely

with a finite resolution.

One thing to notice about both the radial part of the spinors in (6.60) and the energy splitting in (6.47), is that neither expression have any dependency on ℓ. Of course, the true solutions from (6.30) and (6.32) depend on ℓ, but this information is lost in the asymptotic solution basis. Performing the energy splitting calculation from section 6.2 exactly with, for instance, $\ell = -1$ will result in a more technical calculation. This is because the Bessel functions are not perfectly periodic for small arguments. It serves as a suggestive calculation that may be performed in an extension of this work. Moreover, we have kept a particular focus on the assumption of $\eta_T > (\delta_0/2)^2$. This was seen to result in wavefunctions, and the energy splitting, having spatial oscillations. Assuming instead that $0 < \eta_T < (\delta_0/2)^2$ is expected to have the effect of replacing sinusoidal functions with hyperbolic sines in the expressions above. It was confirmed numerically that both the energy splitting and the edge modes became purely exponential functions in this parameter regime. Furthermore, it basically answers the main consequence of including the ∇^2 term in the Hamiltonian. The parametrical distinction between $\eta_T > (\delta_0/2)^2$ and $0 < \eta_T < (\delta_0/2)^2$ reflects whether wavefunctions and the energy splitting oscillate or not. With these remarks we close our consideration of the $p + ip$ model.

Chapter 7

Experimental Activity and Conclusions

7.1 Experimental Status

The prediction of Majorana fermions localized on the ends of nanowires has become a hot experimental research topic. As mentioned earlier, the ultimate and long-term goal is to utilize Majorana fermions in a topological quantum computer. Ideally, one may imagine braiding Majoranas in a network of wires with voltage gates and T-shaped junctions as described in [7]. However, experimentally verifying Majorana fermions has proven to be demanding. Lately, several experiments have shown promising evidence in accordance with predicted signatures. We will briefly summarize two of the most influential experiments to illustrate how active this field is. The figures in this section are reprinted with permission from the American Association for the Advancement of Science (AAAS).[1]

In 2012 V. Mourik et al. [8] reported from an advanced experiment. They performed electrical measurements on a nanowire in contact with a s-wave superconductor and a normal electrode on opposite ends. To effectively obtain spinless electrons, they applied an external magnetic field B parallel to the wire and exploited the Zeeman splitting (for instance discussed in [11]). A tunnel barrier was constructed by applying a negative voltage on a small gate beneath the nanowire. They measured the differential conductance $\mathrm{d}I/\mathrm{d}V$ and voltage V across the barrier, and in this way they performed a tunnelling spectroscopy. The differential conductance spectra, for a range of magnetic field strengths, revealed a zero-energy peak. One of the main results of the experiment can be seen in Figure 7.1. The appearance of the peak was interpreted as a strong indication of a Majorana zero mode. However, it should be pointed out that the peak amplitude was much smaller than expected, and that the wire appears to be short compared to the coherence length. The authors themselves state that they are not aware of any mechanism, other than the existence of an end-Majorana state, capable of explaining their results. But clearly, this does not

[1] Permission to reuse figures was also gained by email correspondence with the article authors.

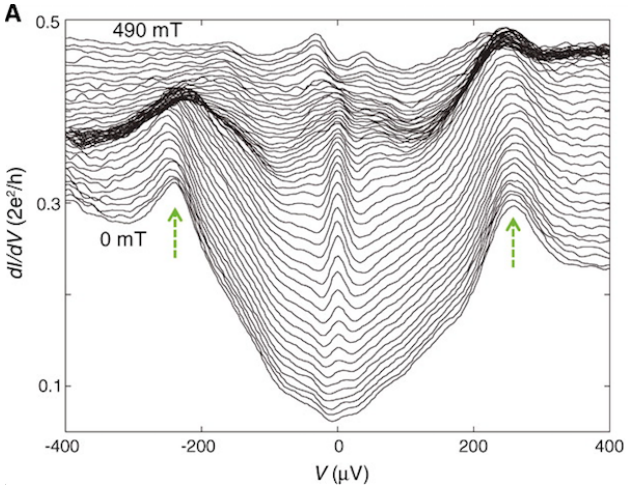

Figure 7.1: Differential conductance spectra, $\mathrm{d}I/\mathrm{d}V$ versus voltage V, across a tunnel barrier in an InSb nanowire in contact with a *s*-wave superconductor at low temperature (70 mK). The different curves correspond to various applied magnetic field strengths, plotted with a systematic offset for clarity. The two green arrows indicate quasiparticle resonances, which can be used to quantitatively determine the induced gap Δ. A zero-voltage peak can be seen when the magnetic field is approximately 100 mT $< B <$ 400 mT. From [8]. Reprinted with permission from AAAS.

guarantee that such explanations exist.

More recently, in 2014, S. Nadj-Perge et al. [9] used sophisticated techniques in an attempt to realize a one-dimensional topological superconductor. They fabricated iron atomic chains on the top of a superconducting layer of lead, see Figure 7.2(a). The coupling of the iron chain to the conventional superconductor with strong spin-orbit coupling was shown to allow for *p*-wave superconductivity without any applied magnetic field (under these circumstances the chain is always in the topological phase). Using scanning tunnelling microscopy, they were able to measure the differential conductance spectra for different locations on the atomic chain, see Figure 7.2(b). The resulting spectra show a tendency of having zero-energy peaks at the ends of the chain. This is evidence of a Majorana zero energy mode. Furthermore, the spectra had the same characteristics as predicted by numerical experiments, especially the occurrence of symmetrically placed in-gap states, seen more or less as two peaks in the upper left panels of Figure 7.2(b). But again, the community seems to be careful about drawing any definite conclusions before having seen more signature effects, in particular on longer chains.

7.2 Concluding Remarks and Outlook

In this thesis, various aspects of topological superconductivity have been demonstrated and explored, and the outcome has been rewarding. We have gradually established details and obtained a more complete view than the schematic descrip-

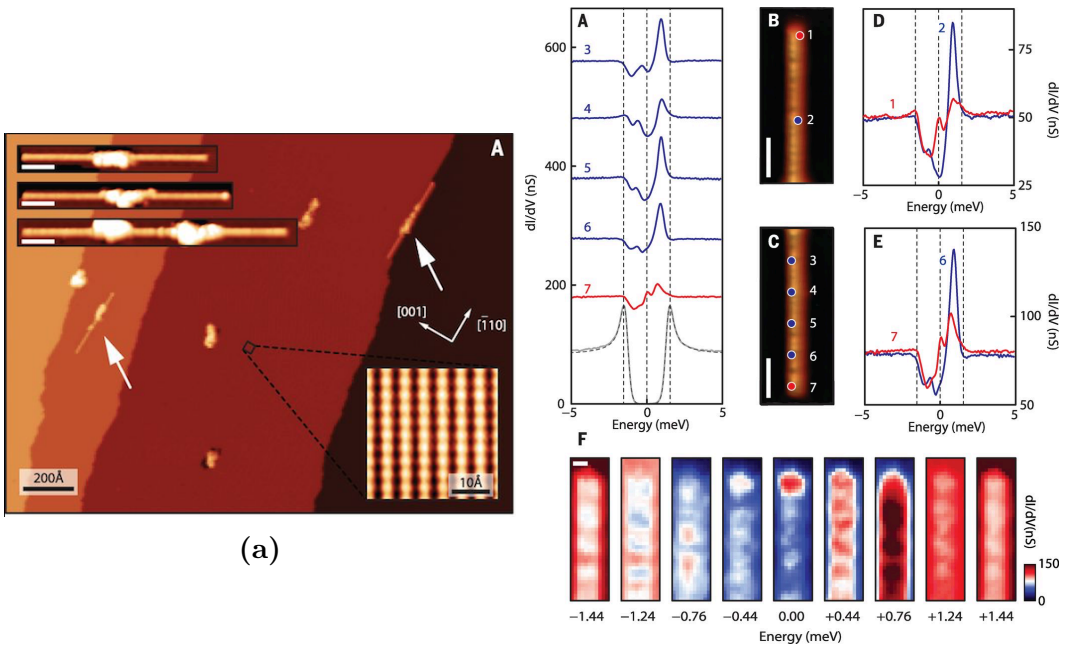

Figure 7.2: **(a)** Topography of a lead surface with islands and chains of iron atoms (white arrows). In the upper left panel, some more or less pure iron chains are shown with white scale bars of 50 Å for reference. **(b)** Differential conductance spectra resulting from scanning tunnelling microscopy in an iron chain. Note that the spectra are plotted with a constant offset for clarity. A tiny zero-energy peak can be seen in the spectra at points 1 and 7. Their corresponding locations on the chain are shown in the upper middle panel. The lower middle panel, with a white scale bar of 10 Å, shows increased conductance in a region close to the end of the chain. From [9]. Reprinted with permission from AAAS.

tions in [5, 11]. We started with a thorough study of the one-dimensional Kitaev chain. The spectrum and the ground state were derived analytically for a closed system. We found the ground state fermion parity to be altered just as μ passed the topological phase transitions at $\pm t$, which is not evident from [11]. Moreover, the topological phase transition was reflected in a Berry phase calculation. The vector $\boldsymbol{h}(k)$ either did or did not circulate the origin, corresponding to the topological and the trivial phase, respectively. Two-point correlation functions of great spatial separation had enlarged values close to the phase transitions, and their maximum values scaled linearly with reciprocal system size. We also found the fermion parity of the ground state to be opposite when comparing periodic to anti-periodic boundary conditions in the topological phase.

The Kitaev chain with open boundary conditions was used to demonstrate the possibility of Majorana fermions at the ends in the topological phase. We pursued a particularly simple parameter choice, $\Delta = t$ and $\mu = 0$, and established details related to the degenerate ground state subspace. It turned out to be non-trivial to choose the correct ground states from a set of three candidate states, $\{|a\rangle, d_0|a\rangle, d_0^\dagger|a\rangle\}$ (from equation (4.16)). The degenerate ground states were also found to be greatly entangled when separating the system ends from the interior. By picking the state

with the correct fermion parity, one of the degenerate states was associated with the unique ground state in the closed chain. This choice was in satisfactory agreement with the defining property of the ground state in the closed system, acting as a confirmation of our result. Thereafter, we numerically studied the energy spectrum and how it was affected by a space varying order parameter. Two additional Majorana modes emerged for a real order parameter subject to a sign change. This was *a posteriori* seen to be in accordance with the results in [28].

We proceeded by studying the $p + ip$ model. A set of consistency relations, including the BdG equations that were implied by expansion of fermion operators in a quasiparticle basis, were derived. The order parameter was then taken to describe a symmetric vortex from Ginzburg-Landau theory. We argued how only odd vorticity agreed with single valued fermion operators. The BdG equation for a Majorana zero mode was solved numerically. A Majorana mode was typically localized within some multiple of the Ginzburg-Landau coherence length from the vortex center. Our description of the vortex equation, and the scheme for solving it, may be extended in future work. Especially with a more complete Ginzburg-Landau theory that takes p-wave pairing rigorously into account. An idealized system of many vortex modes was considered, and we proposed an argument that resulted in the same transformation rule as Ivanov describes [6]. In turn, this transformation rule was seen in the introduction to imply non-Abelian interchange properties.

Finally, we considered the $p+ip$ model on an annulus with constant parameters. We approximated the ground state as a linear combination of edge modes, living on the circular boundaries of systems with only one edge each. We focused on the parameter regime $\eta_T > (\delta_0/2)^2$. In this case, the energy splitting between the edge modes was found to be exponentially suppressed in the boundary separation. The splitting also contained oscillations, which led to a zero mode condition that reminded of an interference phenomenon. Our analytical results were verified by the numerical implementation as the boundary separation was large compared to the decay length scale. Moreover, we have not been capable of finding any references with a similar consideration of this system, even though related discussions were found in [34, 35].

Seen in a wider perspective, topological superconductivity can be characterized as a field of research with great potential. The unambiguous observation of Majorana fermions in topological nanowires or in vortex bound states would be a milestone. Not only because it would confirm a theoretical prediction from 1937, but also because it would give the field a solid experimental foundation. It would probably also shift the focus experimentally to the natural follow-up aspect of Majorana fermions: confirmation of their non-Abelian interchange properties. The flourishing experimental activity in this field is likely to trigger discoveries of new applications and techniques. Despite experimental barriers to overcome, topological superconductors may ultimately turn out to be a platform where a topological quantum computer can be brought to life. And even if that is not the case, the physics of topological superconductors has proven to have great theoretical value in its own right.

Appendices

Appendix A

The Geometrical Phase

In 1984 Michael Berry described adiabatic evolution of energy eigenstates as the parameters of a quantum system perform a loop in parameter space [25, 26]. During an adiabatic evolution, the *Adiabatic Theorem* ensures that if the system prior to the change was in the ground state, it will remain so as long as there is a finite energy gap to the first excited state. Adiabatic evolution is the focus of Appendix B, but we merely mention that the ground state will obtain a phase factor that can be separated into an *energy dependent* part and an *energy independent* part. The energy independent phase is known as the Berry phase for closed contours, and it has three central properties: 1) it is gauge invariant, i.e. a physical measurable quantity, 2) it is a geometrical phase that does not depend on the details of the path in parameter space, and 3) it contains analogies to gauge theory and classical electrodynamics. In this section useful expressions for the geometric vector field, and the corresponding curvature field, are derived. This presentation follows [23] closely and to some extent [26]. For notational convenience in this section, differential operators are sometimes placed inside the ket, such as $|\partial_i \psi\rangle$. This is understood to mean $\partial_i |\psi\rangle$. Summing over repeated indices is implied.

A.1 The Quantum Metric

In the quantum formalism there is a concept of length defined by the metric

$$\mathrm{d}s^2 = \langle \mathrm{d}\psi | \mathrm{d}\psi \rangle \,, \tag{A.1}$$

with $|\mathrm{d}\psi\rangle$ being the difference between the state vectors $|\psi + \mathrm{d}\psi\rangle$ and $|\psi\rangle$. This metric must, however, be modified to stay invariant during arbitrary phase changes of $|\psi\rangle$ and $|\psi + \mathrm{d}\psi\rangle$. After all, phase factors do not represent physical change. A modified metric that takes this into account is

$$\mathrm{d}s^2 = \langle \mathrm{d}\psi | \mathrm{d}\psi \rangle - \langle \mathrm{d}\psi | \psi \rangle \langle \psi | \mathrm{d}\psi \rangle \,. \tag{A.2}$$

Assume next that $\{|n_i\rangle\}$ is a basis of the Hilbert space, such that a general state can be expanded in it,

$$|\psi\rangle = \psi^i \, |n_i\rangle \, . \tag{A.3}$$

Using this expansion in the modified metric (A.2) yields the metric on coordinate form,

$$\mathrm{d}s^2 = \gamma_{ij} \, \mathrm{d}\psi^{*i} \mathrm{d}\psi^j, \tag{A.4}$$

with

$$\gamma_{ij} = \langle n_i | n_j \rangle - \langle n_i | \psi \rangle \, \langle \psi | n_j \rangle \tag{A.5}$$

as the metric tensor. This formulation is strikingly similar to the tensor formulation in general relativity, but in the quantum version γ_{ij} is generally complex and hermitian. Assume that there is a parameter space specified by a set of m coordinates, $\{x^i\}_{i=1}^m$. For each set of coordinates there is an associated state vector $|n_x\rangle$. An infinitesimal change in the state $|n_x\rangle$ is then caused by changes in the coordinates,

$$|\mathrm{d}n_x\rangle = \mathrm{d}x^i \frac{\partial}{\partial x^i} \, |n_x\rangle \equiv |\partial_i n_x\rangle \, \mathrm{d}x^i. \tag{A.6}$$

By inserting this in the metric in (A.4), we find that

$$\mathrm{d}s^2 = \Big[\, \langle \partial_i n_x | \partial_j n_x \rangle - \langle \partial_i n_x | n_x \rangle \, \langle n_x | \partial_j n_x \rangle \, \Big] \mathrm{d}x^i \mathrm{d}x^j. \tag{A.7}$$

Summation over i and j ensure that only the symmetric part of the tensor above remains. This symmetric part is

$$\begin{aligned} g_{ij}(x) &\equiv \frac{1}{2} \Big[\, \langle \partial_i n_x | \partial_j n_x \rangle - \langle \partial_i n_x | n_x \rangle \, \langle n_x | \partial_j n_x \rangle + \langle \partial_j n_x | \partial_i n_x \rangle - \langle \partial_j n_x | n_x \rangle \, \langle n_x | \partial_i n_x \rangle \, \Big] \\ &= \mathrm{Re} \Big[\, \langle \partial_i n_x | \partial_j n_x \rangle - \langle \partial_i n_x | n_x \rangle \, \langle n_x | \partial_j n_x \rangle \, \Big]. \end{aligned} \tag{A.8}$$

It is compactly expressed if we introduce, in analogy to gauge theory and covariant derivatives, a *projective derivative*,

$$\mathrm{D}_j \equiv \partial_j - i a_j, \tag{A.9}$$

with the (state dependent) vector field $a_j(x)$ defined as

$$a_j(x) \equiv -i \, \langle n_x | \partial_j n_x \rangle \, . \tag{A.10}$$

The metric tensor is expressed in terms of this vector field according to

$$\begin{aligned} g_{ij}(x) &= \mathrm{Re}\Big[\, \langle \mathrm{D}_i n_x | \mathrm{D}_j n_x \rangle \,\Big] \\ &= \mathrm{Re}\Big[\, \langle \partial_i n_x | \partial_j n_x \rangle - \langle \partial_i n_x | n_x \rangle \langle n_x | \partial_j n_x \rangle \,\Big] \\ &= \mathrm{Re}\, \langle \partial_i n_x | \partial_j n_x \rangle - a_i a_j. \end{aligned} \tag{A.11}$$

Above, we used that $a_i(x) \in \mathbb{R}$, which is seen from the normalization of $|n_x\rangle$,

$$\langle n_x | n_x \rangle = 1 \Rightarrow \langle \partial_i n_x | n_x \rangle + \langle n_x | \partial_i n_x \rangle = 0 \Rightarrow \mathrm{Im}\; a_i(x) = 0. \tag{A.12}$$

The importance of this vector field becomes clear with the Adiabatic Theorem.

A.2 A New Tensor Field

The fact that $g_{ij}(x) = \mathrm{Re}\,[\langle \mathrm{D}_i n_x | \mathrm{D}_j n_x \rangle]$ suggests the existence of another independent quantity, due the richness stemming from γ_{ij} being complex *a priori*. We define this other object as

$$f_{ij}(x) \equiv 2\,\mathrm{Im}\,\langle \mathrm{D}_i n_x | \mathrm{D}_j n_x \rangle = 2\,\mathrm{Im}\,\langle \partial_i n_x | \partial_j n_x \rangle\,, \tag{A.13}$$

with the factor of 2 simply being convenient. Two equivalent expressions for this new quantity are derived in this section. The first one is found by observing that

$$\begin{aligned} \partial_i a_j - \partial_j a_i &= -i\Big[\, \langle \partial_i n_x | \partial_j n_x \rangle - \langle \partial_j n_x | \partial_i n_x \rangle \,\Big] \\ &= 2\,\mathrm{Im}\,\langle \partial_i n_x | \partial_j n_x \rangle \\ &= f_{ij}(x), \end{aligned} \tag{A.14}$$

which explicitly shows that the tensor is antisymmetric. It also gives associations of the electromagnetic field tensor. There is an alternative formulation that does not require taking derivatives of any basis states. The starting point is the Schrödinger equation with $\{|n_x\rangle\}$ being a complete, orthonormal set of energy eigenstates for every set of parameters x,

$$H(x)\,|n_x\rangle = E_n(x)\,|n_x\rangle\,, \quad \mathbb{1} = \sum_n |n_x\rangle\langle n_x| \quad \text{and} \quad \langle n_x | n'_x \rangle = \delta_{n,n'}. \tag{A.15}$$

Manipulation of these expressions, while assuming $n \neq n'$, yields

$$\begin{aligned} \langle n_x | \frac{\partial H}{\partial x^i} | n'_x \rangle &= \partial_i \overbrace{\langle n_x | H | n'_x \rangle}^{=0} - \langle \partial_i n_x | H | n'_x \rangle - \langle n_x | H | \partial_i n'_x \rangle \\ &= -E_{n'} \langle \partial_i n_x | n'_x \rangle - E_n \langle n_x | \partial_i n'_x \rangle \\ &= (E_{n'} - E_n) \langle n_x | \partial_i n'_x \rangle\,. \end{aligned} \tag{A.16}$$

We combine this with the expressions for $f_{ij}(x)$ in (A.14) and the completeness of basis states,

$$\begin{aligned} f_{ij}(x) &= -i\Big[\,\langle\partial_i n_x|\partial_j n_x\rangle - (i \leftrightarrow j)\Big] \\ &= -i\sum_{n'\neq n}\Big[\,\langle\partial_i n_x|n'_x\rangle\,\langle n'_x|\partial_j n_x\rangle - (i \leftrightarrow j)\Big] \\ &= -i\sum_{n'\neq n}\left[\frac{\langle n_x|\frac{\partial H}{\partial x^i}|n'_x\rangle\,\langle n'_x|\frac{\partial H}{\partial x^j}|n_x\rangle}{(E_n - E_{n'})^2} - (i \leftrightarrow j)\right]. \end{aligned} \tag{A.17}$$

The parenthesis $(i \leftrightarrow j)$ is used here to denote the proceeding expression with indices i and j interchanged. Note that both $a_i(x)$ and $f_{ij}(x)$ are state dependent, which we could have used a subscript n to explicitly point out.

Appendix B

The Adiabatic Theorem

The Adiabatic Theorem is a central pillar in quantum mechanics, first proven in 1928 when quantum theory was still in early development. At that time, the link to the geometric properties of the Berry phase was not established (of course, the factor did not carry the name "Berry phase" either) [26]. We present and prove the theorem in this section. The proof we present follows [23] closely. Some elements are inspired by [17]. As in Appendix A, differential operators are sometimes placed inside the ket in this section. Hence, $|\partial_i \psi\rangle$ means $\partial_i |\psi\rangle$. Summation over repeated indices is implied. Assume that $H = H(x(t))$ is the Hamiltonian of a system with n parameters, $x = \{x_1(t), \ldots, x_n(t)\}$, that change *slowly* with time. The exact meaning of the word "slowly" in this context will be revealed in the derivation. Let $|n_x\rangle$ denote the nth energy eigenstate in an orthonormal basis,

$$H(x)\,|n_x\rangle = E_n(x)\,|n_x\rangle \quad \text{and} \quad \langle n_x|m_x\rangle = \delta_{n,m}. \tag{B.1}$$

The Adiabatic Theorem may be formulated:

THEOREM 1. *If a state is prepared in the (non-degenerate) ground state $|0_x\rangle$ of $H(x(t))$, it will remain in the ground state throughout the time evolution but acquire a phase factor* $\exp(-i\phi(t))$*, with*

$$\phi(t) = \frac{1}{\hbar}\int_0^t \mathrm{d}t'\, E_0(t') - i\int_0^t \mathrm{d}t'\, \dot{x}^k \langle 0_x|\partial_k 0_x\rangle\,. \tag{B.2}$$

Here, ∂_k is the derivative with respect to x^k, and the dot denotes derivative with respect to t'.

PROOF. The general solution to the time-dependent Schrödinger equation may be expanded in terms of time-dependent eigenstates,

$$|\psi(t)\rangle = \sum_n c_n(t) e^{i\theta_n(t)}\,|n_{x(t)}\rangle\,, \tag{B.3}$$

with the phase factor $\theta_n(t)$ commonly known as the *dynamical phase factor*,

$$\theta_n(t) = -\frac{1}{\hbar}\int_0^t \mathrm{d}t'\, E_n(t'). \tag{B.4}$$

Taking the time derivative of equation (B.3) and inserting it into the time-dependent Schrödinger equation yields

$$i\hbar \sum_n \left[\dot{c}_n e^{i\theta_n}\left|n_x\right\rangle + i c_n \dot{\theta}_n e^{i\theta_n}\left|n_x\right\rangle + c_n e^{i\theta_n}\dot{x}^k\left|\partial_k n_x\right\rangle\right] = H\sum_n c_n e^{i\theta_n}\left|n_x\right\rangle. \tag{B.5}$$

Equation (B.1) ensures that the middle term on the left cancels the term on the right hand side. Acting with $\langle m_x|$ on the remaining equation leaves us with

$$\dot{c}_m = -\sum_n c_n \dot{x}^k \left\langle m_x|\partial_k n_x\right\rangle e^{i(\theta_n-\theta_m)}. \tag{B.6}$$

The mth coefficient is found by integrating this expression over time, assuming that the system is prepared in the ground state initially $c_n(0) = \delta_{n,0}$,

$$c_m(t) = \delta_{m,0} - \sum_n \int_0^t \mathrm{d}t_1\, c_n \dot{x}^k \left\langle m_x|\partial_k n_x\right\rangle e^{i[\theta_n(t_1)-\theta_m(t_1)]}. \tag{B.7}$$

Consider the evolution on a large time interval T with fixed end points $x^k(0)$ and $x^k(T)$. We study the coefficients on a small interval δt compared to T: $\delta t \ll T$. Within δt we assume that the energies, E_n, and the coefficients, c_n, may be considered constant. Using (B.7):

$$\begin{aligned}
c_m(t+\delta t) &= \delta_{m,0} - \sum_n \int_0^{t+\delta t} \mathrm{d}t_1\, c_n \dot{x}^k \left\langle m_x|\partial_k n_x\right\rangle e^{i[\theta_n(t_1)-\theta_m(t_1)]} \\
&= \delta_{m,0} - \sum_n \int_0^{t} \mathrm{d}t_1\, c_n \dot{x}^k \left\langle m_x|\partial_k n_x\right\rangle e^{i[\theta_n(t_1)-\theta_m(t_1)]} \\
&\qquad - \sum_n \int_t^{t+\delta t} \mathrm{d}t_1\, c_n \dot{x}^k \left\langle m_x|\partial_k n_x\right\rangle e^{i[\theta_n(t_1)-\theta_m(t_1)]} \\
&\approx c_m(t) - \sum_n c_n \dot{x}^k \left\langle m_x|\partial_k n_x\right\rangle \int_t^{t+\delta t} \mathrm{d}t_1\, e^{\frac{i}{\hbar}\int_0^{t_1}\mathrm{d}t_2\,[E_m(t_2)-E_n(t_2)]} \\
&\approx c_m(t)\left[1 - \dot{x}^k \left\langle m_x|\partial_k m_x\right\rangle \delta t\right] \\
&\qquad + i\hbar \sum_{n\neq m} c_n \dot{x}^k \frac{\left\langle m_x|\partial_k n_x\right\rangle}{E_m - E_n} e^{\frac{i}{\hbar}(E_m-E_n)t}\left(e^{\frac{i}{\hbar}(E_m-E_n)\delta t} - 1\right).
\end{aligned} \tag{B.8}$$

The final term may be neglected if

$$\delta t \gg \frac{\hbar}{|E_m - E_n|}, \tag{B.9}$$

which is called the *adiabatic criterion*. In this limit the equation above gives an expression for the ground state coefficient $c_0(t)$,

$$\begin{aligned} \dot{c}_0 &= -c_0 \dot{x}^k \langle 0_x | \partial_k 0_x \rangle \Rightarrow \\ c_0(t) &= \exp\Big(- \int_0^t \mathrm{d}t \; \dot{x}^k \langle 0_x | \partial_k 0_x \rangle \Big) \\ &= \exp\Big(- \int_{x(0)}^{x(t)} \mathrm{d}x^k \; \langle 0_x | \partial_k 0_x \rangle \Big). \end{aligned} \tag{B.10}$$

This means that the ground state acquires two contributions to the accumulated phase factor in time, $\exp\left(i\theta_0(t) - i\alpha_0(t)\right)$. The first part, $\theta_0(t)$, is *energy dependent* and given by equation (B.4). The second part,

$$\alpha_0(t) \equiv -i \int_{x(0)}^{x(t)} \mathrm{d}x^k \; \langle 0_x | \partial_k 0_x \rangle = \int_{x(0)}^{x(t)} \mathrm{d}x^k \, a_k(x), \tag{B.11}$$

is *energy independent*. It rather depends on the parametric geometry of the ground state. It is called the *geometrical phase* and establishes a connection to the vector field $a_j(x)$ introduced in Appendix A. Furthermore, if the parameter evolution is periodic, $x(0) = x(T)$, *Stokes' Theorem* enables us to rewrite the geometrical phase as a surface integral,

$$\oint_\zeta \mathrm{d}x^k \, a_k(x) = \frac{1}{2} \int_{\mathcal{S}} \mathrm{d}S^{ij} \, f_{ij}(x). \tag{B.12}$$

Above, ζ is the closed contour determined by $x(t)$, $\mathcal{S}$ is a surface with ζ as boundary, $\mathrm{d}S^{ij}$ is the element of an infinitesimal surface element, and $f_{ij}(x)$ is the tensor field discussed in Appendix A.2.

□

Appendix C

Bessel Functions

Bessel functions appear on several occasions in this thesis. A selection of their properties relevant for our purposes are listed in this section. We also present a schematic proof on the absolute normalizability of the nth order Bessel function. The material in this section is based on [36].

C.1 Bessel Functions of the First and Second Kind

Bessel's differential equation of order α reads

$$x^2\frac{\mathrm{d}^2y}{\mathrm{d}x^2} + x\frac{\mathrm{d}y}{\mathrm{d}x} + (x^2 - \alpha^2)y = 0. \tag{C.1}$$

Two often used solutions to this equations are referred to as solutions of the first kind, J_α, and solutions of the second kind, Y_α. The functions J_α (Y_α) are characterized by being finite (singular) at the origin. Frobenius' method of generalized power series may be applied to find polynomial expansions of these functions. In other words, making the ansatz $y(x) = \sum_{n=0}^{\infty} a_n x^{n+s}$ yields a recursion relation in the coefficients a_n. The functions $J_\alpha(x)$ correspond to solutions with $s = \alpha$ and $a_0 = 1/(2^\alpha\Gamma(1+\alpha))$. This procedure results in the power series

$$J_\alpha(x) = \sum_{m=0}^{\infty} \frac{(-1)^m}{\Gamma(m+1)\Gamma(m+1+\alpha)} \left(\frac{x}{2}\right)^{2m+\alpha}. \tag{C.2}$$

Consider the integer ordered Bessel function $J_n(x)$ with $n \in \mathbb{N}$. The small argument expansion follows from (C.2),

$$J_n(x) = \frac{1}{\Gamma(n+1)} \left(\frac{x}{2}\right)^n + \mathcal{O}(x^{n+2}). \tag{C.3}$$

The functions also have a simple asymptotic behaviour,

$$J_n(x) \sim \sqrt{\frac{2}{\pi x}} \cos\left(x - \frac{2n+1}{4}\pi\right) + \mathcal{O}(x^{-3/2}). \tag{C.4}$$

Furthermore, the integer ordered Bessel functions satisfy the dependency relation $J_{-n}(x) = (-1)^n J_n(x)$. One may replace $s = -\alpha$ in Frobenius' method and obtain a second class of solutions, $J_{-\alpha}(x)$, which are linearly independent from J_α as long as $\alpha \notin \mathbb{N}$. The following combination of solutions are usually called Neumann or Weber functions and defines the solutions of the second kind:

$$Y_\alpha(x) = \frac{\cos(\pi\alpha)J_\alpha(x) - J_{-\alpha}(x)}{\sin(\pi\alpha)}. \tag{C.5}$$

The integer ordered Bessel functions of the second kind, $Y_n(x)$, are obtained for any $n \in \mathbb{N}$ by taking the limit $Y_n(x) = \lim_{\alpha\to n} Y_\alpha(x)$. They diverge (logarithmically for $n = 0$) as $x \to 0$ and have asymptotic forms similar to $J_n(x)$,

$$Y_n(x) \sim \sqrt{\frac{2}{\pi x}} \sin\left(x - \frac{2n+1}{4}\pi\right) + \mathcal{O}(x^{-3/2}). \tag{C.6}$$

A question that naturally arises in section 5.3.3 about Majorana modes concerns the integrability of $J_n(x)$. Below, we provide a schematic proof, based on basic techniques from calculus, that answers this question.

THEOREM 2. $\int_0^\infty \mathrm{d}x\, |J_n(x)|^p < \infty$ *if and only if* $p > 2$.

PROOF. We only need to consider the tail behaviour of the integral, let us say from some value $M \in \mathbb{R}$ to ∞. This means we can apply the asymptotic form of the function. Using equation (C.4) observe that

$$|J_n(x)|^p \sim (2/\pi)^p x^{-p/2} |\cos(x - (2n+1)\pi/4)|^p \Big(1 + \mathcal{O}(x^{-1})\Big). \tag{C.7}$$

Assume first that $p > 2$. Then, the integral of the tail function $|J_n(x)|^p$ is clearly finite since,

$$\int_M^\infty \mathrm{d}x\, x^{-p/2} |\cos(x - (2n+1)\pi/4)|^p \leq \int_M^\infty \mathrm{d}x\, x^{-p/2} < \infty \quad \forall\, p > 2. \tag{C.8}$$

Next order terms, which are bounded by $x^{-p/2-1}$, are of course also convergent.

Assume now that $p \leq 2$. We again consider only the first term in (C.7) since next order terms are trivially bounded. The 2π-periodicity of the cosine is exploited by splitting the integral in the partitions $A_m = [M + 2\pi(m-1), M + 2\pi m)$. We see that the intervals A_m are disjoint, and that their union covers the integration domain, $\cup_{m=1}^\infty A_m = [M, \infty)$. Therefore,

$$\begin{aligned} I &\equiv \int_M^\infty \mathrm{d}x\, x^{-p/2} |\cos(x-(2n+1)\pi/4)|^p \\ &= \sum_{m=1}^\infty \int_{A_m} \mathrm{d}x\, x^{-p/2} |\cos(x-(2n+1)\pi/4)|^p \\ &\equiv \sum_{m=1}^\infty b_m(p). \end{aligned} \tag{C.9}$$

Moreover, since $x^{-p/2}$ is strictly decreasing in x for positive p, we have that $(M + 2\pi m)^{-p/2} < x^{-p/2}$ for $x \in A_m$, and thereby the inequality

$$\frac{1}{(M+2\pi m)^{p/2}} \int_{A_m} \mathrm{d}x\, |\cos(x-(2n+1)\pi/4)|^p < \int_{A_m} \mathrm{d}x\, \frac{|\cos(x-(2n+1)\pi/4)|^p}{x^{p/2}}. \tag{C.10}$$

The term $N_p \equiv \int_{A_m} \mathrm{d}x\, |\cos(x-(2n+1)\pi/4)|^p$ is independent of m since the integrand is periodic in 2π. Consider equation (C.9) again, with the use of the inequality in (C.10),

$$\infty = N_p \sum_{m=1}^\infty \frac{1}{(M+2\pi m)^{p/2}} < \sum_{m=1}^\infty b_m(p) = I. \tag{C.11}$$

The sum on the left side is a (shifted) divergent series for $p \leq 2$ (harmonic series for $p = 2$), and the comparison test for convergence of series tells us that I diverges as well. This completes the proof. □

C.2 Modified Bessel Functions of the First and Second Kind

Bessel's *modified* differential equation of order α,

$$x^2 \frac{\mathrm{d}^2 y}{\mathrm{d}x^2} + x \frac{\mathrm{d}y}{\mathrm{d}x} - (x^2 + \alpha^2) y = 0, \tag{C.12}$$

is obtained by making the replacement $x \mapsto ix$ in (C.1). Not surprisingly, its solutions of the first and second kind, denoted by I_α and K_α respectively, are related to J_α and Y_α by

$$\begin{aligned} I_\alpha(x) &= i^{-\alpha} J_\alpha(ix), \\ K_\alpha(x) &= \frac{\pi}{2} i^{\alpha+1} \Big(J_\alpha(ix) + i Y_\alpha(ix) \Big). \end{aligned} \tag{C.13}$$

The hyperbolic Bessel functions, $I_\alpha(x)$ and $K_\alpha(x)$, are adjusted to become real for real x. In the small x expansion, I_α behaves similarly to J_α, and K_α similarly to Y_α. Their asymptotic forms are given by

$$\begin{aligned} I_n(x) &\sim \frac{1}{\sqrt{2\pi x}} e^x \Big(1 + \mathcal{O}(x^{-1})\Big), \\ K_n(x) &\sim \sqrt{\frac{\pi}{2x}} e^{-x} \Big(1 + \mathcal{O}(x^{-1})\Big). \end{aligned} \tag{C.14}$$

Appendix D

Code Attachment

A selection of the code written during this work is listed. The code samples represent a small fraction of the total amount of code produced. Still, it is meant to illustrate the diversity of the applied methods and the most essential structures needed to reproduce the numerical results.

D.1 Diagonalization of the Kitaev Chain

In Listing D.1 a `C++` script that diagonalizes the Kitaev chain is provided. This code is the main ingredient used to produce the results in section 4.4, in particular Figure 4.5. Compilation and plotting of the results was done with `Python`. Note that this script must be compiled with the package `Armadillo` installed. This package is described in [27]. In section 6.3 the $p + ip$ model was discretized, and the BdG equations were formulated as an eigenvalue problem. Thus, the matrix that is set up in Listing D.1 can be modified to describe $\mathcal{A}$ from equation (6.59) instead. Thereby, this code structure may be reused.

```
1  // A C++ script that diagonalizes the Kitaev chain.
2  // Eigenvalues are written to a text file.
3
4  #include <armadillo>
5  #include <iomanip>
6  using namespace std;
7  using namespace arma;
8
9  // Gap function with kink declared here:
10 double Delta_kink(int x, int N, double Delta_0) {
11     double s = 10.0;
12     return -Delta_0*tanh((x - (N-2)/2.0 )/s); }
13
14 int main(int argc, char** argv) {
15   int n, A; // 2n: matrix dimension, A: number of chemical
         potentials.
16   double t, Delta0, h; // t: hopping parameter, Delta0:
         asymptotic order parameter, h: step length.
```

```
17    char *outfilename;
18
19    if( argc <= 5 ){
20        cout << "Bad Usage: " << argv[0] <<
21            " Read also n, outfilename, A, t and Delta0 on same
                  line" << endl;
22        exit(1);
23    }
24    else {
25        n = atoi(argv[1]);
26        outfilename = argv[2];
27        A = atoi(argv[3]);
28        t = atof(argv[4]);
29        Delta0 = atof(argv[5]);
30    }
31
32    int N = 2*n; // matrix dimension
33    vec mu(A+1); // Armadillo vector of chemical potentials
34    h = 4.0*t/A; // discretization in chemical potential
35    for (int j=0; j < A+1; j++) { mu(j) = -2.0*t + j*h; }
36
37    ofstream ofile;
38    ofile.open(outfilename);
39
40    // Outer loop over all chemical potentials:
41    for (int l = 0; l < A+1; l++) {
42      // Set up matrix and diagonalize it for each value of mu:
43      int x_int; // dummy variable (position)
44      double mu_val = mu(l); // current value of mu
45      mat M(N,N);
46      M.zeros();
47      // Set up matrix in a brute force way:
48      for (int i=0; i < N; i++) {
49        if (i % 2 == 0) {
50          x_int = i/2;
51          M(i,i) = -mu_val/2.0;
52          if (i < N-3) {
53            M(i,i+3) = +Delta_kink(x_int, n, Delta0)/4.0;
54            M(i+3,i) = +Delta_kink(x_int, n, Delta0)/4.0;
55            M(i+3,i+1) = +t/4.0;
56            M(i+1,i+3) = +t/4.0;
57          }
58          if (i < N-2) { M(i,i+2) = -t/4.0; }
59          if (i > 1) { M(i,i-2) = -t/4.0; }
60        }
61        else {
62          x_int = (i-1)/2;
63          M(i,i) = +mu_val/2.0;
64          if (i < N-1) { M(i,i+1) = -Delta_kink(x_int, n,
                Delta0)/4.0; }
65          if (i < N-1) { M(i+1,i) = -Delta_kink(x_int, n,
                Delta0)/4.0; }
66        }
67      }
68      vec eigval; // vector with eigenvalues
69      mat eigvec; // matrix with eigenvectors
70      eig_sym(eigval, eigvec, M); // fetch eigenvalues
```

```
71      // Writing results to outfile:
72      ofile << " Eigenvalues for n = " << n;
73      ofile << " for mu = " << mu_val << endl;
74      for (int i=0; i < N; i++) { ofile << setw(11) <<
            setprecision(8) << eigval(i) << endl; }
75    } // calculation for mu_val done. Update mu and continue
76    ofile.close();
77    return 0;
78  } // end of main program
```

Listing D.1: A C++ script that diagonalizes the open Kitaev chain with a spatially varying order parameter Δ_x. The returned eigenvalues are written to a text file that may be read and plotted with a Python script. The parameters of the problem are provided by the user as command line arguments when running this script.

D.2 The Radial Majorana Zero Mode Equation

In Listing D.2 we have included the Python script that produces the results plotted in Figure 5.3(a). This code sample applies the module ODESolver as described in [33], and it contains tabulated vortex data from [32] that are interpolated with a cubic spline method from scipy. Note that equation (5.40) is formulated as a coupled set of two first order differential equations in this implementation.

```
1  # A python script that interpolates reference date
2  # for a vortex of vorticity l = -1.
3  # The interpolation is applied in solving the differential
       equation
4  # describing a Majorana zero mode bound to the vortex.
5
6  from scipy.interpolate import interp1d
7  # The module ODESolver has Runge Kutta 4th order method built in:
8  from ODESolver import ODESolver, RungeKutta4
9  from math import sqrt, pi
10 import numpy as np
11
12 # Initial conditions and parameters are fixed in this block:
13 rho_min = 0.01
14 rho_max = 14.99
15 u_init = [1.0, 0.0] # initial conditions, [u(0), du/drho(0)]
16 n = 800 # grid resolution
17 D0 = 1.0 # asymptotic value of the order parameter
18 eta = 1.0 # chemical potential
19
20 # Function to find the value of R from which the solution stays
21 # less than a fraction p of its maximum value:
22 def less_than_p(R, func_vals, p):
23     m = len(R)
24     tol = max(abs(func_vals))*p
25     R_tol = 0.0
26     for i in xrange(m):
```

```
27            if abs(func_vals[i]) > tol:
28                R_tol = R[i]
29        return R_tol
30
31    # Trapezoidal integrator used for normalization:
32    def Trapezoidal_integrator(R, func_vals):
33        h = R[1]-R[0]
34        m = len(R)
35        S = 0.0
36        for l in range(1,m-1):
37            S += func_vals[l]*h
38        S += (func_vals[0]+func_vals[m-1])*h/2.0
39        return S
40
41    # A class structure that contains an interpolator
42    # of tabulated vortex values and callable functions
43    # that return the right hand sides of the differential equation
44    # expressed as two coupled first order equations.
45    # The instances of this class should be passed to ODESolver.
46    class Vortex_numerical_l1:
47
48        def __init__(self, Delta0, mu, activate_g=1):
49            self.D = float(Delta0)
50            self.mu = float(mu)
51            self.bool = activate_g # boolan variable. If 0 the order
                  parameter is set to 0.
52            # Tabulated reference data for a vortex with l = -1:
53            self.rho_num =
                  np.array([0.0,0.1,0.2,0.3,0.4,0.5,0.6,0.7,0.8,0.9,1.0,
54                        1.5,2.0,2.5,3.0,3.5,4.0,4.5,5.0,6.0,7.0,8.0,
55                        9.0,10.0,11.0,12.0,13.0,14.0,15.0])
56            self.g_l1_num =
                  self.D*np.array([0.0,0.058250,0.116064,0.173022,
57                        0.228729,0.282827,0.335001,0.384990,0.432586,
58                        0.477636,0.520039,0.692060,0.804926,0.874944,
59                        0.917461,0.943364,0.959460,0.969771,0.976620,
60                        0.984730,0.989150,0.991845,0.993627,0.994874,
61                        0.995784,0.996470,0.997000,0.997418,0.997755])
62            # Callable function of cubic spline interpolated values:
63            self.f = interp1d(self.rho_num, self.g_l1_num,
                  kind='cubic')
64
65        # Help function that returns the order parameter:
66        def f_val(self, rho):
67            if self.bool:
68                value = self.f(rho)
69            else: value = 0.0
70            return value
71
72        # This function returns the term g*g'
73        # with a numerical differentiation of g = \sqrt{f}.
74        # A symmetric formula for differentiation is used.
75        def g_dg_numerical(self, rho, h=1E-6):
76            if self.bool:
77                term = sqrt(self.f_val(rho+h))-sqrt(self.f_val(rho-h))
78                d_sqrt_g = term/(2*h)
79                value = d_sqrt_g*sqrt(self.f_val(rho))
```

```
80          else: value = 0.0
81          return value
82
83      def __call__(self, u, rho):
84      # u is a two-component vector.
85      # u[0] is the same as u(rho)
86      # u[1] is the same as du(rho)/drho
87      # This function returns the derivatives of u[0] and u[1]
88        v, w = u
89          term1 = -self.f_val(rho)-1.0/rho
90          term2 = -self.g_dg_numerical(rho)
91          term2 -= self.mu
92          term2 -= self.f_val(rho)/(2.0*rho)
93          return [w, term1*w + term2*v]
94
95  rho = np.linspace(rho_min, rho_max, n, endpoint=True)
96  V = Vortex_numerical_l1(Delta0=D0, mu=eta) # instance with vortex
97  V0 = Vortex_numerical_l1(Delta0=D0, mu=eta, activate_g=0) #
        instance without vortex
98
99  # Passing instance V to RK4 solver:
100 method = RungeKutta4(V)
101 method.set_initial_condition(u_init)
102 u, rho = method.solve(rho)
103 u0_values = u[:,0] # extracting the solution (not normalized yet)
104
105 # Normalizing solution:
106 u0_square = rho*u0_values**2 # integrand
107 I = Trapezoidal_integrator(rho, u0_square)
108 N = 1.0/sqrt(2*pi*I) # normalization constant
109 u0_values *= N # normalized solution is now ready for plotting
110
111 R_c = less_than_p(rho, u0_values, 0.01)
112 print " Critical radius at which the solution is less than 1%
        of maximum: ", R_c
113 print " Value of the vortex profile at critical radius: ",
        V.f_val(R_c)
114
115 # Similar calculation without vortex as a reference calculation:
116 method0 = RungeKutta4(V0)
117 method0.set_initial_condition(u_init)
118 v0, rho0 = method0.solve(rho)
119 v0_values = v0[:,0]*N # extracting the solution and scaling it
        with the normalization of u0
```

Listing D.2: A `Python` script that applies cubic spline interpolated values of reference data for the order parameter profile from [32]. The values are used when solving the radial Majorana zero mode equation (5.40), which is done with the Runge-Kutta 4th order method. The `Python` module named `ODESolver`, which is importet and used in this script, was taken from [33] and can be found documented and explained in that reference. This module was used due to its object oriented and compact implementation.

References

[1] J. M. Leinaas and J. Myrheim, "On the Theory of Identical Particles," *Il Nuovo Cimento B*, vol. **37**, pp. 1 – 23, 1977. DOI: 10.1007/bf02727953.

[2] J. Bardeen, L. N. Cooper, and J. R. Schrieffer, "Microscopic Theory of Superconductivity," *Physical Review*, vol. **106**, pp. 162 – 164, 1957. DOI: 10.1103/PhysRev.106.162.

[3] M. Tinkham, *Introduction to Superconductivity*. McGraw-Hill, Inc., 1996.

[4] A. P. Schnyder, S. Ryu, A. Furusaki, and A. W. W. Ludwig, "Classification of topological insulators and superconductors in three spatial dimensions," *Physical Review B*, vol. **78**, p. 195125, 2008. DOI: 10.1103/PhysRevB.78.195125.

[5] M. Leijnse and K. Flensberg, "Introduction to topological superconductivity and Majorana fermions," *Semiconductor Science and Technology*, vol. **27**, p. 124003, 2012. DOI: 10.1088/0268-1242/27/12/124003.

[6] D. A. Ivanov, "Statistics of Half-Quantum Vortices in p-Wave Superconductors," *Physical Review Letters*, vol. **86**, pp. 268 – 271, 2001. DOI: 10.1103/PhysRevLett.86.268.

[7] J. Alicea, Y. Oreg, G. Refael, F. von Oppen, and M. P. A. Fisher, "Non-Abelian statistics and topological quantum information processing in 1D wire networks," *Nature Physics*, vol. **7**, pp. 412 – 417, 2011. DOI: 10.1038/nphys1915.

[8] V. Mourik, K. Zuo, S. M. Frolov, S. R. Plissard, E. P. A. M. Bakkers, and L. P. Kouwenhoven, "Signatures of Majorana Fermions in Hybrid Superconductor-Semiconductor Nanowire Devices," *Science*, vol. **336**, pp. 1003 – 1007, 2012. DOI: 10.1126/science.1222360.

[9] S. Nadj-Perge, I. K. Drozdov, J. Li, H. Chen, S. Jeon, J. Seo, A. H. MacDonald, B. A. Bernevig, and A. Yazdani, "Observation of Majorana fermions in ferromagnetic atomic chains on a superconductor," *Science*, vol. **346**, pp. 602 – 607, 2014. DOI: 10.1126/science.1259327.

[10] A. Y. Kitaev, "Unpaired Majorana fermions in quantum wires," *Physics-Uspekhi*, vol. **44**, p. 131, 2001. DOI: 10.1070/1063-7869/44/10S/S29.

[11] J. Alicea, "New directions in the pursuit of Majorana fermions in solid state systems," *Reports on Progress in Physics*, vol. **75**, p. 076501, 2012. DOI: 10.1088/0034-4885/75/7/076501.

[12] C. Nayak, S. H. Simon, A. Stern, M. Freedman, and S. D. Sarma, "Non-Abelian anyons and topological quantum computation," *Reviews of Modern Physics*, vol. **80**, pp. 1083 – 1159, 2008. DOI: 10.1103/RevModPhys.80.1083.

[13] V. Gurarie and L. Radzihovsky, "Zero modes of two-dimensional chiral p-wave superconductors," *Physical Review B*, vol. **75**, p. 212509, 2007. DOI: 10.1103/PhysRevB.75.212509.

[14] A. A. Abrikosov, "Nobel Lecture: Type-II superconductors and the vortex lattice," *Reviews of Modern Physics*, vol. **76**, pp. 975 – 979, 2004. DOI: 10.1103/RevModPhys.76.975.

[15] S. Fujita and S. Godoy, *Quantum Statistical Theory of Superconductivity*. Kluwer Academic Puplishers, 2002.

[16] F. Ravndal and E. G. Flekkøy, "Statistical Physics – a second course," Department of Physics, University of Oslo, 2014.

[17] D. J. Griffiths, *Introduction to Quantum Mechanics*. Pearson Education, Inc., 2005.

[18] L. P. Gor'kov, "Microscopic Derivation of the Ginzburg-Landau Equations in the Theory of Superconductivity," *Journal of Experimental and Theoretical Physics*, vol. **36**, pp. 1918 – 1923, 1959. URL: http://www.jetp.ac.ru/cgi-bin/e/index/r/36/6/p1918?a=list.

[19] E. Majorana and L. Maiani, *Ettore Majorana Scientific Papers: On occasion of the centenary of his birth*, pp. 201 – 233. Springer Berlin Heidelberg, 2006. DOI: 10.1007/978-3-540-48095-2_10.

[20] F. Wilczek, "Majorana returns," *Nature Physics*, vol. **5**, pp. 614 – 618, 2009. DOI: 10.1038/nphys1380.

[21] F. Wilczek, *Fractional Statistics and Anyon Superconductivity*. World Scientific Publishing Co. Pte. Ltd., 1990.

[22] C. C. Adams, *The Knot Book: An Elementary Introduction to the Mathematical Theory of Knots*. American Mathematical Society, 2004.

[23] J. M. Leinaas, "Non-Relativistic Quantum Mechanics. Lecutre notes – FYS4110," Department of Physics, University of Oslo, 2014.

[24] N. Read and D. Green, "Paired states of fermions in two dimensions with breaking of parity and time-reversal symmetries and the fractional quantum Hall effect," *Physical Review B*, vol. **61**, pp. 10267 – 10297, 2000. DOI: 10.1103/PhysRevB.61.10267.

[25] M. V. Berry, "Quantal Phase Factors Accompanying Adiabatic Changes," *Proceedings of the Royal Society of London A: Mathematical, Physical and Engineering Sciences*, vol. **392**, pp. 45 – 57, 1984. DOI: 10.1098/rspa.1984.0023.

[26] D. Xiao, M. Chang, and Q. Niu, "Berry phase effects on electronic properties," *Reviews of Modern Physics*, vol. **82**, pp. 1959 – 2007, 2010. DOI: 10.1103/RevModPhys.82.1959.

[27] M. Hjorth-Jensen, "Computational Physics. Lecture Notes Fall 2015," Department of Physics, University of Oslo, 2015.

[28] C. Spånslätt, E. Ardonne, J. C. Budich, and T. H. Hansson, "Topological aspects of π phase winding junctions in superconducting wires," *Journal of Physics: Condensed Matter*, vol. **27**, p. 405701, 2015. DOI: 10.1088/0953-8984/27/40/405701.

[29] J. Zhou, S. Wang, Y. Wu, R. Li, and S. Kou, "Topological mid-gap states of $p_x + ip_y$ topological superconductor with vortex square superlattice," *Physics Letters A*, vol. **378**, pp. 2576 – 2581, 2014. DOI: 10.1016/j.physleta.2014.07.008.

[30] N. Hayashi, T. Isoshima, M. Ichioka, and K. Machida, "Low-Lying Quasiparticle Excitations around a Vortex Core in Quantum Limit," *Physical Review Letters*, vol. **80**, pp. 2921 – 2924, 1998. DOI: 10.1103/PhysRevLett.80.2921.

[31] A. L. Fetter, "Vortices in an Imperfect Bose Gas. I. The Condensate," *Physical Review*, vol. **138**, pp. A429 – A437, 1965. DOI: 10.1103/PhysRev.138.A429.

[32] M. P. Kawatra and R. K. Pathria, "Quantized Vortices in an Imperfect Bose Gas and the Breakdown of Superfluidity in Liquid Helium II," *Physical Review*, vol. **151**, pp. 132 – 137, 1966. DOI: 10.1103/PhysRev.151.132.

[33] H. P. Langtangen, *A Primer on Scientific Programming with Python*. Springer, 2011.

[34] M. Cheng, R. M. Lutchyn, V. Galitski, and S. D. Sarma, "Tunneling of anyonic Majorana excitations in topological superconductors," *Physical Review B*, vol. **82**, p. 094504, 2010. DOI: 10.1103/PhysRevB.82.094504.

[35] B. Rosenstein, I. Shapiro, and B. Y. Shapiro, "Majorana states in a p-wave superconducting ring," *Europhysics Letters*, vol. **102**, p. 57002, 2013. DOI: 10.1209/0295-5075/102/57002.

[36] M. L. Boas, *Mathematical Methods in the Physical Sciences*. John Wiley & Sons, Inc., 2006.